HELLENIC REPUBLIC
National and Kapodistrian University of Athens
— EST. 1837 —

MASTER THESIS

Resolution Study of a γ-Camera System for Single Photon Emission Computed Tomography (SPECT) at Preclinical Level

Despoina Zarketan

Supervisor: Efstathios Stiliaris, Associate Professor

Master of Science

Medical Physics-Radiophysics

Athens, June 2019

3Member Examination Committee

P. Karaiskos, Professor, School of Medicine
C. Loukas, Assistant Professor, School of Medicine
E. Stiliaris, Associate Professor, Physics Department

Examination Date: 25/06/2019

To my parents,

Tasos & Vaso

Abstract

The current thesis is an experimental study which focuses on the resolution determination of a small-field γ-Camera system dedicated to Single Photon Emission Computed Tomography (SPECT) at preclinical level. The Position Sensitive Photomultiplier Tube (PSPMT) was characterized in terms of its spatial and energy resolution. For this purpose, light pulses of controlled time-width were guided to the front surface of the PSPMT and the multi-anodic charge signal was detected and analyzed. The linearity of the accumulated charge as a function of the light pulse duration, which equivalently reflects the energy of an incident γ-ray photon, was verified. In parallel, the overall charge gain of the PSPMT system was measured for various values of the high voltage power supply.

Simple geometrical phantoms consisted of ^{99m}Tc filled capillaries were used to evaluate the performance and the spatial resolution of the whole γ-Camera system. Detected aberrations in planar imaging were eliminated by applying 1D and 2D linear interpolation functions based on supporting points with known nominal position. Corrected images on planar and tomographic level were produced for a more complicated geometrical phantom as well as for specific targeted organs of a small mouse injected with ^{99m}Tc radiopharmaceutical.

KEY WORDS: Position Sensitive PhotoMultiplier Tube (PSPMT), small-field γ-Camera, spatial resolution, energy response, gain factor, correction algorithm, Algebraic Reconstruction Technique (ART).

Σύνοψη

Η παρούσα διπλωματική εργασία αποτελεί μια πειραματική μελέτη που εστιάζει στον προσδιορισμό της διακριτικής ικανότητας ενός συστήματος μικρού πεδίου γ-Camera, το οποίο προορίζεται για Μονοφωτονική Τομοσπινθηρογραφία (SPECT) σε προκλινικό επίπεδο. Ο χωρικά ευαίσθητος Φωτοπολλαπλασιαστής (PSPMT) χαρακτηρίστηκε τόσο ως προς την χωρική όσο και ως προς την ενεργειακή διακριτική του ικανότητα. Για τον σκοπό αυτό, φωτεινοί παλμοί με ρυθμιζόμενο χρονικό εύρος καθοδηγούνταν στην εμπρόσθια επιφάνεια του PSPMT και το φορτίο της ανόδου ανιχνευόταν ως σήμα και αναλυόταν. Η γραμμικότητα του συλλεγόμενου φορτίου σαν συνάρτηση της διάρκειας του φωτεινού παλμού, η οποία ισοδύναμα προσομοιώνει την ενέργεια ενός προσπίπτοντος γ φωτονίου, επαληθεύτηκε. Παράλληλα, το συνολικό κέρδος φορτίου του συστήματος του PSPMT μετρήθηκε για ποικίλες τιμές της εφαρμοζόμενης υψηλής τάσης.

Απλά γεωμετρικά ομοιώματα αποτελούμενα από τριχοειδή και γεμισμένα με ^{99m}Tc, χρησιμοποιήθηκαν ώστε να αξιολογηθεί η απόδοση και η χωρική διακριτική ικανότητα ολόκληρου του συστήματος της γ-Camera. Οι παραμορφώσεις που ανιχνεύτηκαν κατά την προβολική απεικόνιση εξομαλύνθηκαν με την εφαρμογή 1D και 2D συναρτήσεις γραμμικής παρεμβολής που βασίστηκαν σε υποστηρικτικά σημεία γνωστών ονομαστικών θέσεων. Τέλος, παρήχθησαν διορθωμένες εικόνες σε προβολικό και τομογραφικό επίπεδο ενός πιο σύνθετου γεωμετρικού ομοιώματος, καθώς επίσης και συγκεκριμένων, ιχνηθετημένων οργάνων ενός μικρού ποντικιού στο οποίο είχε χορηγηθεί ραδιοφάρμακο τεχνητίου ^{99m}Tc.

Acknowledgements

List of Tables

Contents

Chapter I

Introduction to Nuclear Medicine Imaging

1.1 Introduction

One of the most important medical field nowadays is this of *Nuclear Medicine*. *Nuclear Medicine* is a medical specialty that uses radioactive tracers (radiopharmaceuticals) to assess bodily functions and to diagnose and treat disease. Specially designed cameras allow doctors to track the path of these radioactive tracers. So, these techniques are known as *Emission Techniques*. The most common imaging modalities are this of Positron Emission Tomography (PET) and Single Photon Emission Tomography (SPECT).

The roles of imaging in disease diagnosis and treatment monitoring continue to increase because of advances in imaging technologies and concomitant improvements in detection sensitivity, spatial resolution, and quantitative information. In a perfect world, a single imaging method could furnish anatomic, physiologic, and molecular information with high sensitivity and specificity. However, none of the current imaging methods used in humans provides comprehensive medical imaging. Whereas Computed Tomography (CT) and Magnetic Resonance Imaging (MRI) provide high anatomic resolution, the exceptionally high detection sensitivity of optical and radionuclear methods, such as PET and SPECT, enables these techniques to excel at molecular imaging **[CUL08]**.

What is more, nuclear medicine imaging offers a number of important advantages in the context of clinical practice, as well as in clinical and preclinical research. First, the specific activity (i.e., activity per unit mass) of radiopharmaceuticals and the detection sensitivity of radionuclide imaging instruments are generally high. Second, like other clinical imaging modalities, nuclear medicine imaging is noninvasive and thus may be used serially to characterize the longitudinal time course of some process (e.g., response to a therapeutic intervention). Third, nuclear medicine images are quantitative, or at least semi-quantitative, meaning that image intensity (i.e., counts) reflects the radiopharmaceutical-derived activity concentration. Fourth, a large number and variety of molecularly targeted and/or pathway-targeted radiopharmaceuticals (such as metabolites and metabolite analogs, drugs, receptor-binding ligands, antibodies, and other immune constructs, etc.) have been, and continue to be, developed for increasingly specific characterization of in situ biology.

Nuclear medicine imaging is not without its drawbacks, however. These include coarse spatial resolution expressed as the full-width half-maximum of the system point or line spread function; this ranges from ~5 mm for PET to ~8 mm or less for SPECT at clinical level. This is about an order of magnitude poorer than that of CT and MRI, that's why further studies at preclinical level are necessary (*Figure 1.1*). Further, nuclear medicine is a radiation-based imaging modality and thus delivers low, but non-negligible, radiation doses to patients, with effective doses and maximal organ-absorbed doses per study, typically of the order of ten millisieverts (mSv) and up to several centigrays (cGy), respectively. Moreover, nuclear medicine images generally include only limited anatomic information, which may complicate their analysis and interpretation. With the increasingly widespread availability of multi-modality (i.e., PET-CT and SPECT-CT)

devices, nuclear medicine images reflecting *in vivo* function may be registered and fused with anatomic images, largely overcoming this limitation **[ZAN12]**.
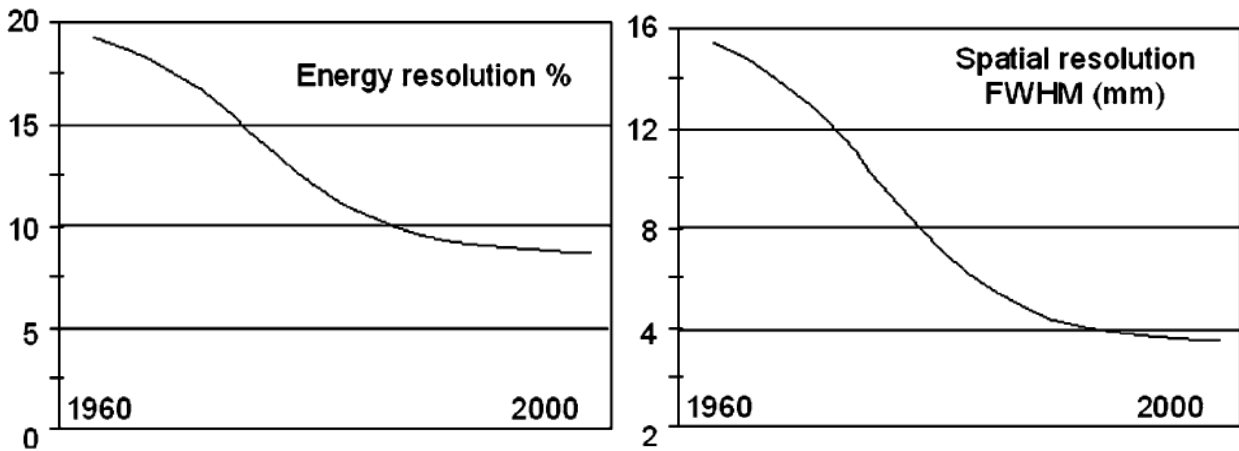
Figure 1.1. *The Energy and Spatial Resolution of SPECT modality at clinical level during the period 1960-2000.*

1.2 Single Photon Emission Computed Tomography (SPECT)

The Single Photon Emission Tomography (SPECT) is one of the most common nuclear medicine tomographic imaging technique using gamma rays. SPECT modality is consisted of one or more γ-Cameras which have the possibility of automatic or programmable rotation around the examined object or the patient to a desired radius and speed (*Figure 1.2*) **[GEO08]**. It is very similar to conventional nuclear medicine planar imaging using a γ-Camera (that is, scintigraphy) but is able to provide true 3D information. This information is typically presented as cross-sectional slices through the patient, but can be freely reformatted or manipulated as required.
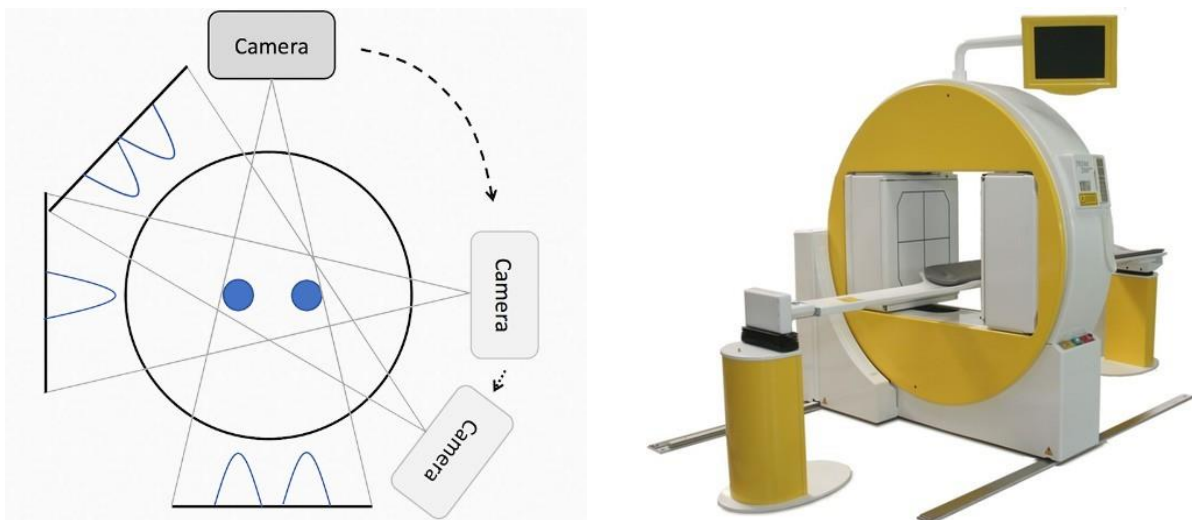
Figure 1.2. *A schematic illustration of the γ-Camera rotation taking planar images around the examined objects (left) and a clinical γ-Camera SPECT device (right).*

1.2.1 γ-Camera

 The gamma camera, shown in *Figure 1.3*, is the instrumental basis for both planar Scintigraphy and SPECT. The patient lies on a bed beneath the γ-camera, which is positioned close to the organ of interest. The gamma camera must be capable of γ-ray detection rates of up to tens of thousands per second, should reject those γ-rays that have been scattered in the body and therefore have no useful spatial information, and must have as high a sensitivity as possible in order to produce the highest quality images within a clinically acceptable imaging time. The roles of each of the separate components of the gamma camera are covered in the following sections.
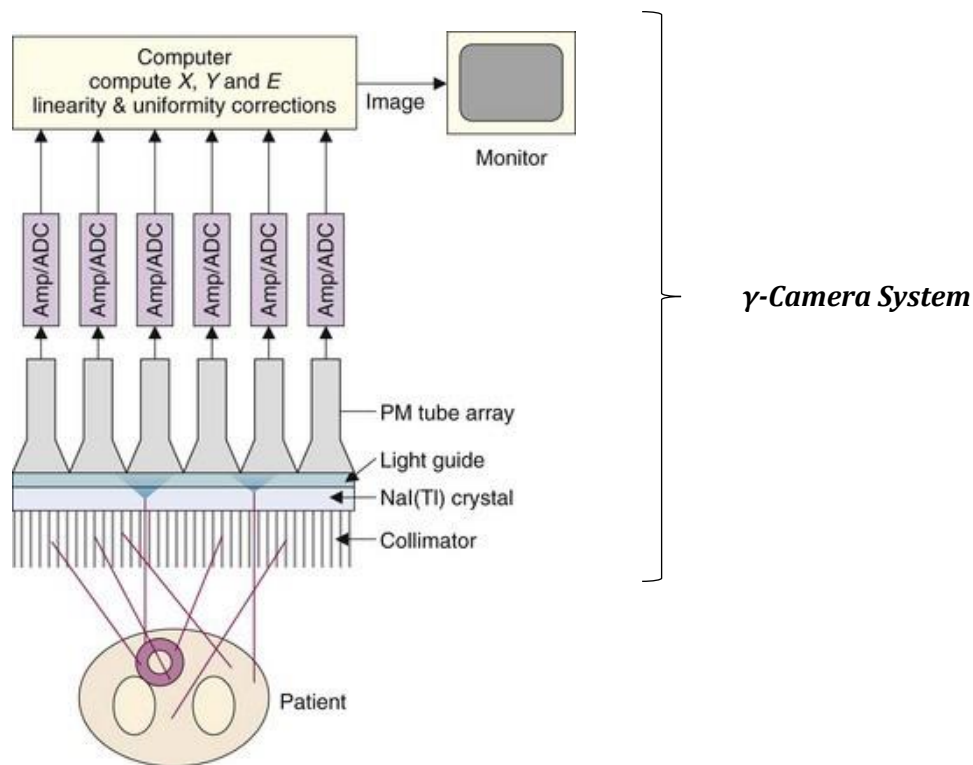
Figure 1.3. *A schematic illustration of all the components comprising a γ-Camera system.*

1.2.1.1 The Collimator

 The role of the collimator in nuclear medicine is very similar to that of the antiscatter grid in X-ray imaging. Since γ-rays from a source of radioactivity within the body are emitted in all directions, a much higher degree of collimation is required in nuclear medicine than in X-ray imaging. This, together with the high attenuation of γ-rays within the body, leads to a very high proportion of emitted γ-rays (99.9%) not being detected. There are six basic collimator designs: parallel hole, slanthole, converging, diverging, fan-beam and pinhole. Each has particular properties in terms of effects on image signal to noise ratio (SNR), contrast to noise ratio (CNR) and spatial resolution **[SMI11]**. The parallel hole collimator is the most common design, and so is described first.

3

i. Parallel hole collimator. As the name suggests, all the holes in the collimator are parallel to each other. The collimator is usually constructed from thin strips of lead in a hexagonally-based 'honeycomb' geometry, although round holes in a hexagonal array can also be used. Ideally there would be zero transmission of γ-rays through the septa themselves, but since this is not possible the septa are designed so that 95% of γ-rays are attenuated.

ii. Slanthole collimators consist of parallel septa which are all tilted at the same angle with respect to the detection crystal. They are used primarily for breast and cardiac imaging.

iii. Converging collimators have the holes focused towards the body, with the center of curvature ideally located at the middle of the imaging field-of-view (FOV). A converging collimator is used to magnify the image and increase the spatial resolution.

iv. A diverging collimator is essentially a converging collimator that has been turned around. This enables a larger FOV, compared to a parallel hole collimator, to be imaged. One application is planar scintigraphy of the whole body.

v. Fan-beam collimators are used primarily for brain and heart studies. The two dimensions of the collimator have different geometries: in the head/foot direction the holes are parallel, whereas in the radial direction they are similar to a converging collimator. Thus, these types of collimator provide image magnification over a reduced FOV.

vi. Pinhole collimators are used for imaging very small organs such as the thyroid and parathyroid. These collimators have a single hole with interchangeable inserts that come with a 3, 4 or 6 mm aperture. A pinhole collimator produces an image with significant magnification and higher spatial resolution, but also produces geometric distortion, particularly at the edges of the image.
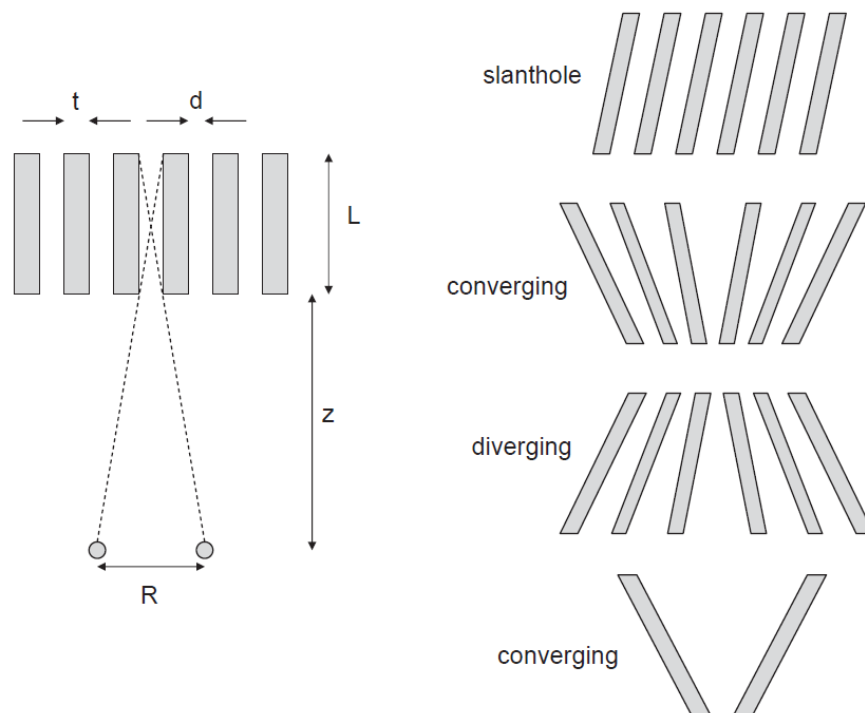
Figure 1.4. *(left) A parallel hole collimator, with parameters necessary (L,d,t,z) to calculate the spatial resolution, R. The patient would be positioned at the bottom of the figure, with the gamma camera at the top. (right) Four common types of collimator: from top-to-bottom, slanting hole, converging, diverging and pinhole.*

1.2.1.2 The Scintillation Crystal

Materials that emit visible light when they absorb energetic charged particles, g-rays, or x-rays are called scintillators, *Table 1.1* lists the physical properties of the materials that will be discussed in this section. Scintillators have several advantages as γ-ray detectors, including high intrinsic efficiency and moderate cost. They can also be fabricated into a large variety of shapes and sizes. However, scintillators require an additional stage to convert the scintillation light into an electronic pulse. Light is lost at the interface between the detector and the photon transducer, which limits energy resolution. The materials shown in *Table 1.1* have comparable effective atomic numbers and densities, which mean they will have similar photopeak efficiencies. The persistence of the scintillation limits the counting rate capability of the detectors, although counting rate losses are rarely a problem with SPECT when conventional collimation is used. The wavelength of the scintillation determines what kind of photon transducer can be used to turn the scintillation into an electronic pulse. The brightness of the scintillation expressed in terms of the output relative to NaI(Tl) directly affects the potential energy resolution **[MAD07]**.

Scintillator	Atomic number Z effective	Density ρ (g/cm^3)	Decay time τ (ns)	Wavelength λ (nm)	Relative light output (% of NaI(Tl))
NaI(Tl)	50	3.67	200	415	100
CsI(Tl)	54	4.5	1,000	550	45 (118*)
CsI(Na)	54	4.51	630	420	85
LaBr$_3$:Ce	47	5.3	25	360	160

*Represents total light output. Because of the long wavelength of the scintillation, the effective signal for CsI(Tl) is only 45% of NaI(Tl).

Table 1.1. *Scintillators used in SPECT modality and some of their properties.*

Along with the trend for making smaller and more compact imaging systems, new γ-camera designs have featured pixelated detectors, where the field of view is covered by an array of individual scintillators with a face size of typically 2–3mm instead of one large crystal, as with a conventional Anger scintillation camera. Each approach has its own advantages. The large detector geometry of a conventional scintillation camera is less costly to assemble and provides continuous sampling. Position information is determined by Anger logic or similar weighted averaging of photomultiplier tube (PMT) signals from an array of PMTs covering the detector back surface. One disadvantage to this approach is that the Anger logic breaks down near the detector edge, resulting in several centimeters of ''dead'' space. This is not much of a concern with large detectors but becomes substantial for smaller field-of-view systems. Pixelated detectors do not have dead edges and are preferred for small-field-of-view (FOV) configurations. The sampling and intrinsic spatial resolution of pixelated systems are determined by the face size of the individual detector elements. In addition to the increased assembly costs, energy resolution is usually worse for the pixelated detectors because of reduced light transmission and subsequent collection by the photon transducers.

Thallium-activated sodium iodide, NaI(Tl) is still the most commonly used scintillator for SPECT applications. In most clinical SPECT systems, the NaI(Tl) detector is one large crystal as described above. However, NaI(Tl) can be pixelated and several small-field-of-view devices, including small-animal SPECT systems, are configured that way. For clinical SPECT, the NaI(Tl) thickness is typically 6–10 mm. It is possible to have γ-camera detectors made with

NaI(Tl) crystals that are 25.4-mm thick (StarBrite; Saint-Gobain Crystals and Detectors) to obtain increased efficiency for
high-energy γ-emitters. Grooves are machined into the top surface of the detector to prevent light diffusion and to maintain acceptable intrinsic spatial resolution (4.1 mm at 140 keV).

Thallium-activated cesium iodide competes well with NaI(Tl) in terms of efficiency and it is not strongly hygroscopic. It has a significantly longer scintillation time, leading to a larger dead time, but that is rarely a concern for SPECT. However, the scintillation light from CsI(Tl) has alonger wavelength that is not as well matched to PMTs as sodium iodide. As a result, its performance with PMTs is worse than NaI(Tl) even though the total number of scintillation photons (including the infrared) is actually about 18% higher than NaI(Tl). However, these photons are detected with a high quantum efficiency with photodiodes that can replace PMTs. Sodium-activated cesium iodide, CsI(Na), is similar to CsI(Tl), but with an emission that is better matched to PMTs. It is currently being used as the detector in the LinoView small-animal SPECT system.

Lanthanum bromide, LaBr3, is a scintillation that has garnered attention as a potential detector for time-of-flight PET, but its properties are also attractive for single-photon imaging . LaBr3 has a very high light output with a correspondingly improved energy resolution (<6% at 140 keV) and an intrinsic efficiency comparable to NaI(Tl). In addition, LaBr$_3$ is a very fast detector and potentially very useful for approaches such as Compton γ-cameras, where high counting rates are likely to be encountered. It is also being used as the detector in a recently reported small-animal SPECT system.

1.2.1.3 The PhotoMultiplier Tubes (PMTs)

For every γ-ray that hits the scintillation crystal a few thousand photons are produced, each with a very low energy of a few electronvolts. These very low light signals need to be amplified and converted into an electrical current that can be digitized: PMTs are the devices used for this specific task. The basic design of a PMT is shown in *Figure 1.5*. The inside surface of the transparent entrance window of the PMT is coated with a material such as Cesium Antimony (CsSb) which forms a photocathode. Free electrons (photoelectrons) are generated via photoelectric interactions when the photons from the scintillation crystal strike this material. These electrons are accelerated towards the first stage of amplification, a metal plate termed a dynode held at a voltage of +300 volts with respect to the photocathode. This plate is also coated with a Bialkali material such as CsSb. When the electrons strike this dynode several secondary electrons are emitted for every incident electron: a typical amplification factor is between 3 and 6. A series of eight to ten further accelerating dynodes, each at a voltage of +100 volts with respect to the previous one, produces between 105 and 106 electrons for each initial photoelectron, creating an amplified current at the output of the PMT. A high voltage power supply is required for each PMT, in the range 1–2 kV. The PMTs are sealed in glass, and the entire enclosure evacuated to reduce attenuation of the electrons between the dynodes: a photograph of a single PMT is shown in *Figure 1.5*.
Since each PMT has a diameter of 2–3 cm, and the NaI(Tl) crystal is much larger in size, a number of PMTs are closely coupled to the scintillation crystal. The most efficient packing geometry is hexagonally-close-packed, which also has the property that the distance from the center of one PMT to that of each neighboring PMT is the same: this property is important for

determination of the spatial location of the scintillation event using an Anger position network. Arrays of 61, 75 or 91 PMTs are typically used, with a thin optical coupling layer used to
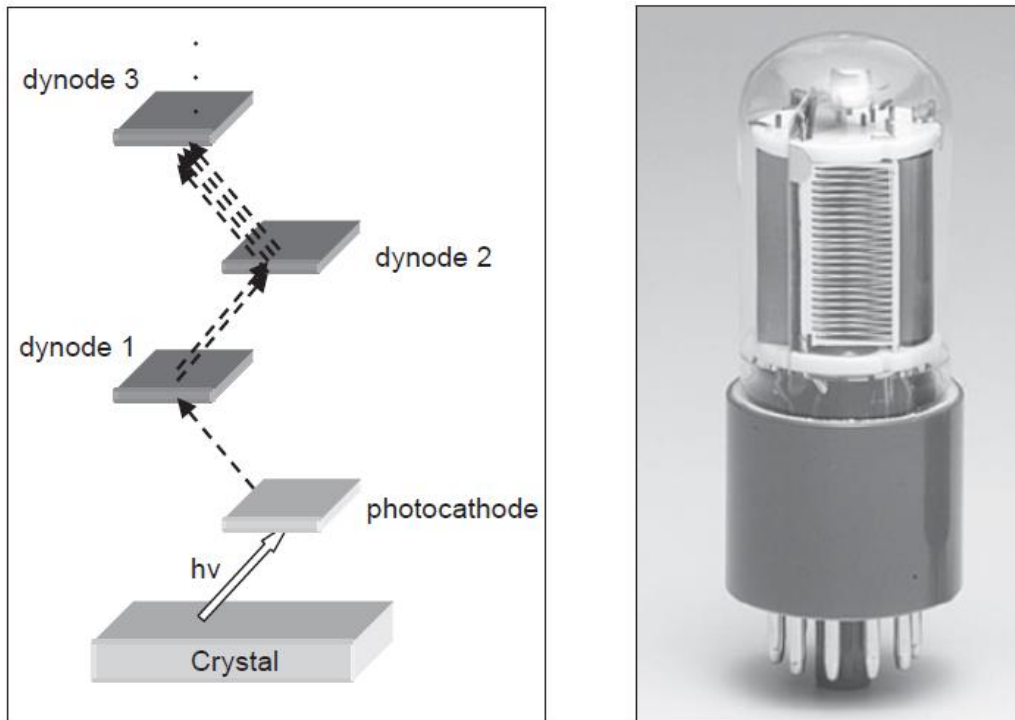
Figure 1.5. *Left a schematic illustration of the first three amplification stages in a PMT tube and right a commercial PMT. (Figure taken from 'Introduction to Medical Imaging. Physics, Engineering and Clinical Applications' N.B. Smith & A. Webb, Cambridge, 2011).*

interface the surface of each PMT with the scintillation crystal. Each PMT should ideally have an identical energy response, i.e. the output current for a given c-ray energy should be the same. If this is not the case, then artifacts are produced in the image. For planar nuclear medicine scans, a variation in uniformity of up to 10% can be tolerated; however, for SPECT imaging, covered later in this chapter, this value should be less than 1%. In practice, calibration of the PMTs is performed using samples of uniform and known radioactivity, and automatic data correction algorithms can then be applied to the data. More recently, continuous monitoring of individual PMTs during a nuclear medicine scan has become possible using a light-emitting diode (LED) calibration source for each PMT **[SMI11]**.

 The summed signal is sent to a pulse-height analyzer (PHA). The role of the PHA is to determine which of the recorded events correspond to c-rays that have not been scattered within tissue (primary radiation) and should be retained, and which have been Compton scattered in the patient,
do not contain any useful spatial information, and so should be rejected. Since the amplitude of the voltage pulse from the PMT is proportional to the energy of the detected c-ray, discriminating on the basis of the magnitude of the output of the PMT is equivalent to discriminating on the basis of c-ray energy. A multiplechannel analyzer (MCA), in which the term 'channel' refers to a specific energy range, uses an analogue-to-digital converter (ADC) to digitize the signal, and then to produce a pulse-height spectrum, i.e. a plot of the number of events from the PMTs as a function of the output voltage level. The number of channels in an

MCA can be more than a thousand, allowing essentially a complete energy spectrum to be produced. After digitization, the upper and lower threshold values for accepting the γ-rays are applied.

At first sight for clinical γ-cameras and SPECT modalities it might seem that only a single threshold voltage equivalent to a 140 keV (energy of ^{99m}Tc emitted photons) γ-ray which passes directly through tissue to the detector without scattering would suffice. However, γ-rays which have been scattered by only a very small angle still have useful information and so should be recorded. In addition, there are non-uniformities in the response of different parts of the NaI(Tl) crystal, and similarly with the PMTs, both of which will produce a range of output voltages even from mono-energetic γ-rays. Compton scattering of the γ-rays within the scintillation crystal itself also causes small and variable reductions in γ-ray energy. The energy resolution of the system is defined as the full-width-half-maximum (FWHM) of the photopeak and typically is about 14 keV (or 10%) for most gamma cameras without a patient present. The narrower the FWHM of the system the better it is at discriminating between unscattered and scattered γ-rays. In a clinical scan with the patient in place, the threshold level for accepting the 'photopeak' is set to a slightly larger value, typically 20%. For example, a 20% window around a 140 keV photopeak means that γ-rays with values of 127 to 153keV are accepted.

1.2.2 Radiotracers in SPECT Modality

In nuclear medicine scans a very small amount, typically nanogrammes (ng), of radioactive material called a radiotracer is injected intravenously into the patient. The agent then accumulates in specific organs in the body. In SPECT modality the most common radiotracers are chemical complexes of Technetium (^{99m}Tc), an element which emits mono-energetic γ-rays at 140 keV that end up in γ-Camera system. Various chemical complexes of ^{99m}Tc have been designed in order to target different organs in the body.

The ideal properties of a radiotracer for SPECT include:

  i.   A radioactive half-life that is short enough to produce significant radioactivity without requiring a very large initial dose, but not so short that there is significant decay before the required post-injection delay to allow the radiotracer to clear the blood and distribute in the relevant organs.
 ii.   Decay should be via emission of a mono-energetic c-ray without emission of alpha- or beta-particles. A mono-energetic c-ray allows discrimination between Compton scattered and unscattered c-rays, thereby improving image contrast. Alpha- or beta-particles are completely absorbed within tissue, therefore increasing the radioactive dose without giving any useful image information.
iii.   The energy of the c-ray should be greater than ~100 keV so that a reasonable proportion of c-rays which are emitted deep within the tissue have sufficient energy to travel through the body and reach the detector.
 iv.   The energy of the c-ray should be less than ~200 keV so that the rays do not penetrate the thin lead septa in the collimator (which is analogous to the antiscatter grid in X-ray imaging).

v. The radiotracer should have a high uptake in the organ of interest and relatively low non-specific uptake in the rest of the body. These two factors lower the required dose for the patient and increase the image contrast, respectively **[SMI11]**.

The most widely used radiotracer is ^{99m}Tc which is involved in over 90% of planar scintigraphy and SPECT studies. It exists in a metastable state, i.e. one with a reasonably long half-life (6.02 hours), and is formed from ^{99}Mo according to the decay scheme

$$\,^{99}_{42}\mathrm{Mo} \xrightarrow{\tau_{1/2}\,=\,66\,\mathrm{hours}} \,^{0}_{1}\beta + \,^{99m}_{43}\mathrm{Tc} \xrightarrow{\tau_{1/2}\,=\,6\,\mathrm{hours}} \,^{99g}_{43}\mathrm{Tc} + \gamma$$
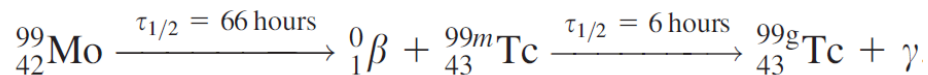
The energy of the emitted c-ray is 140 keV. It is important to note that this is a mono-energetic emission, unlike the wide spectrum of energies of X-rays produced by an X-ray source.
Other useful radiotracers used in SPECT modality are shown in *Table 1.2*, with their properties along with the corresponding clinical applications that they are introduced in.

Radiotracer	Half-life (hours)	γ-ray energy (keV)	Clinical application
^{99m}Tc	6.0	140	various
^{67}Ga	76.8	93, 185, 300, 394	tumour detection
^{201}Tl	72	167, 68–82 (X-rays)	myocardial viability
^{133}Xe	127.2	81	lung ventilation
^{111}In	67.2	171, 245	inflammation

Table 1.2. *Commonly used radiotracers in SPECT modality with their properties and the clinical applications in which they are introduced.*

1.3 Positron Emission Tomography (PET)

Similar to SPECT, Positron Emission Tomography (PET) is a tomographic technique which also uses radiotracers. However, PET has between 100 and 1000 times higher SNR as well as significantly better spatial resolution than SPECT. The fundamental difference between the two imaging techniques is that the radiotracers used in PET emit positrons which, after annihilation with an electron in tissue, result in the formation of two γ-rays with energies of 511 keV each. These two γ-rays have trajectories 180° apart and strike solid-state detectors which are positioned in a series of complete rings around the patient. This forms an intrinsic line-of-reconstruction (LOR) without the need for any collimation. The much higher SNR of PET compared to SPECT arises from several factors including: (i) collimation not being required, (ii) reduced attenuation of higher energy (511 keV vs. 140 keV) c-rays in tissue, and (iii) the use of a complete ring of detectors. In the past five years, stand-alone PET scanners have largely been replaced with hybrid PET/CT scanners which use a single patient bed to slide between the two systems (*Figure 1.6*). The rationale for the hybrid system is similar to that for SPECT/CT, namely improved attenuation correction and the ability to fuse morphological and functional information.

A general schematic illustration of PET modality is shown in *Figure 1.7*. The detectors (typically many thousands) consist of small crystals of Bismuth Germanium (BGO), which are coupled to PMTs: the resulting output voltages are then digitized. After correction of the acquired data for accidental coincidences and attenuation effects using the CT images, the PET image is reconstructed using either filtered backprojection or iterative methods. The most recent technical innovation in commercial PET/CT scanners is time-of-flight (TOF) technology, in which the SNR is improved by very accurate measurement of the exact time at which each γ-ray hits the detector **[SMI11]**.

Figure 1.6. *A commercial clinical PET/CT device.*

 PET/CT has its major clinical applications in the general areas of oncology, cardiology and neurology. In oncology, whole body imaging is used to identify both primary tumors and secondary metastatic disease remote from the primary source. The major disadvantages of PET/CT are the requirement for an on-site cyclotron to produce positron emitting radiotracers, and the high associated costs.
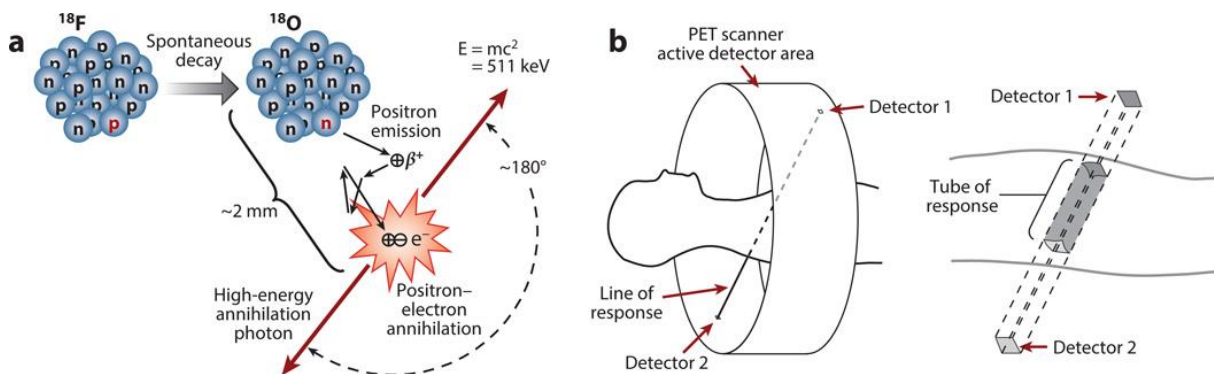
Figure 1.7. *A schematic illustration of PET modality, where we exploit the annihilation of a β+ with an electron in tissue with the parallel formation of 2 γ photons that are emitted in 180° apart (a) and a figure of PET imaging process (b). (Figure taken from* Juan José Vaquero *and* Paul Kinahan: *'Positron Emission Tomography: Current Challenges and Opportunities for Technological Advances in Clinical and Preclinical Imaging Systems',*2015, **[VAQ15]***)*

1.3.1 Instrumentation for PET

The instrumentation in PET modality is significantly different from this used in SPECT technique, even though there are similar components such as multi-channel pulse height analyzers and photomultiplier tubes. PET system is consisted of thousands small solid-state detectors and additional annihilation coincidence circuits.

Although the NaI(Tl) scintillation crystals can be used in PET technique, they have a low detection efficiency at 511keV, meaning that the crystal would have to be very thick for high SNR and this would result in poor spatial resolution. The ideal detector crystal has:

  i.   a high c-ray detection efficiency,
  ii.   a short decay time to allow a short coincidence resolving time to be used,
  iii. a high emission intensity (the number of photons per detected c-ray) to allow more crystals to be coupled to a single PMT, reducing the complexity and cost of the PET scanner,
  iv.   an emission wavelength near 400 nm which corresponds to the maximum sensitivity for standard PMTs,
  v.   optical transparency at the emission wavelength, and
  vi.   an index of refraction close to 1.5 to ensure efficient transmission of light between the crystal and the PMT.

In the majority of the commercial PET scanners BGO detectors are used, since BGO has a high density and effective atomic number giving it a high linear attenuation coefficient and hence high efficiency. The major disadvantage of BGO is its low emission intensity, meaning that a maximum of 16 crystal elements can be coupled to each PMT. An alternative material, LSO(Ce), has a much higher intensity and almost as high an efficiency, and is currently being commercially integrated into newer systems, particularly time-of-flight (TOF) scanners for which its very short decay time is highly advantageous. A third material, GSO(Ce), is also used in some PET/CT systems. BaF_2 has the shortest decay time, but has not yet found widespread commercial utility.

Detection of the anti-parallel γ-rays uses a large number of scintillation crystals which are placed in a circular ring surrounding the patient. Coupling each crystal to a single PMT would give the highest possible spatial resolution but would also increase the cost prohibitively. Modern PET scanners are based upon a 'block detector' design, which consists of a large block of BGO (dimensions ~50×50×30 mm) which has a series of partial cuts through it, with the cuts filled with light-reflecting material. The cuts prevent light which is formed at the top of the crystal from producing a very broad light spread function by the time the photon has passed through the entire 30 mm depth. An eight-by-eight array of partial cuts is produced, and each block can be considered to contain effectively 64 separate detectors, each with dimensions ~6×6 mm with a depth of 30 mm. Four PMTs are coupled to each BGO block and localization of the detected γ-ray to a particular crystal is performed using the Anger principle.

When a γ-ray hits a BGO or LSO(Ce) detector crystal it produces a number of photons. These photons are converted into an amplified electrical signal, at the output of the PMT, which is fed into a multichannel analyzer. If the voltage is within a pre-determined range, then the pulse height analyzer generates a 'logic pulse', which is sent to the coincidence detector: typically, this logic pulse is 6–10 ns long. The energy resolution of BGO crystals is ~20%, so the energy window set for acceptance is typically 450–650 keV.

1.3.2 Radiotracers in PET Modality

Positron emission tomography (PET) is a powerful molecular imaging modality, which when applied with specific radiopharmaceuticals can deliver quantitative measures of biochemical parameters, such as the concentrations or functions of neurotransmitter receptors, transporters or enzymes in living subjects, including humans.

Isotopes such as ^{11}C, ^{15}O, ^{18}F and ^{13}N used in PET undergo radioactive decay by emitting a positron, i.e. a positively charged electron (e+), and a neutrino:

$$^{18}_{9}\text{F} \rightarrow {}^{18}_{8}\text{O} + \text{e}^{+} + \text{neutrino}$$

$$^{11}_{6}\text{C} \rightarrow {}^{11}_{5}\text{B} + \text{e}^{+} + \text{neutrino}.$$
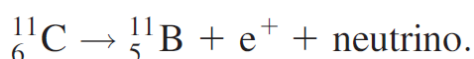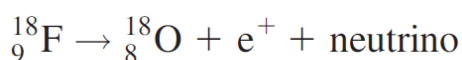
PET is commonly applied to studies of the brain for example, and the required radiopharmaceuticals are usually labeled with one of the short-lived positron-emitters, Carbon-11 ($T_{1/2}$ = 20 min) or Fluorine-18 ($T_{1/2}$ = 110 min). The classic example is 2-[18F]Fluoro-2-Deoxy-D-Glucose (FDG), which enters the brain by the action of a glucose transporter and is then phosphorylated by hexokinase to give the 18F-labeled 6-phosphate [PIK09].

What is happen with the radiotracers used in PET is that the positron travels a short distance (an average of 0.1–2 mm depending upon the particular radiotracer) in tissue before annihilating with an electron. This annihilation results in the formation of two γ-rays, each with an energy of 511keV. In *Table 1.3* a list with the most commonly used radiotracers in PET is shown including their clinical applications and their half-life time.

Radionuclide	Half-life (minutes)	Radiotracer	Clinical applications
^{18}F	109.7	^{18}FDG	oncology, inflammation, cardiac viability
^{11}C	20.4	^{11}C-palmitate	cardiac metabolism
^{15}O	2.07	$H_2{}^{15}$O	cerebral blood flow
^{13}N	9.96	^{13}NH$_3$	cardiac blood flow
^{82}Rb	1.27	^{82}RbCl$_2$	cardiac perfusion

Table 1.3. *A list with the most common radiotracers used in PET modalities and some of their properties.*

Radiotracers for PET must be synthesized on-site using a cyclotron, and are structural analogues of biologically active molecules in which one or more of the atoms have been replaced by a radioactive atom. The only PET radiotracer that can be produced from an on-site generator rather than a cyclotron is $_{82}$Rb. The process uses $_{82}$Sr as the parent isotope, which has a half life of 600 hours. The physical set-up is quite similar to the Technetium generator, with the $_{82}$Sr adsorbed on stannic oxide in a lead-shielded column. The column is eluted with NaCl solution, and the eluent is in the form of rubidium chloride which is injected intravenously [SMI11].

1.4 General Imaging Characteristics

The accuracy of clinical diagnoses depends critically on image quality. The higher the quality of the image is the more accurate the diagnosis is. Improvements in imaging techniques and instrumentation have revolutionized early diagnosis and treatment of a number of different pathological conditions. Each new imaging technique or change in instrumentation must be carefully assessed in terms of its effect on diagnostic accuracy. For this purpose many studies at clinical and preclinical level take place.

1.4.1 Spatial Resolution

What is called spatial resolution of an imaging system is the minimum distance between two different objects that the objects can be individually distinguished rather than appearing as one larger formation. The two most common measures in the spatial domain are the line spread function (LSF) and point spread function (PSF).

Since the imaging system is not perfect, it introduces some degree of blurring into the image, and so the line in the image does not appear as sharp as its actual physical shape. The degree of blurring can be represented mathematically by a line-spread function (LSF). The LSF of an imaging system is estimated by measuring a one-dimensional projection and the width of the LSF is usually defined by a parameter known as the full-width-at-halfmaximum (FWHM) (*Figure 1.8.*).

The LSF describes system performance in one dimension. However, in some imaging modalities, for example nuclear medicine, the spatial resolution becomes poorer the deeper the location within the patient from which the signal is received. Therefore, a full description of the spatial resolution of an imaging system requires a three-dimensional formulation: the three-dimensional equivalent of the LSF is termed the point spread function (PSF) (*Figure 1.8*). As the name suggests, the PSF describes the image acquired from a very small 'point source'. In a perfect imaging system, the PSF would be a delta function in all three dimensions, in which case the image would be a perfect representation of the object. In practice, the overall PSF of a given imaging system is a combination of detection instrumentation and data sampling and can be calculated by the convolution of all of the individual components **[SMI11]**. That means that for each point (x, y) there is a function 'Ψ'(x, y; a, b) so that the reconstructed image at (x, y) is given **[EPS08]** by

$$f_\Psi(x, y) = \int_{\mathbb{R}^2} \Psi(x, y; a, b) f(a, b) \, da \, db \qquad (1.1).$$

LSF   **PSF**
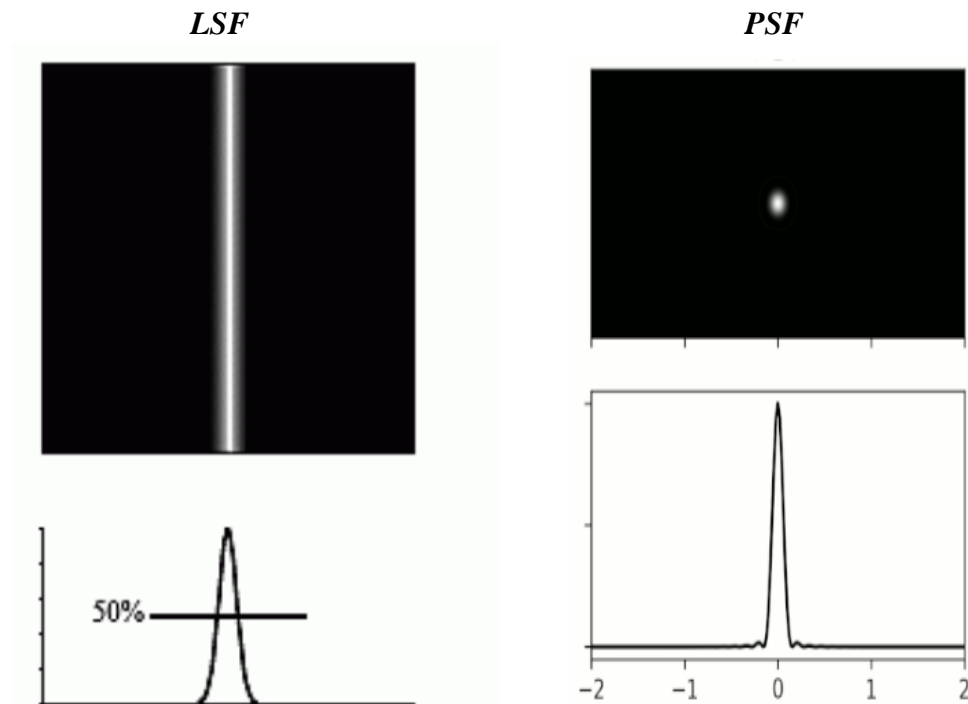
Figure 1.8. *Line Spread Function (LSF) effect on a line source (left) and Point Spread Function (PSF) effect on a point source (right).*

1.4.2 Energy Resolution

Another important factor that affects the quality of the recorded clinical image in each nuclear medicine imaging modality is the Energy Resolution of the system. Energy resolution is the ability of the detector to accurately determine the energy of the incoming radiation. Since no camera system is perfect, no system is capable of determining precisely what energy photon struck the crystal. Instead, the system can only determine within a range of values, what energy radiation it is detecting. The energy resolution is expressed as a percent of the energy of the incoming photons.

If the energy resolution of a camera is 10%, and only 140 KeV photons are striking the crystal, the system will "see" photons ranging from 133 KeV to 147 KeV. That is, it can only determine to within 14 KeV, what the actual incoming energy really is. Energy resolution is a very important parameter in determining the overall performance of a gamma camera, because it is the parameter, which allows a camera to differentiate between primary photons and Compton scattered photons. This ultimately determines the spatial resolution of the system. An important measurement to assess the efficiency of the scintillation counting equipment in a Nuclear Medicine department is the Full Width at Half Maximum (FWHM), which should typically be less than 10%.

The energy resolution depends on the system of the scintillation crystal and the photomultiplier tube. The photomultiplier is coupled to the scintillator which emits light pulses in response to γ-radiation and the average quantity of light per pulse is proportional to the radiation energy dissipated in the scintillator. So, energy resolution is a characteristic of a scintillation counter as a whole, not of the photomultiplier by itself; the contributions of the scintillator and photomultiplier are not independent of each other and cannot be treated separately **[FLY02]**.

1.4.3 Artifacts

The term 'artifact' refers to any signal in an image which is caused by a phenomenon related to the imaging process, but which distorts the image or introduces an apparent feature which has no physical counterpart.

Ensuring quantitative accuracy requires estimating these confounding effects. Artifacts include, in rough order of effect size, attenuation; random coincidences; scattered coincidences; patients' movements; geometry-based variations in efficiency; the system's dead time; radioisotope decay time and branching ratio; detector resolution; and variations specific to the detector element in efficiency, signal gain, coincidence timing, energy resolution, and event positioning [VAQ15].
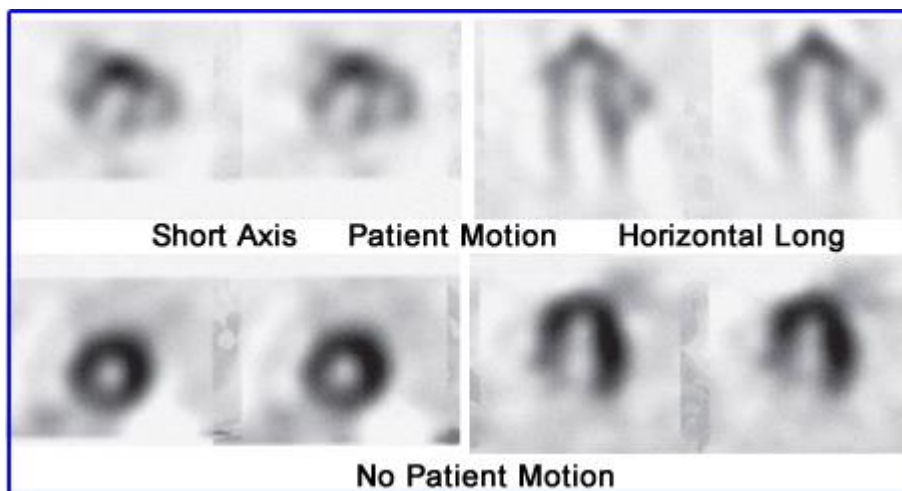
Figure 1.9. How a clinical image seems with artifacts because of patient motion and without.

In addition, a common spatial distortion in a small field γ-camera imaging, which is basically used at preclinical level, is this called barreloid effect that the camera's limited field of view causes. Moreover, non-uniformity of the photon intensity may be observed in planar images which should be calculated and corrected.
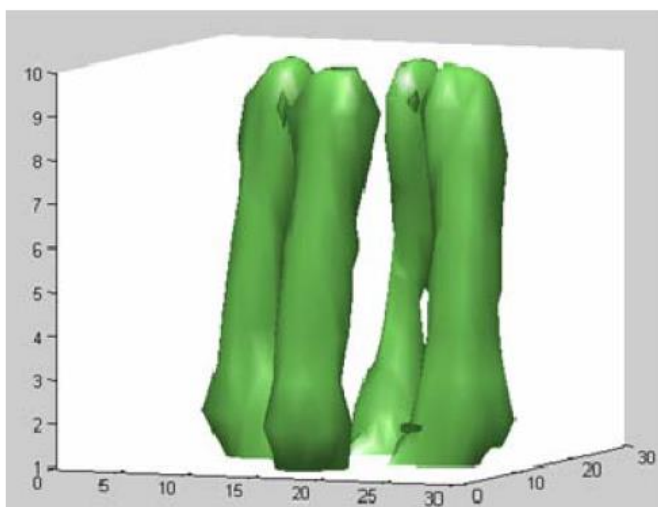
Figure 1.10. How four capillaries seem in a reconstructed tomographic image taken with a small-field γ-Camera. Their curvature is the result of the barreloid effect. (Figure taken from D. Thanasas, D. Maintas, E. Georgiou et al.: 'Correcting Spatial Distortion and non-Uniformity in Planar Images from γ-Camera Systems', 2008, [THA08])

Recognizing the causes of such artifacts and of course eliminating these is an important task for exploiting only the necessary information of each image. In this field various studies take place not only at clinical but also at preclinical level, in order to fabricate useful correction techniques that can improve each imaging system's performance individually.

Thus, in the following sections of this thesis, a complete study of a small field γ-Camera used in SPECT modality is introduced. The aforementioned system is optimized for ^{99m}Tc at preclinical level. The characterization of the camera starts with the determination of the inner spatial and energy resolution of its main component, the position sensitive photomultiplier tube (PSPMT).

Chapter II

Inner Spatial and Energy Resolution of the HAMAMATSU R2486 PSPMT

2.1 Operating Principle of a HAMAMATSU R2486 PSPMT

 HAMAMATSU R2486 PSPMT is a cylindrical position sensitive photomultiplier tube (PSPMT) with 3" diameter. It is composed of a photocathode, a 12 stage coarse mesh dynode structure and 32 crossed-wired anodes that are arranged into two orthogonal groups X and Y, as shown in *Figure 2.1*.
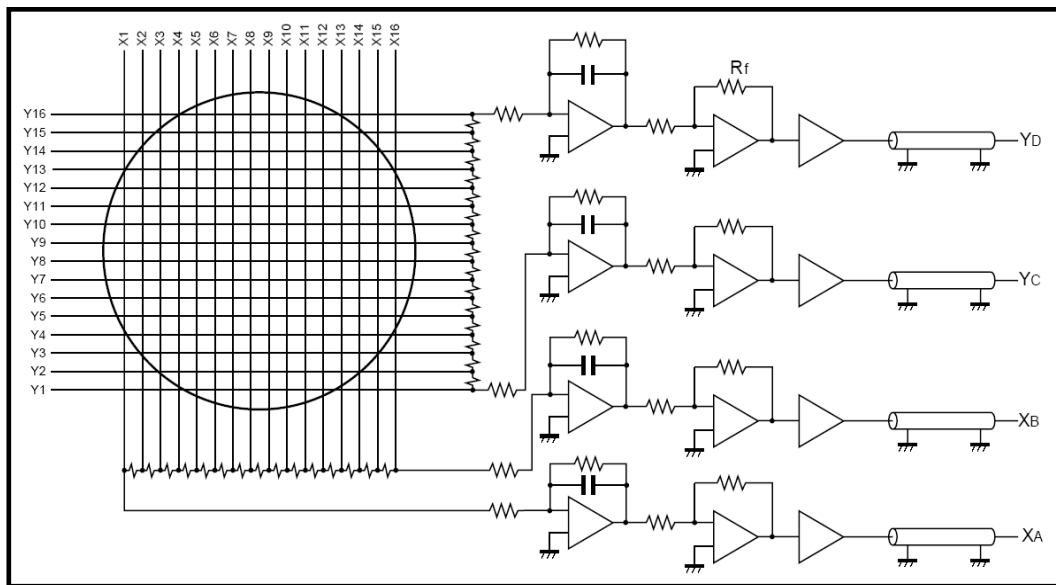
Figure 2.1. *Scheme of 16+16 orthogonally positioned anodes X and Y ending up, through a resistive chain (a charge divider), in 4 analogue signals (X_A, X_B, Y_C, Y_D).*

 The output wires of the anodes end up in a network of resistances, a charge divider, and as a result we have 4 analogue signals (X_A, X_B, Y_C, Y_D) from the 32 initially extracted. The total energy, as well as the position of the incident to the PSPMT photons can be reconstructed from these 4 signals. Specifically, the total energy of each photon is proportional to the total charge accumulated and the position at each axis can be reconstructed from the normalized difference of the two corresponding signals as the following relationships **[POL06]** are shown:

$$X - Position: \quad X \sim (X_A - X_B) / (X_A + X_B)$$
$$Y - Position: \quad Y \sim (Y_C - Y_D) / (Y_C + Y_D)$$
$$Energy: \quad Q \sim (X_A + X_B) + (Y_C + Y_D)$$

 There is also an analog to digital converter (ADC) which is included in a PCI card and digitizes the signals with a maximum rate of 20 MHz, which means 1 point per 50ns. After applying a correction algorithm for the minimum of the pulse, its final shape takes the following form:
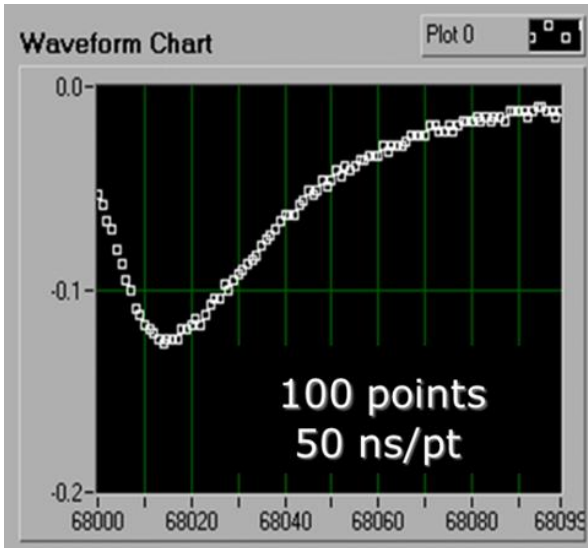
Figure 2.2. *The final form of the output pulse.*

2.2 Inner Spatial And Energy Resolution Of The PSPMT

2.2.1 1st Set Of Measurements

In order to extract the inner spatial and energy resolution of the Position Sensitive PhotoMultiplier Tube (PSPMT) we used a plexiglass with the same diameter with our PSPMT and in contact with it, which is consisted of 21 equidistant holes of 1mm in diameter, where we put an optical fiber. The fiber voltage was set at 1.5 V, its pulse width at 1μs and the high voltage of the PSPMT at 900V.
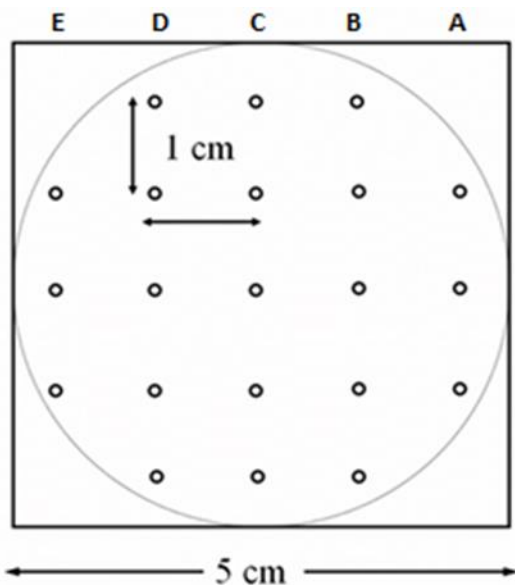
Figure 2.3. *The plexiglass geometry for the 21 equidistant fiber supporting holes.*
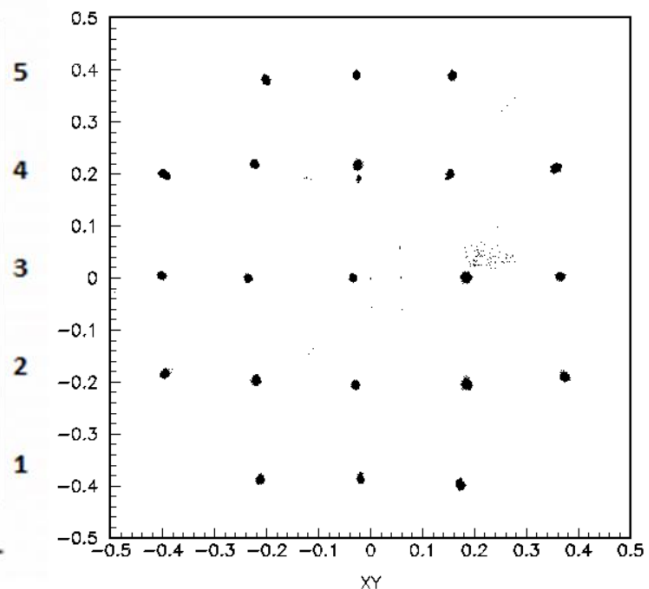
Figure 2.4. *The recorded image for all the different positions of the supporting plexiglass.*

For every single position of the optical fiber its mean X and Y and their width respectively were recorded. Moreover the mean accumulated charges Q_x and Q_y and their widths were recorded, as well as the corresponding values of the total charge Q_{xy} .All these values are included in the following table.
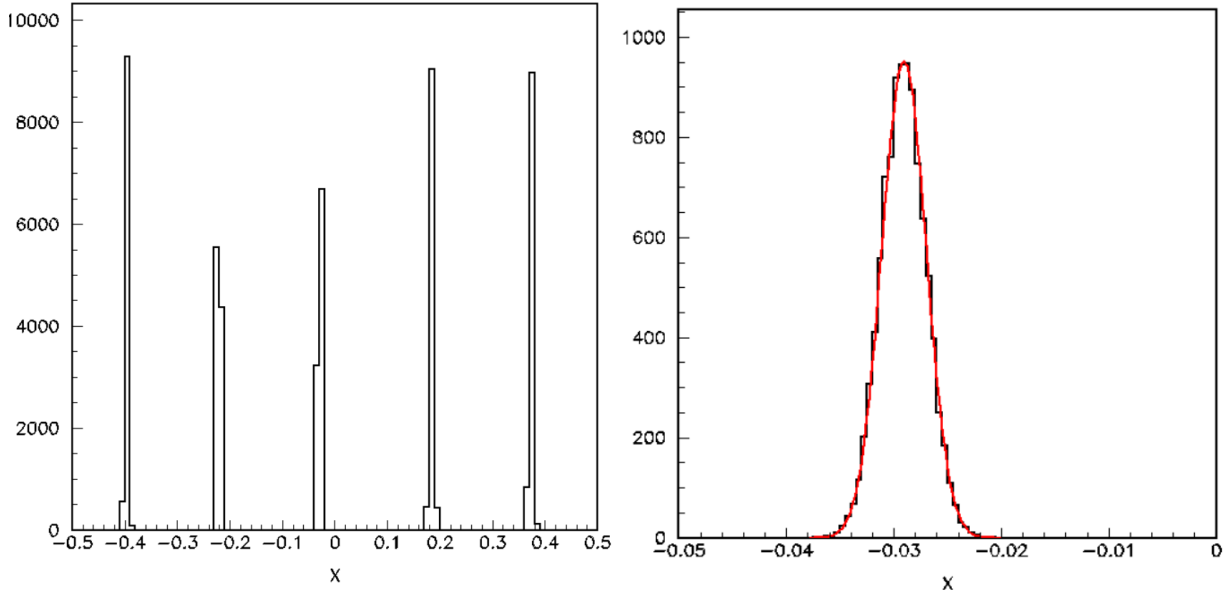
Figure 2.5. *X projection of a slice of the recorded planar image (Left) and a Gaussian fitting on a recorded spot in order to find its mean X position value (Right).*

The analyzed values of the position and the charge of the first set of measurements are represented in the following table in wire-coordinates and arbitrary units (a.u.).

HOLE	X(a.u)		Y(a.u)		Qx(a.u)		Qy(a.u)		Qxy(a.u)	
	Mean	RMS	Mean	RMS	Mean	RMS	Mean	RMS	Mean	RMS
B1	0.1725	0.0024	-0.3982	0.0027	410.2	9.4	419.1	9.5	414.6	9.4
C1	-0.0195	0.0019	-0.3864	0.0023	497.1	10.5	490.1	10.3	493.6	10.4
D1	-0.2123	0.0022	-0.3878	0.0025	459.8	9.6	463.2	9.6	461.4	9.6
A2	0.3737	0.0027	-0.1905	0.0023	428.9	9.7	436.6	9.7	432.7	9.7
B2	0.1850	0.0029	-0.2051	0.0030	338.1	7.8	332.1	7.5	335.0	7.6
C2	-0.0291	0.0021	-0.2063	0.0023	470.3	9.4	450.5	8.9	460.3	9.1
D2	-0.2203	0.0024	-0.1970	0.0026	441.9	9.2	423.2	8.7	432.5	8.9
E2	-0.3961	0.0025	-0.1844	0.0022	475.6	10.3	462.7	9.9	469.1	10.1
A3	0.3653	0.0024	0.0027	0.0020	470.9	10.4	476.9	10.4	473.8	10.4
B3	0.1842	0.0029	0.0008	0.0028	346.3	7.7	338.4	7.4	342.3	7.5
C3	-0.0336	0.0020	0.0001	0.0021	497.7	9.6	478.4	9.1	489.0	9.4
D3	-0.2355	0.0021	-0.0009	0.0020	480.5	9.6	464.3	9.2	472.4	9.4
E3	-0.4018	0.0024	0.0045	0.0020	471.2	10.5	470.8	10.4	471.0	10.4
A4	0.3570	0.0028	0.2114	0.0026	423.6	9.4	413.4	9.0	418.4	9.1

B4	0.1535	0.0020	0.2006	0.0022	371.8	10.5	350.8	10.0	361.2	10.3
C4	-0.0247	0.0023	0.2176	0.0027	431.3	9.0	404.6	8.4	417.9	8.7
D4	-0.2235	0.0023	0.2189	0.0024	462.8	9.9	445.6	9.4	454.1	9.6
E4	-0.3989	0.0031	0.2000	0.0025	479.3	10.3	477.1	10.3	478.1	10.3
B5	0.1574	0.0023	0.3894	0.0026	450.3	9.9	452.1	9.8	451.1	9.9
C5	-0.0273	0.0020	0.3900	0.0024	488.0	10.7	466.6	10.1	477.2	10.4
D5	-0.2016	0.0022	0.3810	0.0027	452.2	10.1	447.5	9.9	449.8	10.0

__Table 2.1.__ Measurements of the 1ˢᵗ set.

Considering the fiber non-dimensional and knowing the real position of each hole in which the fiber was put in order to record its light-pulse, we found (with the use of Mathcad) not only the mean width of each hole at the X and Y axis (taking into account all possible combinations of each sign with the other 20) but also the mean width of X and Y values and their deviations of all the 21 holes, which are:

$$<FWHM>_x = 0.124 \pm 0.009 mm \quad \& \quad <FWHM>_y = 0.123 \pm 0.051 mm$$

More specifically, in order to smoothen distortions such as the barrel observed and be more accurate, we took the mean measured width of X and Y values of two different holes and we found the ratio of the difference between their real positions in mm to the difference between their measured mean X or Y values multiplied by the corresponding deviation. We did that process for every possible combination with the requirement not to be holes with the same X or Y real position when this difference is zero and enters the fraction counter. We found the "weighted average" of the position for every single hole.

$$<Xi> = \frac{(Xi-Xj)real}{(Xi-Xj)measured} \times RMSx_i \quad \& \quad <Yi> = \frac{(Yi-Yj)real}{(Yi-Yj)measured} \times RMSy_i$$

So for each hole we took its mean X and Y position in mm.

Hole	X(mm)	Hole	X(mm)	Hole	X(mm)	Hole	X(mm)	Hole	X(mm)
		A2	0.137	**A3**	0.124	**A4**	0.149		
B1	0.125	**B2**	0.148	**B3**	0.148	**B4**	0.108	**B5**	0.124
C1	0.102	**C2**	0.109	**C3**	0.104	**C4**	0.119	**C5**	0.104
D1	0.115	**D2**	0.124	**D3**	0.107	**D4**	0.119	**D5**	0.118
		E2	0.135	**E3**	0.127	**E4**	0.166		

__Table 2.2.__ The mean X value in mm for each of 21 holes in which we put the fiber.

Hole	Y(mm)	Hole	Y(mm)	Hole	Y(mm)	Hole	Y(mm)	Hole	Y(mm)
		A2	0.117	A3	0.100	A4	0.131		
B1	0.135	B2	0.149	B3	0.140	B4	0.112	B5	0.137
C1	0.119	C2	0.114	C3	0.105	C4	0.135	C5	0.126
D1	0.128	D2	0.131	D3	0.100	D4	0.120	D5	0.146
		E2	0.114	E3	0.100	E4	0.128		

Table 2.3. The mean Y value in mm for each of 21 holes in which we put the fiber.
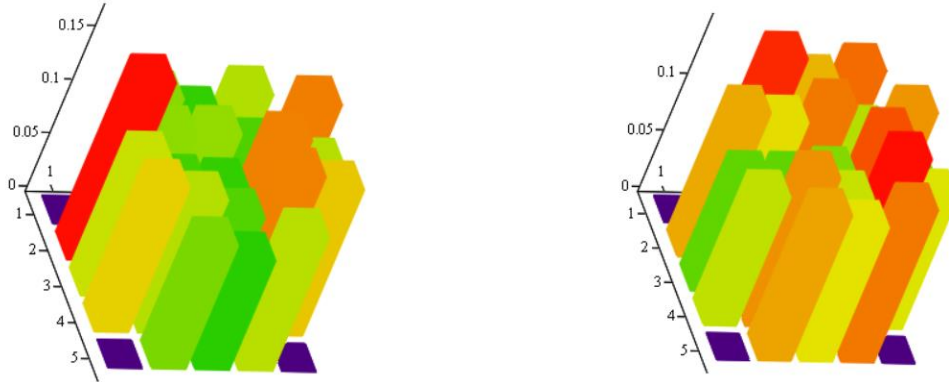
Figure 2.6. The mean width of X (on the left) and Y (on the right) position in mm for all the 21 holes of the plexiglass used.

As far as the energy resolution of the PSPMT it concerns, it is inversely proportional to $\Delta E/E$ ratio which is represented by the ratio $\Delta Q/Q$, where ΔQ is the full width at half maximum (FWHM) of the probability of the anode charge fluctuations and Q the mean anode charge per pulse **[FLY02]**. So, in our measurements we can see that the inner energy resolution of the photomultiplier shows a small increase as we approach the central C_3 point.

Hole	$(\Delta Q/Q)_y$ %	$(\Delta Q/Q)_x$ %	$(\Delta Q/Q)_{xy}$%
B1	2.26	2.30	2.28
C1	2.10	2.11	2.10
D1	2.07	2.09	2.08
A2	2.21	2.27	2.24
B2	2.25	2.30	2.27
C2	1.96	2.00	1.98
D2	2.05	2.08	2.06
E2	2.13	2.16	2.14
A3	2.17	2.21	2.19
B3	2.18	2.23	2.22
C3	1.91	1.93	1.92
D3	1.99	2.00	1.99
E3	2.20	2.23	2.21
A4	2.17	2.21	2.19

B4	2.86	2.82	2.84
C4	2.08	2.08	2.08
D4	2.11	2.14	2.12
E4	2.15	2.16	2.15
B5	2.17	2.20	2.19
C5	2.17	2.19	2.18
D5	2.21	2.23	2.22

Table 2.4. *The ΔQ/Q ratio corresponds to the energy resolution of the PSPMT. The more the ratio is decreased the more the energy resolution is increased.*

2.2.2 2nd Set Of Measurements

During this set of measurements we have just changed the conditions of the experiment. In particular we repeated the same kind of measurements as those of the 1st set, with the exception of the high voltage of the PSPMT, that now was 850V, and the pulse width which was 500ns. The results that these set gave us are:

$$\langle FWHM \rangle_x = 0.178 \pm 0.009\,mm \quad \& \quad \langle FWHM \rangle_y = 0.181 \pm 0.078\,mm$$

The inner spatial resolution of the PSPMT obviously depends not only on the high voltage of the photomultiplier but also on the pulse duration, which essentially simulates the brightness of a scintillator crystal that is used in a γ-camera system. So, the FWHM under these conditions is shown apparently increased, as expected, and the spatial resolution reduced.

HOLE	X(a.u)		Y(a.u)		Qx(a.u)		Qy(a.u)		Qxy(a.u)	
	Mean	RMS	Mean	RMS	Mean	RMS	Mean	RMS	Mean	RMS
B1	0.1752	0.0034	-0.3942	0.0036	373.6	13.9	389.8	14.1	381.7	14.0
C1	-0.0165	0.0025	-0.3822	0.0030	450.8	15.6	454.6	15.5	452.6	15.5
D1	-0.2116	0.0029	-0.3864	0.0032	410.7	14.2	425.6	14.5	418.1	14.3
A2	0.3762	0.0038	-0.1905	0.0031	392.7	14.3	405.2	14.6	398.9	14.4
B2	0.1867	0.0043	-0.2063	0.0041	303.2	11.6	303.8	11.4	303.4	11.5
C2	-0.0263	0.0029	-0.2055	0.0032	422.2	14.0	413.1	13.5	417.6	13.7
D2	-0.2198	0.0033	-0.1983	0.0035	385.8	13.0	377.6	12.7	381.6	12.8
E2	-0.3953	0.0033	-0.1890	0.0031	414.7	14.7	411.8	14.3	413.1	14.5
A3	0.3662	0.0034	0.0031	0.0027	425.3	15.3	439.4	15.6	432.3	15.4
B3	0.1885	0.0055	0.0005	0.0046	301.6	11.2	302.1	11.2	301.8	12.1
C3	-0.0286	0.0028	-0.0022	0.0029	450.3	14.1	444.2	13.8	447.2	13.9

D3	-0.2284	0.0028	-0.0040	0.0030	443.3	14.5	438.9	14.2	441.0	14.5
E3	-0.3967	0.0031	-0.0001	0.0027	437.9	15.8	445.5	15.9	441.6	15.9
A4	0.3527	0.0043	0.2036	0.0036	395.8	14.1	390.1	13.8	392.9	13.9
B4	0.1762	0.0043	0.2128	0.0049	320.9	12.1	307.7	11.5	314.2	11.8
C4	-0.0208	0.0033	0.2094	0.0045	380.4	12.6	363.5	11.9	371.9	12.2
D4	-0.1958	0.0035	0.1861	0.0035	470.9	15.4	462.1	15.0	466.4	15.2
E4	-0.4145	0.0034	0.2045	0.0032	424.7	15.4	430.1	15.2	427.3	15.3
B5	0.1645	0.0034	0.3993	0.0037	398.8	14.5	410.7	14.7	404.7	14.6
C5	-0.0284	0.0027	0.3940	0.0035	443.7	16.3	435.1	15.7	439.3	16.0
D5	-0.2148	0.0032	0.3890	0.0038	382.6	14.6	389.4	14.6	385.9	14.6

Table 2.5. *The recorded mean values of X, Y, Q_x, Q_y and Q_{xy} and their RMS for this set of measurements on which our analysis was based.*

Finally, as the pulse duration and the PSPMT's high voltage decrease, there is also a decrease in the photomultiplier's energy resolution (as the following table shows).

Hole	$(\Delta Q/Q)_y$ %	$(\Delta Q/Q)_x$ %	$(\Delta Q/Q)_{xy}$%
B1	3,62	3,72	3,67
C1	3,41	3,46	3,42
D1	3,41	3,46	3,42
A2	3,60	3,64	3,61
B2	3,75	3,83	3,79
C2	3,27	3,32	3,28
D2	3,36	3,37	3,35
E2	3,47	3,54	3,51
A3	3,55	3,60	3,56
B3	3,71	3,71	4,01
C3	3,11	3,13	3,11
D3	3,24	3,27	3,27
E3	3,57	3,61	3,60
A4	3,54	3,56	3,54
B4	3,74	3,77	3,76
C4	3,27	3,31	3,28
D4	3,22	3,27	3,26
E4	3,53	3,63	3,58
B5	3,58	3,64	3,61
C5	3,61	3,67	3,64
D5	3,75	3,82	3,78

Table 2.6. *The ΔQ/Q ratio corresponds to the energy resolution of the PSPMT*

2.2.3 3rd Set Of Measurements –ΔQ/Q Variation With The Variation Of The Pulse Duration

As we have already seen, the inner spatial resolution of the PSPMT changes with the variation of the pulse duration. The same happens with the energy resolution and the ratio ΔQ/Q too. In this set of measurements we studied which is exactly their dependence. We put the fiber only in C_3 central hole and its voltage was 1.5V. Moreover, the PSPMT was set at 1000V constantly and we just changed the pulse duration from 300ns to 1300ns, with a fixed step of 50ns and a record of 10000 events per measurement.
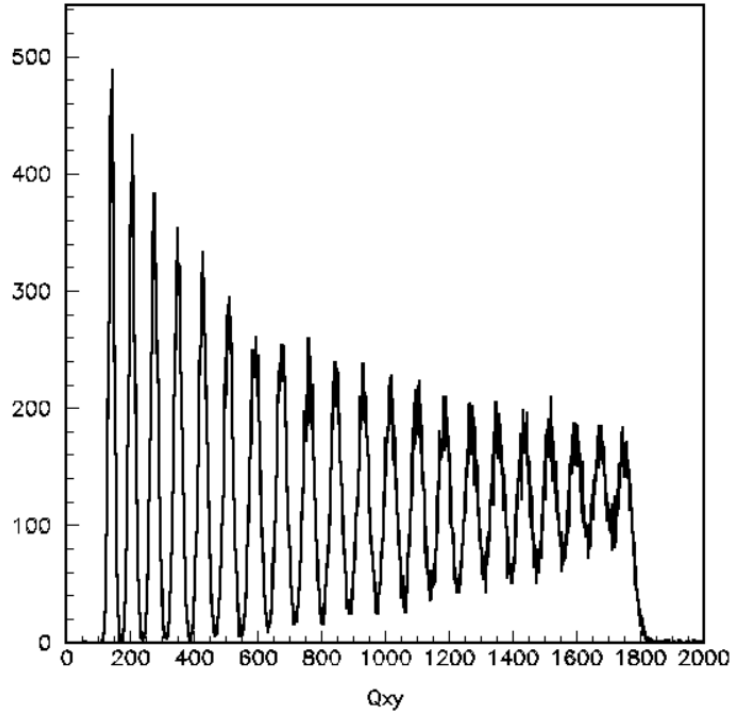
Figure 2.7. *Qxy records per 10000 events for the successively applied pulse duration. Equidistant peaks of the Energy records for each pulse duration.*

T(ns)	Qxy$_{mean}$ (a.u)	σ_Q	(ΔQ/Q)$_{xy}$%
300	141,7	8,63	14,342
350	206,0	9,92	11,340
400	276,4	11,02	9,389
450	350,8	11,92	8,002
500	428,7	13,06	7,174
550	509,2	13,98	6,465
600	593,0	15,11	6,000
650	676,6	15,97	5,558
700	761,5	16,91	5,229
750	846,8	17,34	4,822
800	932,7	17,95	4,532
850	1018,0	18,87	4,365

900	1103,0	19,48	4,159
950	1188,0	20,19	4,002
1000	1273,0	20,68	3,825
1050	1354,0	21,40	3,722
1100	1437,0	21,91	3,590
1150	1519,0	22,26	3,451
1200	1599,0	22,56	3,322
1250	1676,0	23,50	3,302
1300	1753,0	23,84	3,202

Table 2.7. *The Q_{xy} records and their σ for each pulse duration.*

From the sigma of the charge (σ_Q) we can calculate the ratio $\Delta Q/Q$, since the relationship between σ_Q and ΔQ is: $\underline{\boldsymbol{\Delta Q = 2\sqrt{2 \times LN(2)}\sigma_Q}}$. Moreover, the dependence of the charge accumulated (Q_{xy}), and by extension of the energy, on the duration of the pulse is linear, resulting in the peaks of the Energy records being equidistant. (*Figure 2.6, 2.7*).
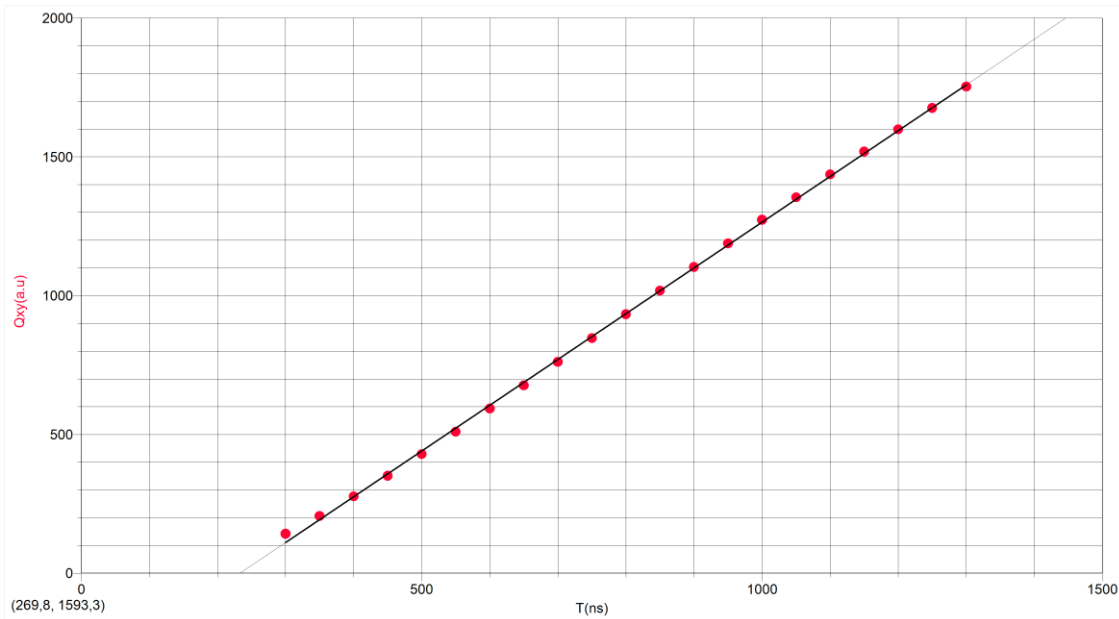
Figure 2.8. *The linear dependence of the charge accumulated on the duration of the pulse.*

In addition, by increasing the pulse duration, the ratio $\Delta Q / Q$ decreases, which results in an increase in the photomultiplier's energy response. It is known that energy resolution and as a result $\Delta Q/Q$ is proportional to $\frac{1}{\sqrt{E}}$ where E is the energy of the incident photon **[FLY02]** and this energy here is simulated by the pulse duration so $\frac{\boldsymbol{\Delta Q}}{\boldsymbol{Q}} \sim \frac{1}{\sqrt{\boldsymbol{T}}}$. As the below graph shows (*Figure 2.8*), the dependence of the ratio $\Delta Q/Q$ on the pulse duration actually takes the form:

$$\frac{\Delta Q}{Q} = \frac{A}{\sqrt{T}+B} \qquad\qquad (2.1).$$

25
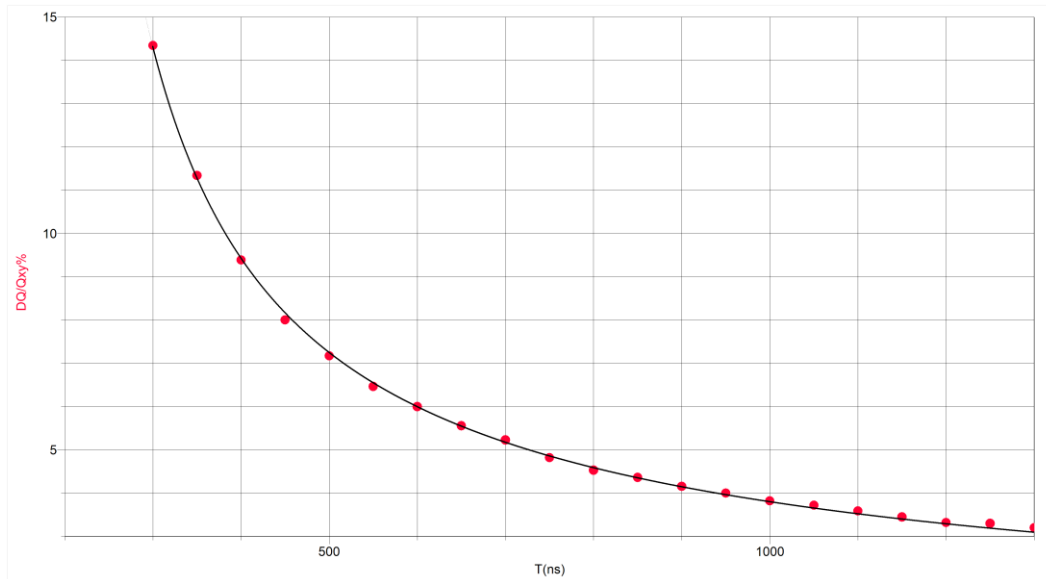
Figure 2.9. *The percentage charge fluctuation (DQ/Q) as a function of the pulse duration T.*

2.2.4 4th Set Of Measurements – *ΔQ/Q Variation With The Variation Of The PSPMT High Voltage*

Not only the pulse duration, but also the high voltage of the PSPMT affects its energy resolution. Specifically, as it is known by the literature, as the PSPMT's high voltage is increased the amplification of the charge through the dynodes and finally the total charge accumulated is increased too. This multiplier factor that shows exactly the final amplification of the charge that is collected by the cathode of our PSPMT is expected to depend on the PSPMT's high voltage, and this is what we study here.
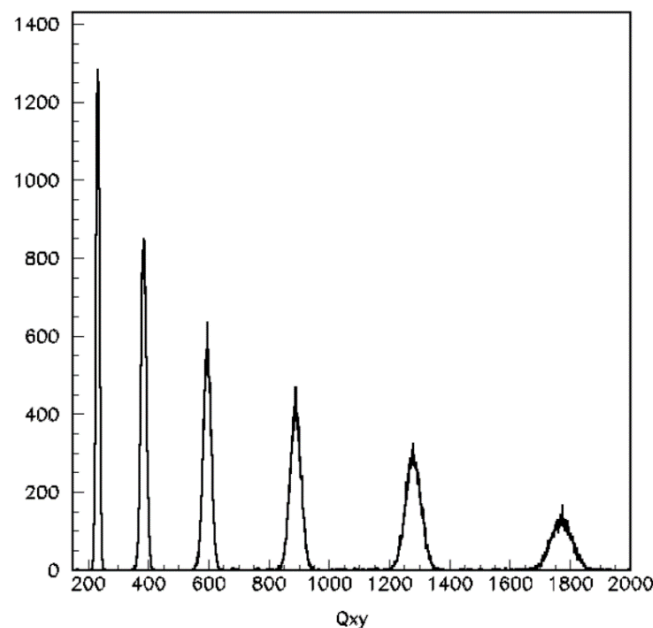
Figure 2.10. *Qxy records per 20000 events for the successively applied PSPMT's high voltage. Non-Equidistant peaks of the Energy records for each high voltage's value.*

For this set of measurements we put the fiber again in the C_3 central hole of our plexiglass, we kept the pulse duration at 500ns and we variated the PSPMT's high voltage from 800V to 1100V with a fixed step of 50V and a record of 20000 events per measurement. The total charge accumulated and the energy resolutions for each value of H.V. is shown in the following table.

H.V.(V)	Qxy$_{mean}$(a.u)	σ$_Q$	(ΔQ/Q)xy%
800	133,2	3,7	6,58
850	232,9	5,6	5,64
900	385,2	8,6	5,27
950	596,2	12,8	5,07
1000	889,6	17,9	4,74
1050	1280,0	25,1	4,61
1100	1772,0	34,5	4,58

Table 2.8. The Qxy records and their σ for each value of high voltage.

Now, the dependence of the charge accumulated (Q_{xy}) ,and by extension of the energy, on the PSPMT's high voltage is exponential, resulting in the peaks of the energies being non-equidistant (*Figure 2.10*)
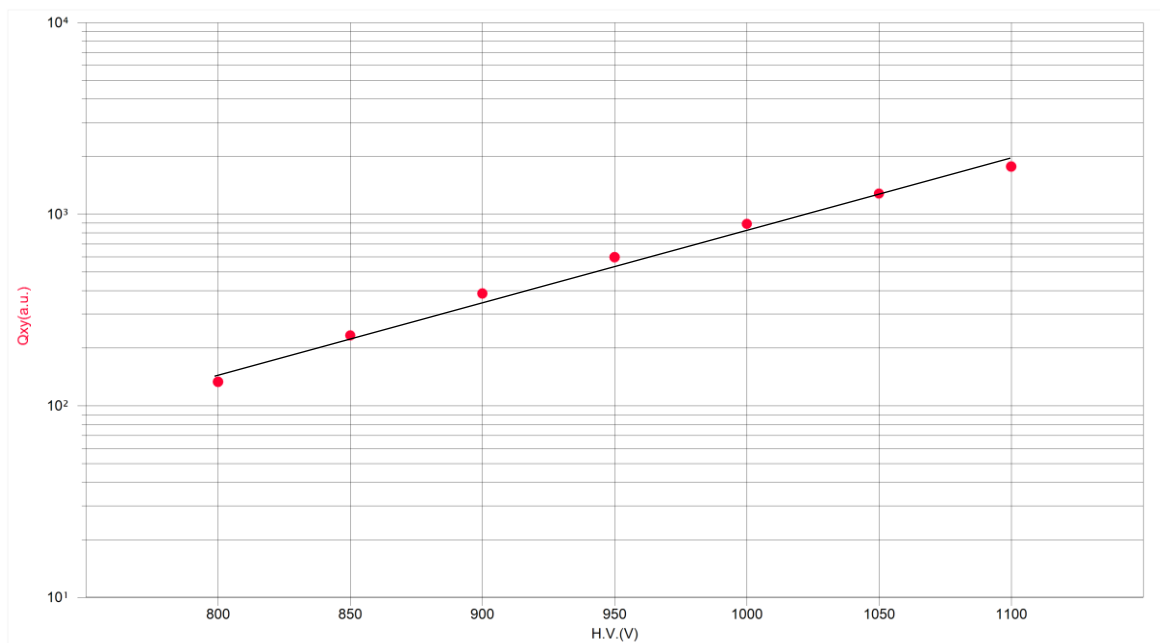
Figure 2.11. The relationship between the accumulated charge and the PSPMT's high voltage is exponential
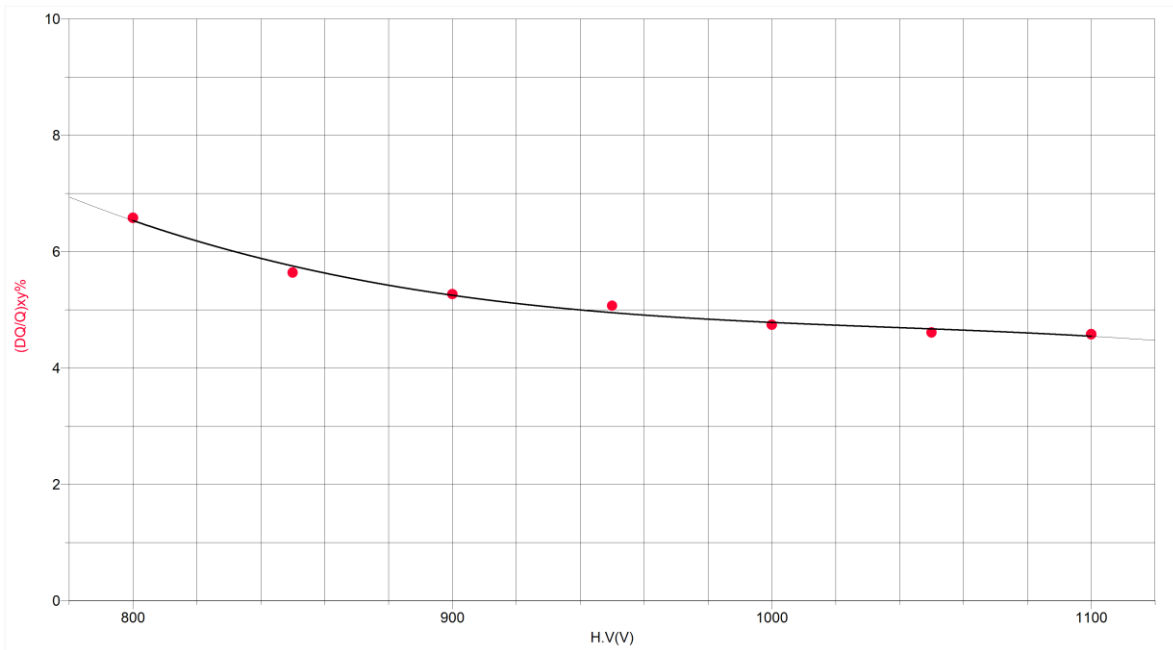
Figure 2.12. *As the DQ/Q ratio decreases with the high voltage increase, the energy resolution tends to be improved.*

As the *Figure 2.12* shows, although the PSPMT's high voltage increases, the energy resolution of the photomultiplier seems to be barely better. We have a 2% optimization for 300V increase (from 800V to 1100V) in the dynamic range of the photomultiplier.

2.3 How The Charge Gain Depends on PSPMT's High Voltage

An extra study here has to do with the gain of the charge accumulated, the multiplier factor, as a function of the applied PSPMT's high voltage. According to the Hamamatsu R2486 PSPMT manual, this gain is exponential function of the supply PSPMT's high voltage, as *Figure 2.12* is shown **[HAM10]**.
For this purpose, we performed three measurements regions based on the supply voltage and the pulse width, in order to avoid the overflow of the accumulated charge, which nevertheless had three measurements with the same voltage that only differed in the fiber's width . More specifically, we had the fiber in the central hole (C3),the fiber's voltage was 1.5V, the increase of the PSPMT's high voltage was with a fixed step of 10V and we took 10000 events per high voltage step.
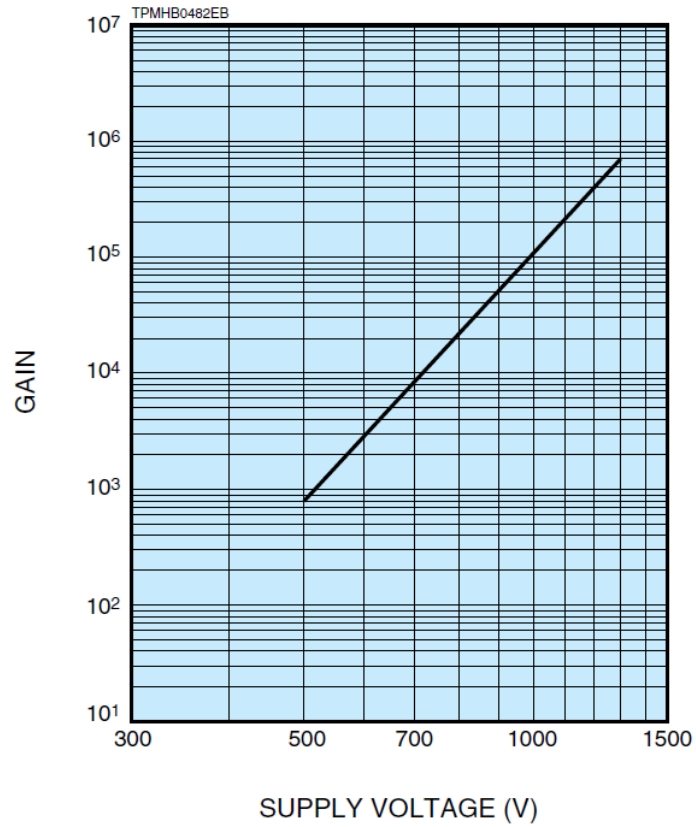
Figure 2.13. *The relationship between the supply voltage of the PSPMT and the gain in the total charge accumulated for a R2486 Hamamatsu PSPMT according to its manual.*

i.   1ˢᵗ measurement region

Pulse Width: 1150ns

PSPMT's High Voltage Width: 800-1020V

H.V(V)	Q(a.u)	H.V(V)	Q(a.u)	H.V(V)	Q(a.u)
800	270.2	880	596.1	960	1152.0
810	299.0	890	650.4	970	1258.0
820	335.0	900	706.1	980	1339.0
830	369.3	910	765.6	990	1455.0
840	406.6	920	838.5	1000	1563.0
850	450.6	930	906.6	1010	1673.0
860	494.9	940	979.9	1020	1821.0
870	543.7	950	1069.0		

Table 2.9. *The total charge accumulated in a.u for the region of 800-1020V and the pulse width of 1150ns.*

ii. 2nd measurement region

Pulse Width: 550ns

PSPMT's High Voltage Width: 1000-1170V

H.V(V)	Q(a.u)	H.V(V)	Q(a.u)	H.V(V)	Q(a.u)
1000	526,0	1060	828,5	1120	1271,0
1010	570,3	1070	897,8	1130	1353,0
1020	618,2	1080	957,1	1140	1448,0
1030	664,6	1090	1026,0	1150	1541,0
1040	716,5	1100	1096,0	1160	1641,0
1050	778,6	1110	1177,0	1170	1739,0

Table 2.10. *The total charge accumulated in a.u for the region of 1000-1170V and the pulse width of 550ns.*

iii. 3rd measurement region

Pulse Width: 350ns

PSPMT's High Voltage Width: 1150-1300V

H.V (V)	Q(a.u)	H.V (V)	Q(a.u)	H.V (V)	Q(a.u)
1150	694.5	1210	1024.0	1270	1472.0
1160	747.4	1220	1096.0	1280	1554.0
1170	797.3	1230	1172.0	1290	1642.0
1180	848.5	1240	1240.0	1300	1745.0
1190	904.4	1250	1311.0		
1200	963.6	1260	1384.0		

Table 2.11. *The total charge accumulated in a.u for the region of 1150-1300V and the pulse width of 350ns.*

Our first goal was to extract the relationship between the total charge accumulated and the PSPMT's high voltage free of the pulse width dependence. For this purpose, we have created a universal Total Charge (Q) – High Voltage (H.V.) diagram by measuring the total charge accumulated for three different H.V. values with respect to various pulse widths in order to find out how the values of the total charge in the three measurements regions are connected. This normalization of the charge was done to the 2nd measurements region, as follows.

Total Charge For The 1st Region: $Q_{norm1}=Q_1 \times <\frac{Q_{550}}{Q_{1150}}>$

where $<\frac{Q_{550}}{Q_{1150}}>=0.339$, is the mean ratio of the charges in the 1st and the 2nd measurements regions for the 1000-1010-1020V and Q_1 are the first measurements of the total charge in this region.

Total Charge For The 3rd Region: $Q_{norm3}=Q_3 \times <\frac{Q_{550}}{Q_{350}}>$,

where $<\frac{Q_{550}}{Q_{350}}>=2.199$, is the mean ratio of the charges in the 2nd and the 3rd measurements regions for the 1000-1010-1020V and Q_3 are the first measurements of the total charge in this region.

Finally, we normalized the total charge accumulated at its value at 1000V of high voltage (Q_{amp}).
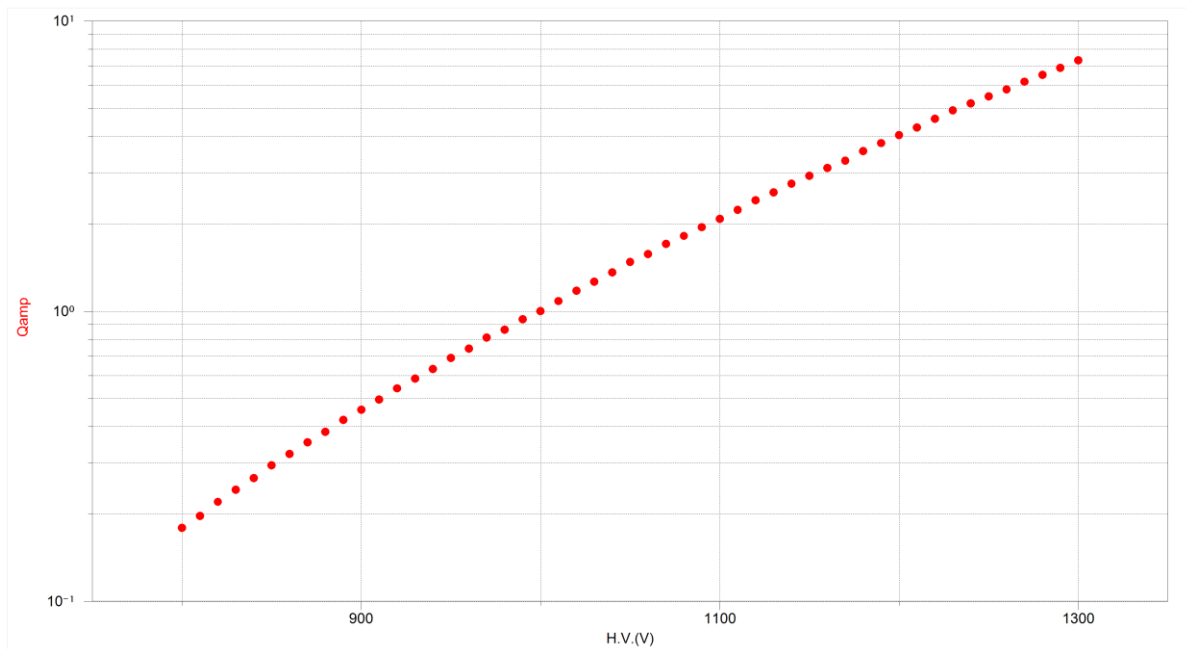
Figure 2.14. *The relationship between the normalized total charge accumulated Q_{amp} and the PSPMT's high voltage H.V. (V)*

As the *Figure 2.14* shows, the relationship between the total charge accumulated and the PSPMT's high voltage seems to be exponential and more specifically:

$$Q=A\times exp[-C(H.V.)]+B \qquad\qquad (2.2)$$

where A=0.00394±0.00025, B=-0.292±0.020, C=-0.00583±5×10^{-5} .

31

Moreover, in order to verify the relationship between the gain in charge and the supply high voltage that the manual of the HAMAMATSU R2486 PSPMT gives, which is an exponential function as *Figure 2.13* shows, we took as a reference point the gain at 1000V which is 110000. What we are calling gain, is the amplification of the charge firstly collected at the PSPMT's cathode (Qo). So, if Q is the accumulated final charge that the PSPMT's anode collects, the gain is the $\frac{Q}{Q_o}$ ratio.

If it is known that at 1000V supply voltage, the gain value is 110000, then the gain value for each supply voltage step is given by the function:

$$\text{Gain}=Q_{amp}\times110000 \qquad (2.3)$$

Q(a.u)	Q_{amp}	Gain	Q(a.u)	Q_{amp}	Gain	Q(a.u)	Q_{amp}	Gain
91.6	0.179	19720.9	426.5	0.810	89112.3	1448.0	2.748	302333.1
101.4	0.197	21676.0	453.9	0.863	94920.9	1541.0	2.923	321528.8
113.6	0.220	24226.1	493.2	0.937	103067.1	1641.0	3.113	342393.8
125.2	0.242	26648.7	526.0	1.000	110000.0	1739.0	3.299	362841.4
137.8	0.266	29248.4	570.3	1.083	119138.8	1865.4	3.559	391465.5
152.8	0.294	32393.5	618.2	1.175	129258.3	1988.3	3.792	417108.2
167.8	0.322	35418.2	664.6	1.262	138856.2	2118.5	4.042	444595.6
184.3	0.353	38846.7	716.5	1.359	149497.3	2251.3	4.293	472267.6
202.1	0.384	42225.6	778.6	1.478	162558.8	2409.6	4.595	505473.9
220.5	0.422	46426.2	828.5	1.572	172970.4	2576.6	4.914	540525.0
239.4	0.457	50301.0	897.8	1.704	187409.0	2726.1	5.199	571886.5
259.5	0.496	54508.7	957.1	1.816	199740.1	2882.2	5.497	604631.6
284.3	0.542	59587.7	1026.0	1.946	214074.4	3042.7	5.803	638299.1
307.3	0.585	64376.2	1096.0	2.079	228679.8	3236.2	6.172	678884.6
332.2	0.632	69511.9	1177.0	2.233	245580.4	3416.5	6.515	716702.9
362.4	0.689	75795.0	1271.0	2.411	265193.5	3609.9	6.884	757288.4
390.5	0.742	81674.5	1353.0	2.566	282302.7	3836.4	7.312	804330.7

Table 2.12. *The total charge accumulated in a.u (Q), the value of normalized charge (Q_{amp}) and the corresponding values of Gain for the region of 800-1300V.*

Then, from our experimental measurements we extract the graph Gain-High Voltage that totally confirms our expectations. So, the overall Gain of a photomultiplier tube is a sensitive function of the applied PSPMT's high voltage.
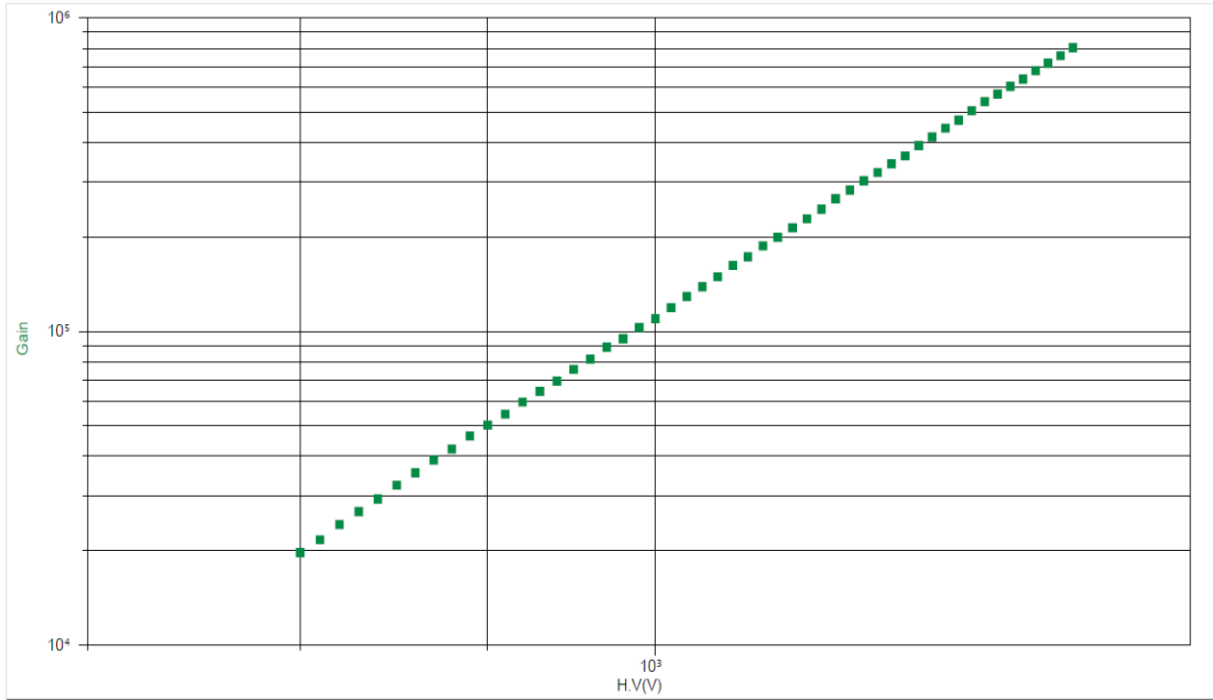
Figure 2.15. *The charge Gain as a function of the PSPMT's High Voltage (H.V.)*

What is also clear, is that the overall gain that the use of a photomultiplier tube brings depends on the number of its stages N (N+1 dynodes) and of course on the multiplication factor from dynode to dynode δ, which is given by

$$\delta = \frac{number\ of\ secondary\ electrons\ emitted}{primary\ incident\ electron} \qquad (2.4)$$

and more specifically what it is true is that: *overall Gain ~ δ^N* **[KNO00]**. So, from the calculated gain of our system we can find out the value of δ for each applied high voltage from dynode to dynode:

$$\delta = \sqrt[N]{overall\ gain} \qquad (2.5)$$

If the multiplication factor from dynode to dynode δ is a linear function of interdynode voltage, *Figure 2.16* (for our system the inter-dynode voltage since we have a 12-stage PM is the applied PSPMT's high voltage over the number of the stages , $\frac{H.V.}{12}$), then the overall gain of a 12-stage tube would vary as V^{12}. However, in fact δ for conventional dynodes varies as some fractional power of inter-dynode voltage so that the overall gain is more typically proportional to V^{Neff}, where N$_{eff}$ < N.

H.V.(V)	$H.V./_{12}$(V)	δ	H.V.(V)	$H.V./_{12}$(V)	δ
800	66,67	2,280	1060	88,33	2,732
810	67,50	2,298	1070	89,17	2,750
820	68,33	2,319	1080	90,00	2,765
830	69,17	2,338	1090	90,83	2,781
840	70,00	2,356	1100	91,67	2,796
850	70,83	2,376	1110	92,50	2,813
860	71,67	2,394	1120	93,33	2,831
870	72,50	2,412	1130	94,17	2,846
880	73,33	2,429	1140	95,00	2,862
890	74,17	2,448	1150	95,83	2,877
900	75,00	2,465	1160	96,67	2,892
910	75,83	2,481	1170	97,50	2,906
920	76,67	2,500	1180	98,33	2,925
930	77,50	2,516	1190	99,17	2,940
940	78,33	2,532	1200	100,00	2,956
960	80,00	2,566	1210	100,83	2,971
970	80,83	2,585	1220	101,67	2,988
980	81,67	2,599	1230	102,50	3,004
990	82,50	2,617	1240	103,33	3,018
1000	83,33	2,631	1250	104,17	3,032
1010	84,17	2,649	1260	105,00	3,046
1020	85,00	2,667	1270	105,83	3,062
1030	85,83	2,683	1280	106,67	3,076
1040	86,67	2,699	1290	107,50	3,090
1050	87,50	2,718	1300	108,33	3,105

Table 2.13. *The applied high voltage from dynode to dynode (H.V./12) and the corresponding multiplier factor δ.*
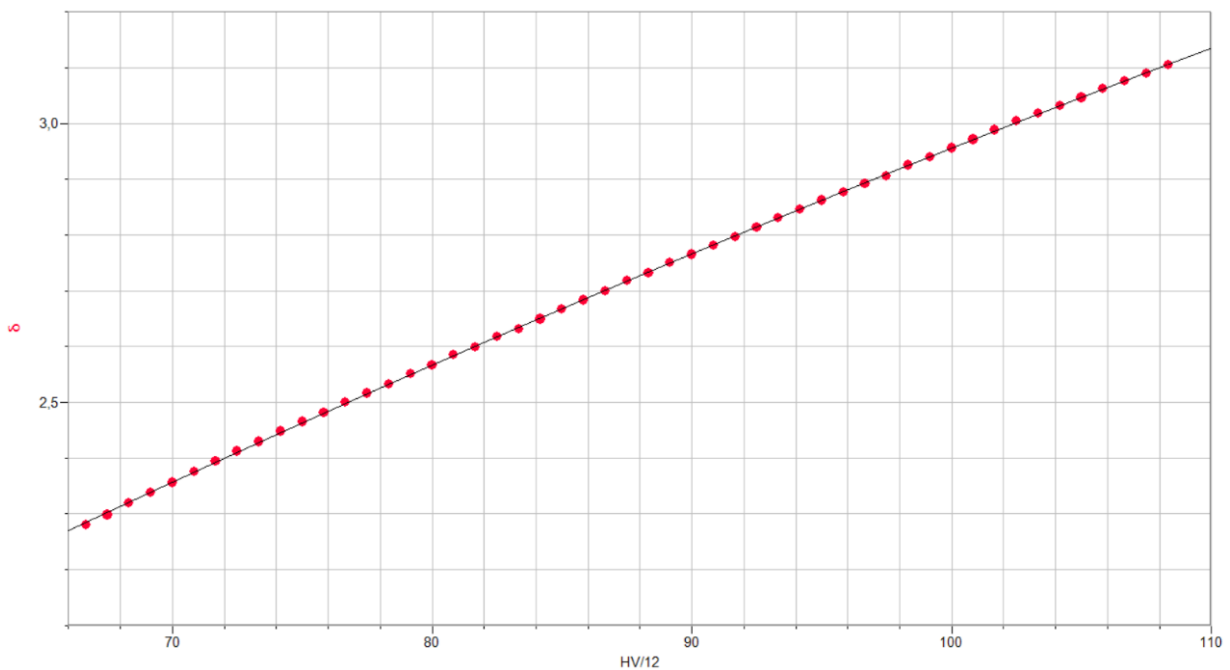
Figure 2.16. *The multiplication factor δ as a function of the applied high voltage from dynode to dynode (H.V./12).*

From our experimental data, as *Figure 2.17* shows, the relationship between LN(Gain) and LN($\frac{H.V.}{12}$) is linear and the graph's slope give the value of N_{eff}. For our PSPMT the $N_{effective}$ is about 7.6 and this is the number of the effective stages of the system that finally achieve the electron gain.
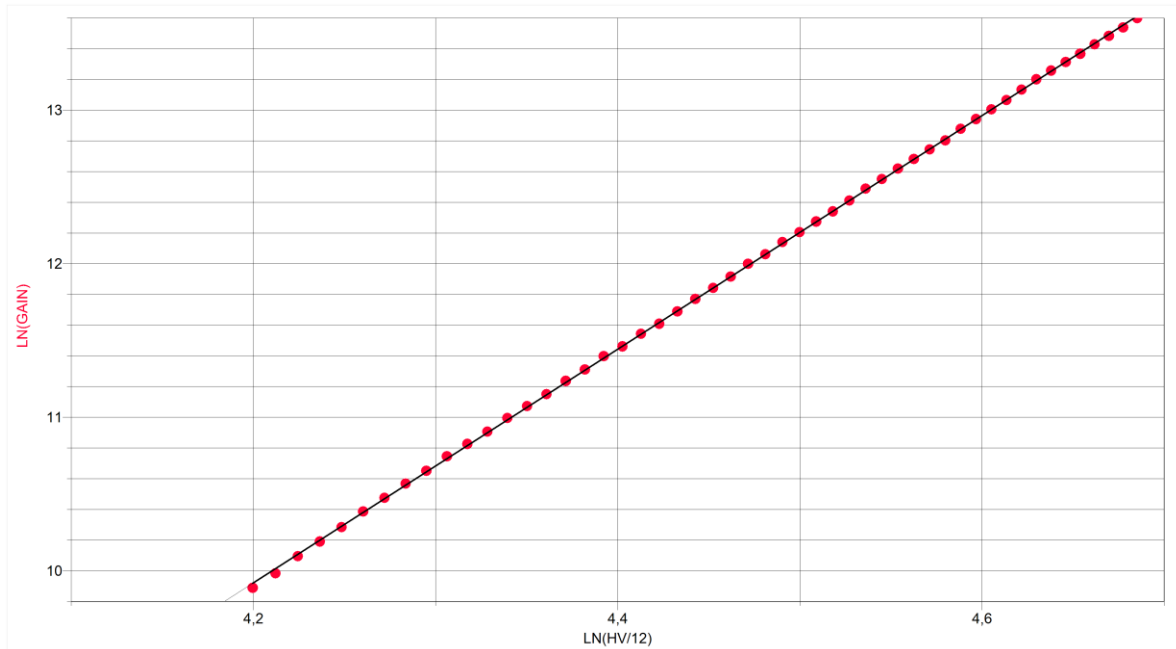
Figure 2.17. The dependence of the electron gain on the applied high voltage from dynode to dynode. The gradient of this straight line gives the number of the effective stages (N_{eff}) that finally lead to the amplification of the firstly incident electrons.

Chapter III

γ-Camera System Characterization And Optimization

3.1 Introduction

In nuclear medicine a number of small field, high-resolution γ-Camera systems based on PSPMT have been recently developed. Their advantages over commercial γ-Camera systems (better spatial resolution, lower cost, light weight) justify their demand for imaging of small human body

organs or small animals. However, the existence of spatial distortions and non-uniformities are very common problems in images from small field γ-Camera systems **[THA08]**.

A small field, high resolution γ-Camera system dedicated to radiopharmaceutical research and other clinical SPECT (Single Photon Emission Computed Tomography) applications is currently being developed in our SPECT-LAB. First of all the main body of the system is 3" cylindrical HAMAMATSU R2486 Position Sensitive PhotoMultiplier Tube (PSPMT) with a 16X+16Y-crossed wire anode in two orthogonal groups that are per two connected in order to finally have 8X and 8Y signals (*Figure 3.1*).
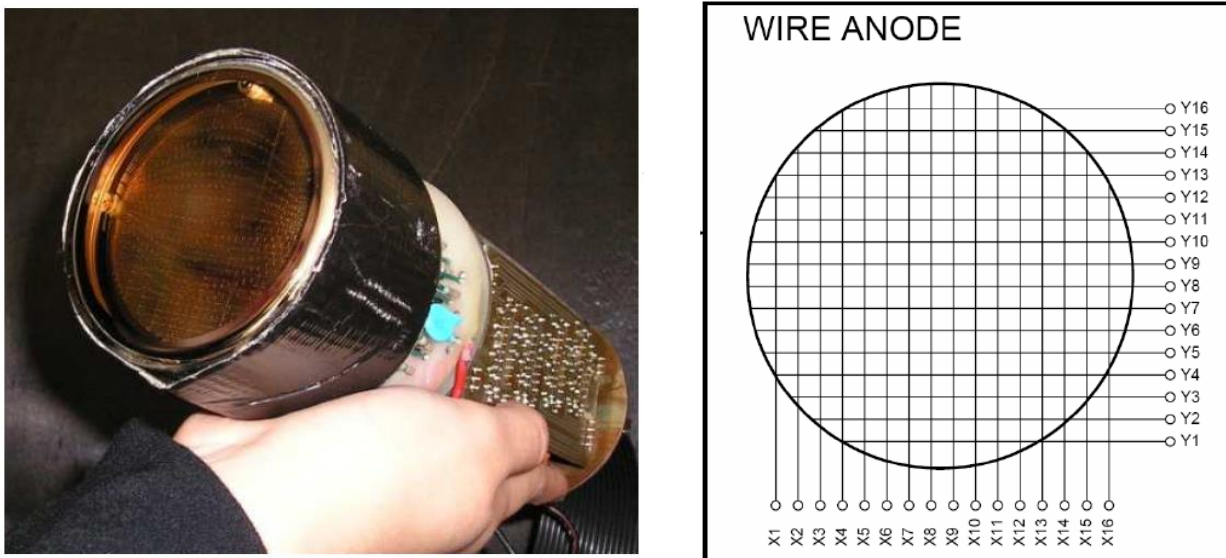
Figure 3.1. *The small field γ-Camera System with the Position Sensitive Photomultiplier Tube (PSPMT) and a schematic diagram of its multi-wire anode grid.*

As *Figure 3*.2 illustrates, our PSPMT is connected with a power supplier (H.V.) that provides a high voltage in the system (nominal values between the range of 1200 to 1320V) which is equalized between the dynodes. Moreover, the final dynode stage is connected with a Fast Amplifier from which the signals is extracted and is led to a Discriminator which adjusts the threshold and the width of the time signal in order to avoid the overflows of the Gate signal.

Finally the desirable signals end up after a small delay to two separated LeCroy 2249W Analog to Digital Converter (ADC) with 11 bits resolution and eight available signals receptors each.
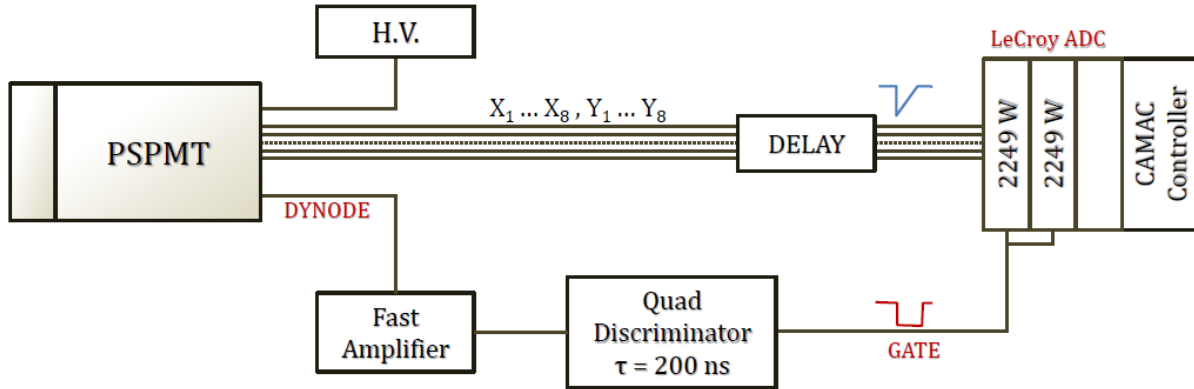
Figure 3.2 *A schematic representation of the electronics used in the PSPMT data acquisition system for signal digitization.*

Two of the main components of our γ-Camera system is a 26.8 mm thick parallel-hexagonal-hole collimator from lead and a 4 mm thick pixelated CsI(Tl) scintillator crystal (Figure 3.3). Each lead sheet of the collimator is characterized by a thickness, which is septum between the holes, and is equal to 250μm. The diameter of the holes formed is 1.5mm, while their length, which practically defines the thickness of the guide, equals 26.8mm. The these characteristics are presented in Table 3.1.

Total Area	$59.5 \times 60.4 mm^2$
Thickness	26.8 mm
Radius R of Circumscribed Circle	0.75 mm
Septum (Pb)	0.25 mm
Total Number of Holes along X (Nx)	32
Total Number of Holes along Y (Ny)	23

Table 3.1. *Geometric characteristics of the parallel hexagonal holes of the collimator.*

The γ-rays pass through the collimator holes without being absorbed and they fall into the scintillation crystal of the system. This is a pixelated crystal of Cesium Iodine doped with Thallium as an activator, in a cylindrical shape of thickness 4mm and radius 29.5mm, as shown in *Figure 3.3*. Its geometric features ensure optimum performance in the radiation detection of ^{99m}Tc. Its properties are presented in *Table 3.2*.

Properties of the CsI(Tl) Scintillation Crystal		
Density	4.51	g/cm^3
Atomic Number (Z)	54	
Decay Time	1	μs
Brightness	54	Photons/keV
Wavelength at Max	550	nm
Refraction Index	1.80	
Energy Resolution (at 662keV)	4.3%	

***Table 3.2** The properties of a Cs(I) scintillation crystal.*
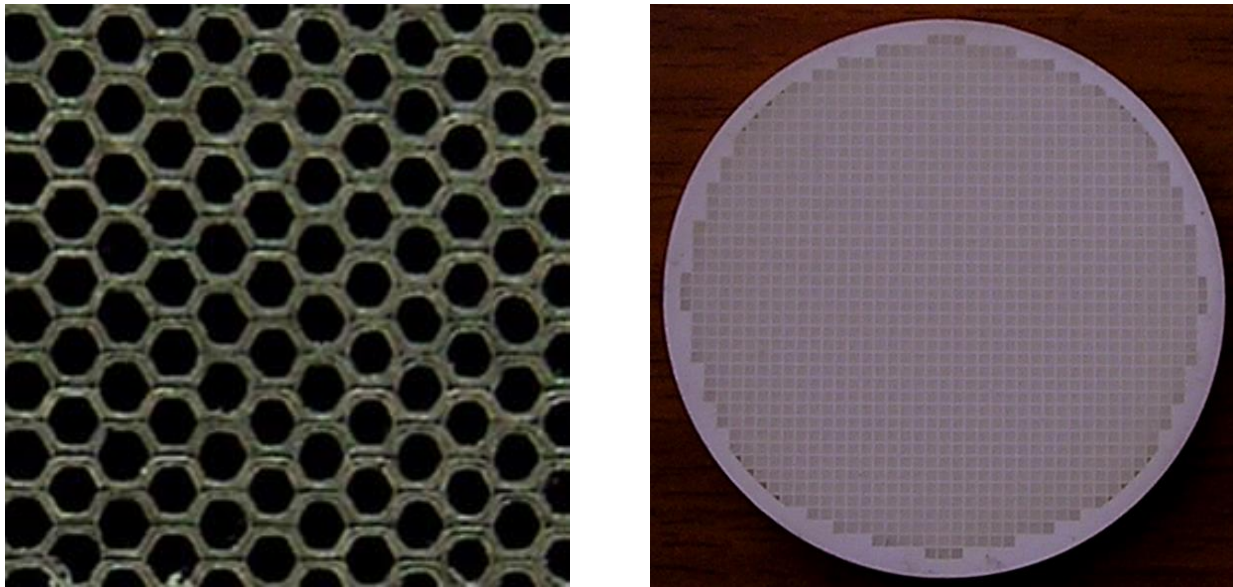
***Figure 3.3.** The parallel-hole lead (Pb) collimator (left) and the pixelated CsI(Tl) scintillation crystal.*

3.2 γ-Camera System Characterization and Optimization

The characterization and the optimization of the whole γ-Camera system was separated in two different steps where measurements with two different simple geometrical phantoms filled with water solution of ^{99m}Tc (A and B) took place.

3.2.1 1st Set of Measurements with Phantom A

In order to characterize our SPECT LAB γ-camera system we used a simple geometrical phantom, consisted of ten capillaries, 1.53mm outer diameter each. Some of them were filled with water solution of Tc^{99m} and the empty ones were used as spacers. Three planar images were recorded in vertical, horizontal and diagonal orientation of the phantom. For each recorded

image, the applied high voltage of the PSPMT was 1320V and the recorded amount of events 100000 per run.

The way that the capillaries were filled is shown in the following figure. The black holes represent the hot spots and the white ones the spacers. For reasons of simplification we will refer to the hot spots as "capillaries" and to the rest of them as "spacers".
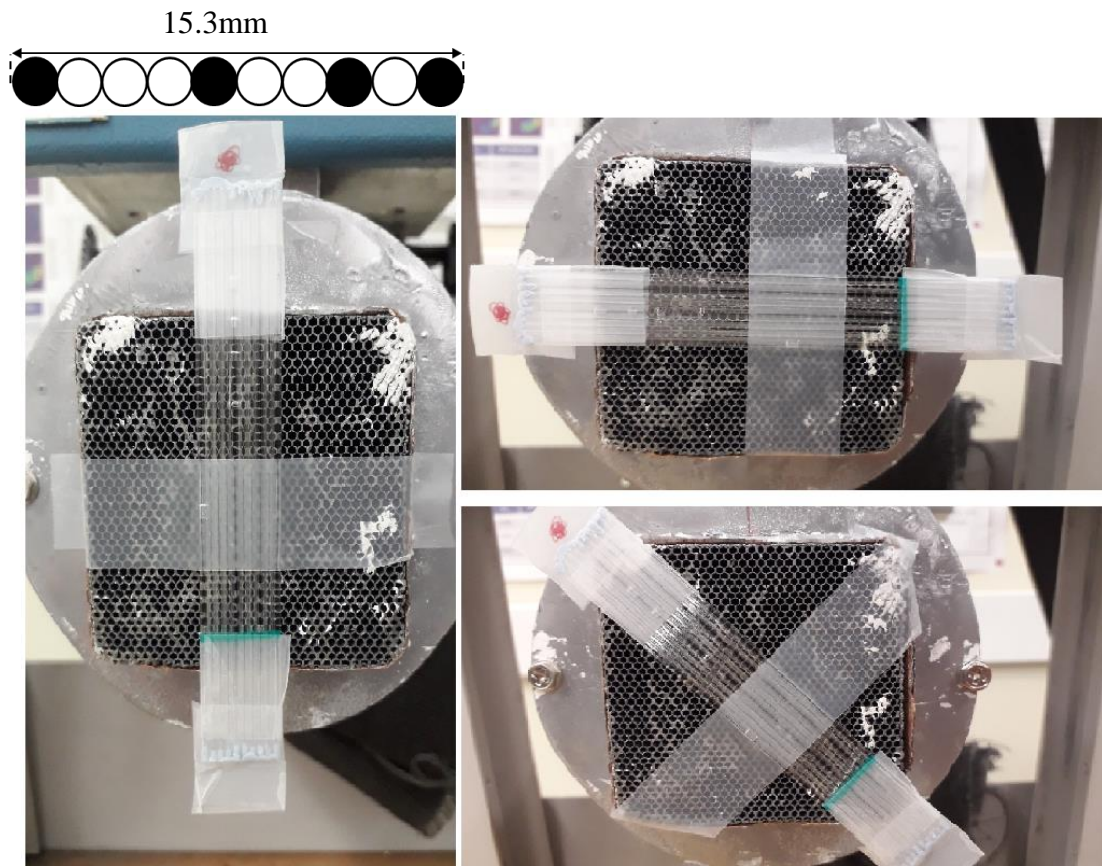
Figure 3.4. *The phantom used for the characterization of our γ-camera system in the 3 different orientations, vertical (left), horizontal (up and right) and diagonal (bottom right).*

The recorded images in all the three orientations are shown in *Figure 3.4.*
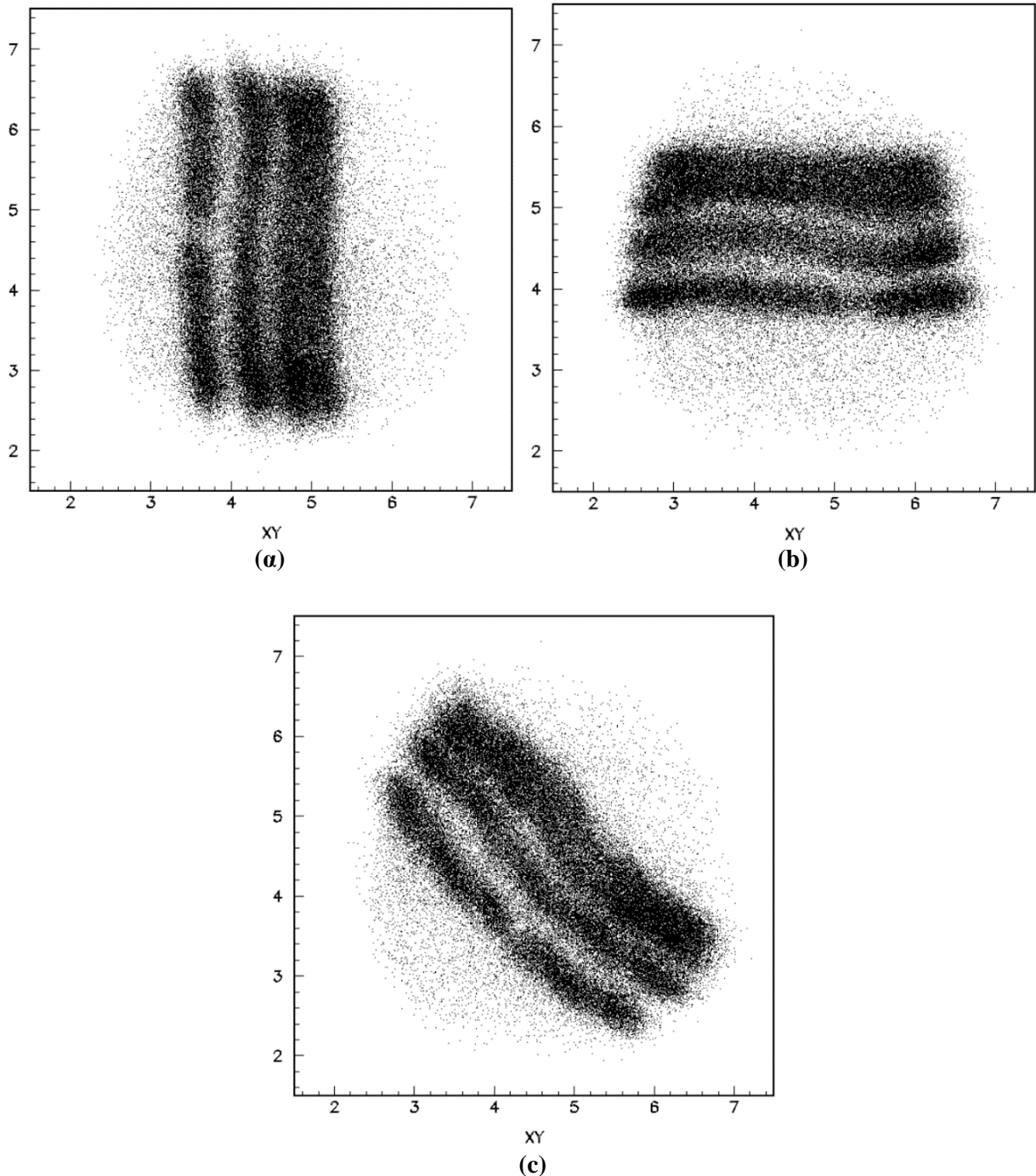
Figure 3.5. *The recorded images of the phantom for the 3 different orientations, vertical (a), horizontal (b) and diagonal (c).*

The characterization of the γ-camera system was mainly based on the evaluation of the vertically and horizontally oriented planar images. These were cut into slices of 0.5 wire-coordinates a.u (arbitrary units) thick, between the range of 6.5 to 2.5 a.u. along the y and x axis respectively. For each slice, we took the x (for the vertical orientation) and y projection (for the horizontal orientation) and by fitting 4 different gaussian curves where it was feasible, one for each hot spot, we found out the mean position of each capillary and its sigma in arbitrary units (a.u.).
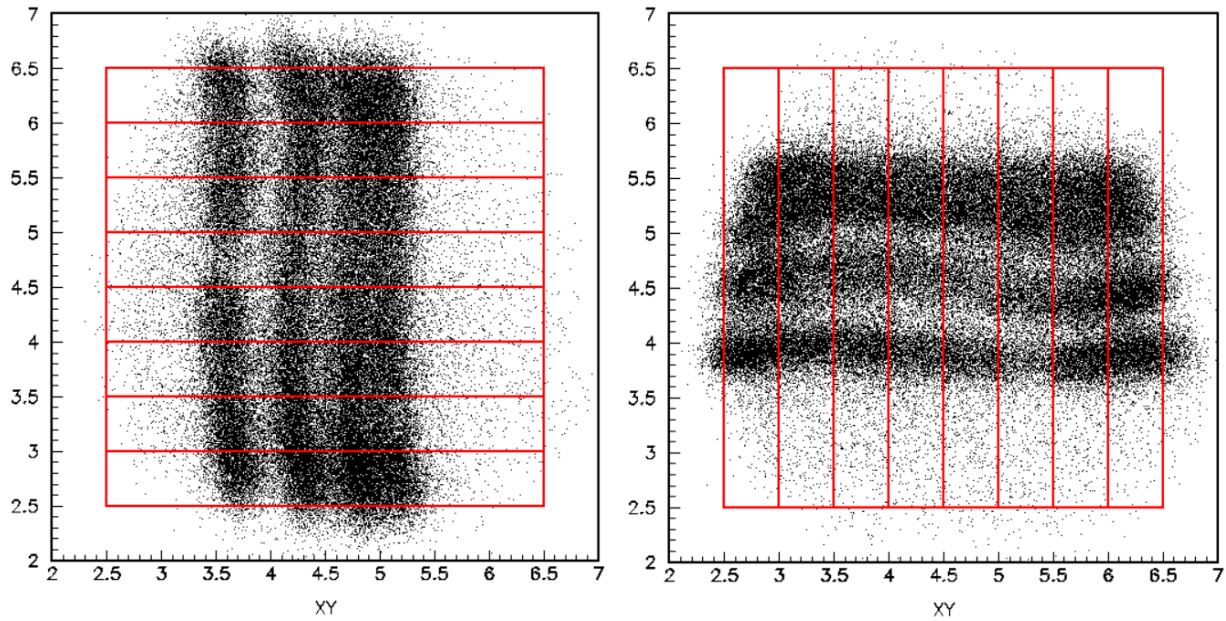
Figure 3.6. *The slices into which the vertical (left) and the horizontal (b) image of the phantom was cut in order to be analyzed. The axes are in a.u.*
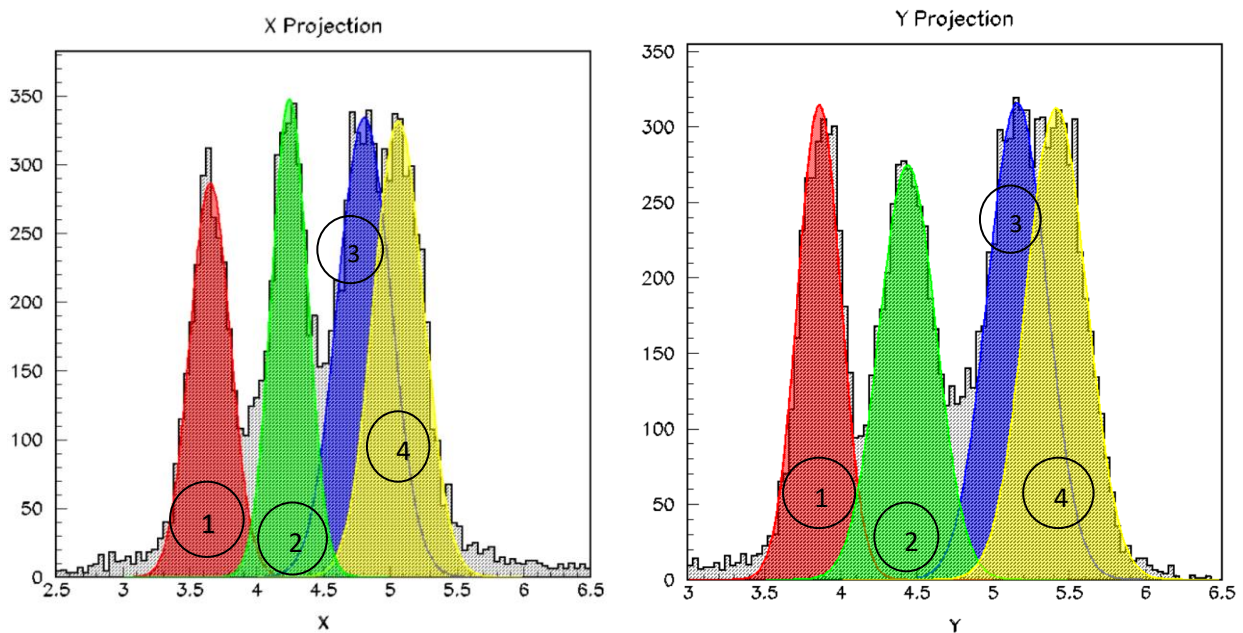
Figure 3.7. *The four different gaussians fitted on a slice of vertical (left) and horizontal (right) planar image. In both plots the horizontal axis is in a.u. and the vertical shows the amount of events.*

Although in the most slices we could distinguish 4 peaks in X or Y projection, this was not always possible, not only because of the existed spatial distortions but also of the really close distance between the 3rd and the 4th capillary that affected their distinct limits. Since we knew the real dimensions of the capillaries and considering the hot spot in the middle

41

of each one we could convert the a.u. in millimeters. Taking as a reference the mean distance between the center of the left (1st) capillary and its next one (2nd) that in fact is 6.12mm ($X_{real_2} - X_{real_1}$ or $Y_{real_2} - Y_{real_1}$, depending on the orientation of the phantom) we linked the a.u with mm and extract the mean value of sigma in each direction.

The analyzed data are summarized in the tables of the following section.

- **Vertical orientation**

X_{mean1}	σ_1	X_{mean2}	σ_2	X_{mean3}	σ_3	X_{mean4}	σ_4
3.61	0.17	4.29	0.18				
3.63	0.17	4.33	0.17				
3.62	0.17	4.28	0.18	4.75	0.14	5.08	0.15
3.58	0.17	4.21	0.17	4.70	0.17	5.08	0.16
3.58	0.17	4.20	0.16	4.72	0.14	5.07	0.14
3.61	0.16	4.21	0.15	4.70	0.16	5.07	0.17
3.66	0.15	4.24	0.17				
3.71	0.15	4.34	0.18				
<X_{mean1}>	**<σ_1>**	**<X_{mean2}>**	**<σ_2>**	**<X_{mean3}>**	**<σ_3>**	**<X_{mean4}>**	**<σ_4>**
3.62	0.16	4.25	0.17	4.72	0.15	5.07	0.15

Table 3.3. The mean X values and their sigma in a.u. for each hot capillary where their peaks in X projection of each slice were distinct. From the top, the 1st slice (6.5<y<6 a.u.) to the bottom, the final slice (3<y<2.5 a.u.)

- **Horizontal orientation**

Y_{mean1}	σ_1	Y_{mean2}	σ_2	Y_{mean3}	σ_3	Y_{mean4}	σ_4
3.90	0.15	4.47	0.17				
3.85	0.15	4.40	0.19				
3.85	0.14	4.40	0.17				
3.88	0.16	4.54	0.21	5.08	0.16	5.44	0.17
3.91	0.15	4.65	0.23	5.06	0.17	5.43	0.17
3.96	0.16	4.65	0.21	5.25	0.18	5.34	0.12
3.96	0.14	4.66	0.22	5.08	0.19	5.59	0.19
3.92	0.13	4.56	0.18				
<Y_{mean1}>	**<σ_1>**	**<Y_{mean2}>**	**<σ_2>**	**<Y_{mean3}>**	**<σ_3>**	**<Y_{mean4}>**	**<σ_4>**
3.90	0.15	4.54	0.20	5.12	0.17	5.45	0.16

Table 3.4. The mean Y values and their sigma in a.u. for each hot capillary where their peaks in Y projection of each slice were distinct. From the top, the 1st slice (6.5<x<6 a.u.) to the bottom, the final slice (3<x<2.5 a.u.)

From the values of each capillary sigma including in *Table 3.3* and *Table 3.4* respectively, we finally calculated the mean value of it in X and Y direction in mm, that gives the γ-camera system vertical and horizontal spatial response.

$$\langle \sigma_x \rangle = \frac{\langle \sigma_{x1} \rangle + \langle \sigma_{x2} \rangle + \langle \sigma_{x3} \rangle + \langle \sigma_{x4} \rangle}{4} \times \alpha_{f1} \qquad (3.1)$$

where:

$$\alpha_{f1} = \frac{X_{real_2} - X_{real_1}}{< X_{mean_2} > - < X_{mean_1} >} \qquad \text{in mm/a.u.}$$

$$\langle \sigma_y \rangle = \frac{\langle \sigma_{y1} \rangle + \langle \sigma_{y2} \rangle + \langle \sigma_{y3} \rangle + \langle \sigma_{y4} \rangle}{4} \times \alpha_{f2} \qquad (3.2)$$

where:

$$\alpha_{f2} = \frac{Y_{real_2} - Y_{real_1}}{< Y_{mean_2} > - < Y_{mean_1} >} \qquad \text{in mm/a.u.}$$

So the spatial resolution of our system is:

$$\langle \sigma_X \rangle = (1.52 \pm 0.08) \text{ mm} \qquad \langle \sigma_Y \rangle = (1.62 \pm 0.20) \text{ mm}$$

What is really important here, is that a small field γ-camera system used at preclinical level has finally a better spatial response than a clinical γ-camera since the first one can reach values up to one and a half mm, while the second one up to 3 or 4 mm. This fact means that there is always room for optimization in clinical practice.

Although a small field γ-camera has a better resolution compared to clinical systems, unbalanced amount of accumulated charge on the anodic grid of the Photomultiplier Tube combined with Center of Gravity position reconstruction algorithms, such as *Anger Algorithm* that is used in this study, produces systematically shifts towards the center of the image and as a result the effective field of view of the camera is reduced. The Anger Algorithm operates successfully in case of a centrally detected γ-rays, but it does not so when it has to do with an electron cloud positioned near the edge of the anode. This fact causes deformation effects at the edges of the image and this kind of spatial distortions is called *barreloid effect*. The position estimates are computed by combining only the PhotoMultiplier Tube's at known locations x_i , y_i

that have signals S_i that exceed a threshold S_{min}. In the simple Center of Gravity calculation, the functions w return just the raw signals Si:

$$\hat{X} = \frac{\sum_{S_i \geq S_{min}} X_i w(X_i S_i)}{\sum_{S_i \geq S_{min}} w(X_i S_i)} \quad \text{and} \quad \hat{Y} = \frac{\sum_{S_i \geq S_{min}} Y_i w(Y_i S_i)}{\sum_{S_i \geq S_{min}} w(Y_i S_i)}$$

that finally result in a non-uniform and non-isotropic spatial resolution **[PET11]**. Similar effects are also caused by the fact that individual anode wires are not uniformly amplified.

In order to eliminate this kind of spatial distortions, a 1st order linear interpolation was applied in vertical and horizontal, recorded, planar images. For this purpose, we found 18 or 20 different supporting points along the 2nd capillary, that consist a reference line in each case (vertical, horizontal and diagonal) and according to the capillary's mean position that experimentally recorded we knew the sifting of each event needed depending only on its Y or X position for the vertically (and diagonally) and horizontally oriented phantom respectively. So, for each orientation that the phantom was put, we defined the suitable function including the position of the supporting points **[THA08]**.

- **Vertical orientation**

The vertically oriented phantom helps to gain the correction for the X-coordinate.

→ The function that followed for the vertical correction of the phantom was:

$$\boxed{\Delta X_i(Y_i) = \frac{Y_i - Y_L}{Y_H - Y_L} \times (\Delta X_H - \Delta X_L) + \Delta X_L}$$

(3.3)

where,

$\Delta X_i \ (Y_i)$= the appropriate sifting of each event according to its Y_i position

$\Delta X_H, \Delta X_L =$ the sifting towards the mean position of the reference capillary of the higher and
lower supporting point of each event

$Y_H, Y_L =$ the Y position of the higher (H) and lower (L) supporting point for each event

X_{Si}	Y_{Si}	ΔX_{Si}
4.11	6.66	+0.14
4.24	6.42	+0.01
4.28	6.21	-0.03
4.31	5.99	-0.06

4.30	5.76	-0.05
4.28	5.50	-0.03
4.25	5.26	0.00
4.22	5.02	+0.03
4.21	4.74	+0.04
4.18	4.46	+0.07
4.18	4.17	+0.07
4.20	3.94	+0.05
4.20	3.68	+0.05
4.25	3.45	0.00
4.22	3.14	+0.03
4.28	2.94	-0.03
4.34	2.73	-0.09
4.32	2.56	-0.07

Table 3.5. *The coordinates (X_{Si}, Y_{Si}) of each supporting point along the 2nd capillary in a.u. and their distances (ΔX_{Si}) from the mean X position of the capillary.*

Based on the above described procedure, the corrected image for the measured vertically oriented phantom is depicted in *Figure 3.8.*

Figure 3.8. *The reference line along the 2nd capillary in the planar image before the correction (left) and how it seems after the correction (right), when the phantom has been vertically oriented. In the right image we can notice the small air bubble in the 1st capillary that caused by accident and that our system recorded. The axes are in a.u in both images.*

• Horizontal orientation

Similarly to the previous process, the horizontally oriented phantom helps to gain the correction of the Y-coordinate.

→ The function that followed for the horizontal correction of the phantom was:

$$\Delta Y_i(X_i) = \frac{X_i - X_L}{X_H - X_L} \times (\Delta Y_H - \Delta Y_L) + \Delta Y_L \qquad (3.4)$$

where

$\Delta Y_i(X_i)$ = the appropriate sifting of each event according to its X_i position

$\Delta Y_H, \Delta Y_L$ = the sifting towards the mean position of the reference capillary of the higher and lower

         supporting point of each event

X_H, X_L = the X position of the higher (H) and lower (L) supporting point for each event

X_{Si}	Y_{Si}	ΔY_{Si}
6.50	4.62	-0.08
6.34	4.50	+0.04
6.16	4.45	+0.09
5.97	4.41	+0.13
5.75	4.38	+0.16
5.52	4.38	+0.16
5.30	4.41	+0.13
5.05	4.50	+0.04
4.76	4.50	+0.04
4.44	4.58	-0.04
4.09	4.64	-0.10
3.79	4.62	-0.08
3.51	4.62	-0.08
3.19	4.61	-0.07
3.03	4.57	-0.03
2.90	4.57	-0.03
2.65	4.57	-0.03
2.51	4.56	-0.02

Table 3.6. *The coordinates (X_{Si}, Y_{Si}) of each supporting point along the 2nd capillary in a.u. and their distances (ΔY_{Si}) from the mean Y position of the capillary.*

In the following figure we can see the results.

Figure 3.9. *The reference line along the 2ⁿᵈ capillary in the planar image before the correction (left) and how it seems after the correction (right), when the phantom has been horizontally oriented. The axes are in a.u in both images.*

• Diagonal orientation

As far as the diagonally recorded planar image is concerned, the upper correction technique did not work since a 2D interpolation was needed, as it seems in *Figure 3.10.* In order to analyze the diagonal planar image we turned it about 45º and its analysis was similar to the vertical one, since we used the *(3.3)* correction function. By cutting the planar image in 8 slices as we did before, we found the $<X_{mean2}>=$ 4.24 a.u. and we took 20 supporting points along the 2ⁿᵈ capillary, for which we calculated the distance of their X position from the mean position $<X_{mean2}>$ of the capillary.

X_{Si}	Y_{Si}	ΔX_{Si}
4.32	6.65	-0.08
4.25	6.44	-0.01
4.22	6.27	+0.02
4.26	6.07	-0.02
4.28	5.88	-0.04
4.29	5.65	-0.05
4.24	5.42	0.00

4.12	5.11	+0.12
4.06	4.86	+0.18
4.04	4.63	+0.20
4.02	4.26	+0.22
4.03	3.87	+0.21
4.07	3.65	+0.17
4.08	3.29	+0.16
4.10	3.10	+0.14
4.12	2.85	+0.12
4.15	2.66	+0.09
4.20	2.43	+0.02
4.25	2.18	+0.01
4.28	2.08	-0.04

Table 3.7. *The coordinates (X_{Si}, Y_{Si}) of each supporting point along the 2nd capillary in a.u. and their distances (ΔX_{Si}) from the mean X position of the capillary.*

It is as clear as day from the *F*igure *3.10* that the previous correction technique can not optimize the image and eliminate the distortions in every case. So further study is needed. For this purpose a second set of measurements with a different phantom followed.
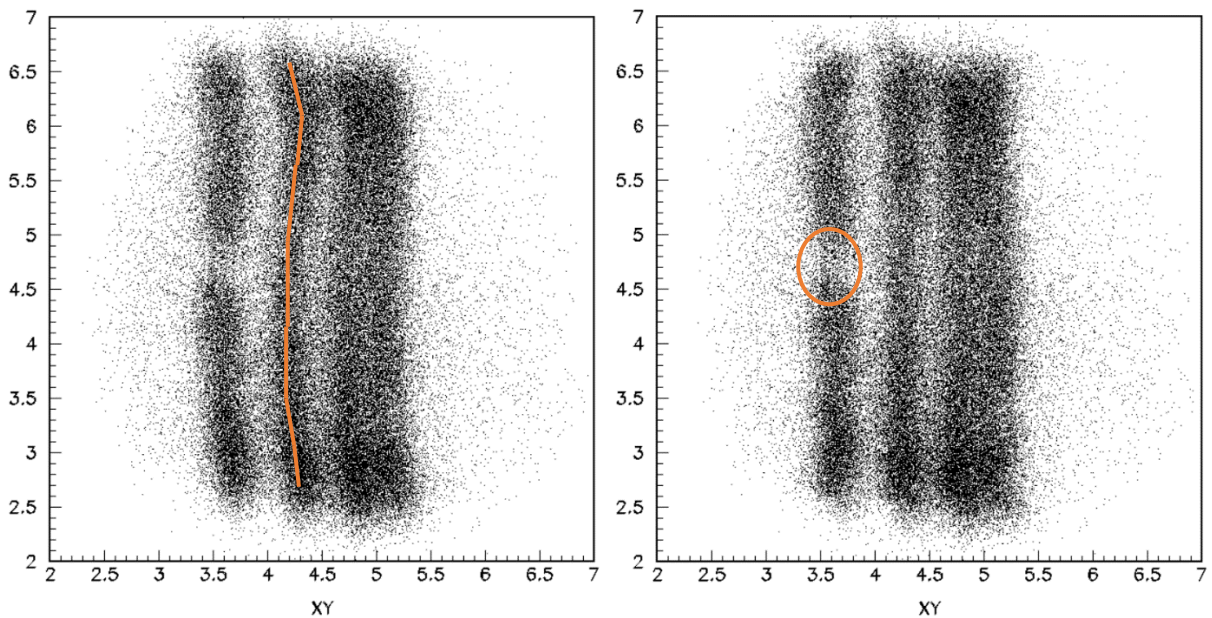

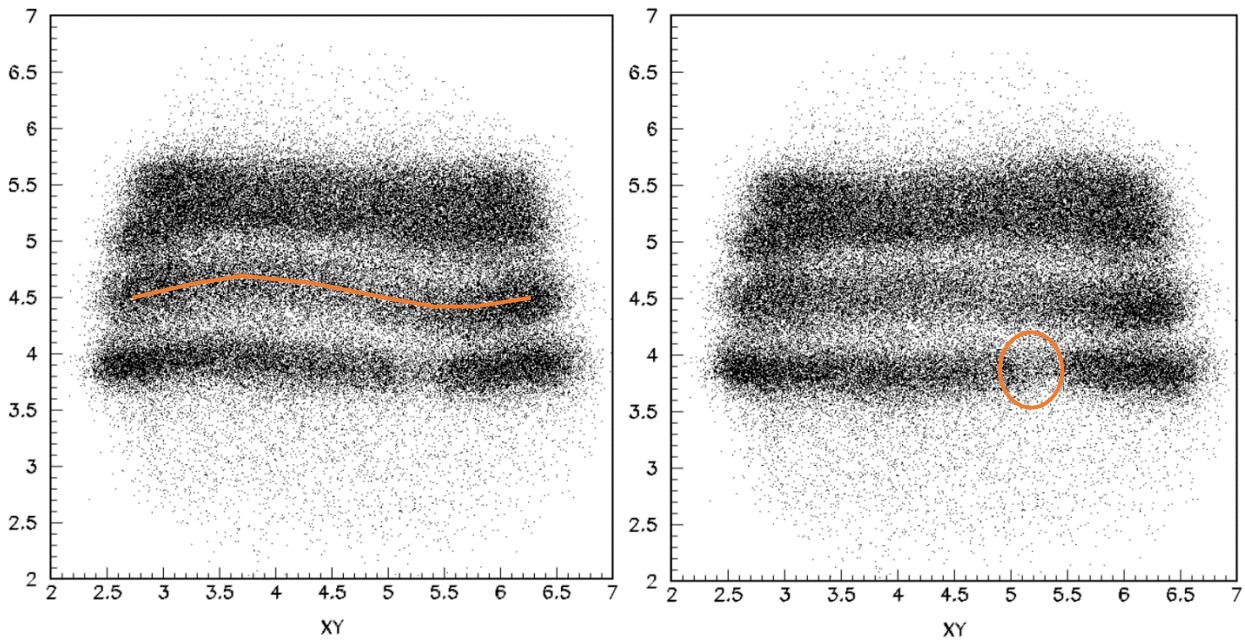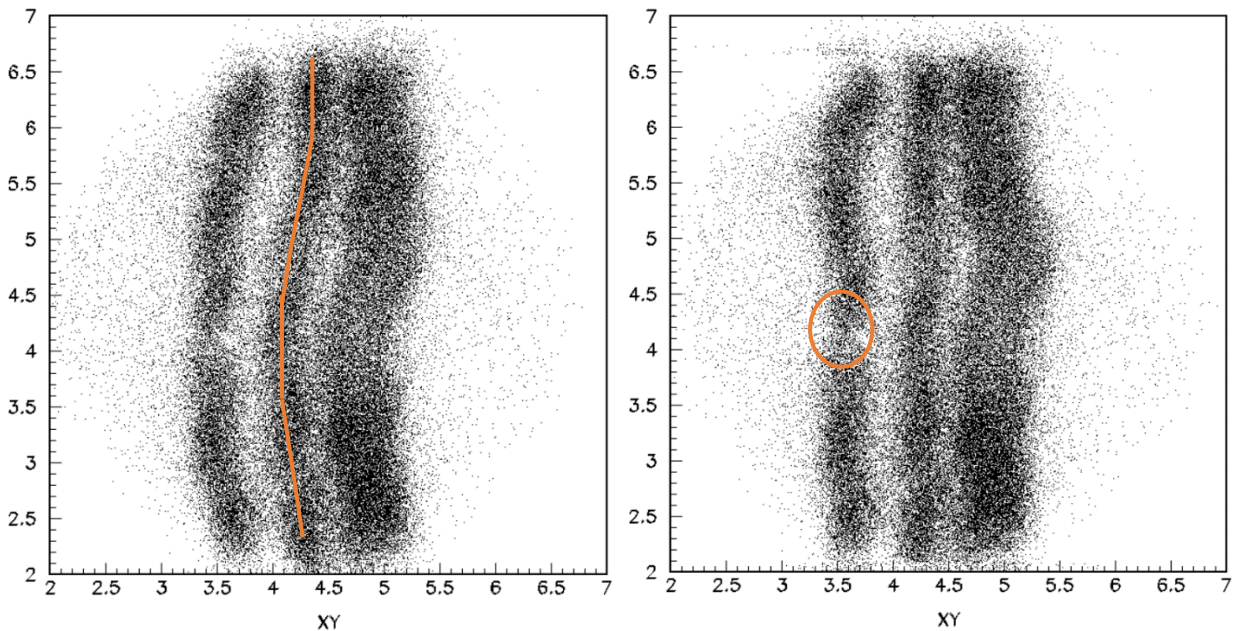**Figure 3.10.** *The reference line along the 2nd capillary in the planar image before the correction (left) and how it seems after the correction (right), when the phantom has been diagonally oriented and the planar image has been turned 45° before the analysis. As it is clear a 1st order interpolation does not eliminate the barreloid effect and a 2d correction is needed. The axes are in a.u. in both images.*

3.2.2 2nd Set of Measurements with Phantom B

Verification And Optimization of Previous Results

This set of measurements (A) was taken in order to verify the above results and to define a more accurate correction technique, in order to be used for planar images of a more complicated geometrical phantom. For this set (A), the phantom used is consisted of capillaries with two different diameters, put as it is shown in *Figure 3.10*, where each painted hole/cylinder represents a filled with Tc-99m capillary and each white an empty one used as spacer. The volume ratios of the capillaries are:

$$\frac{V_1}{V_2} = \frac{200\mu L}{75\mu L} \cong 2.67 \qquad \frac{V_1}{V_3} = \frac{200\mu L}{200\mu L} = 1.00$$

During this set of measurements we increased the statistics by recording 500000 events for only a vertical planar image. From this one, we took again slices of 0.5 a.u thick as in the analysis of the previous set, and by taking its X projection and fitting three different gaussians (one for each hot spot), we extracted by the same analysis process, the mean sigma of the capillaries. It is easy to verify the volume ratios and as a result the system response by the corresponding ratio of the recorded events where the error is about 3%, that is accepted.

$$\frac{Events_1}{Events_2} = \frac{194253}{86838} \cong 2.24 \qquad \frac{Events_1}{Events_3} = \frac{194253}{19173} = 1.01$$
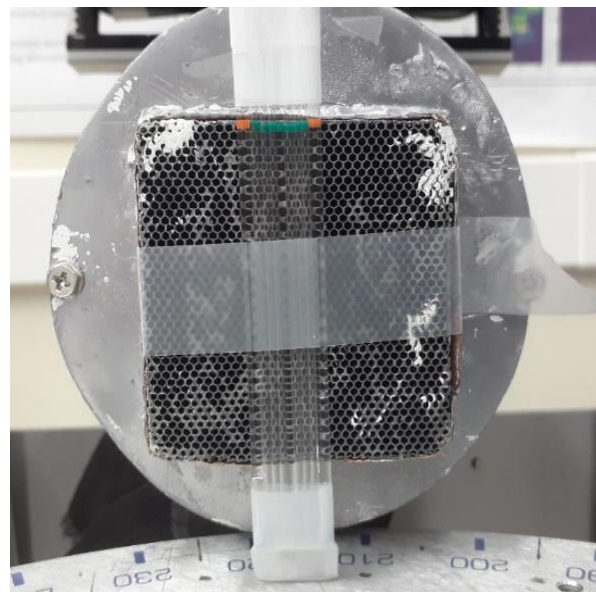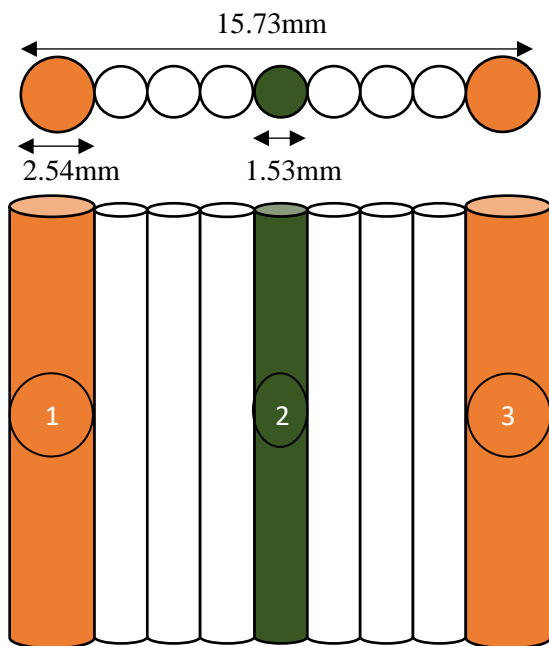
Figure 3.11. *A figure (on the left) and an image (on the right) of the phantom of the 2nd set of measurements consisted of capillaries with different diameters put in front of the γ-Camera System.*

X₁	σ₁	X₂	σ₂	X₃	σ₃
3.798	0.138	4.401	0.150	5.023	0.175
3.837	0.153	4.525	0.158	5.102	0.142
3.818	0.161	4.510	0.168	5.146	0.143
3.759	0.155	4.421	0.163	5.144	0.167
3.732	0.154	4.403	0.162	5.134	0.176
3.753	0.146	4.417	0.170	5.129	0.170
3.799	0.150	4.462	0.160	5.149	0.174
3.873	0.146	4.542	0.161	5.238	0.170
<Xmean1>	**<σ₁>**	**<Xmean2>**	**<σ₂>**	**<Xmean3>**	**<σ₃>**
3.796	0.150	4.460	0.161	5.133	0.164

***Table 3.8.** The mean X values and their sigma in a.u. for each hot capillary where their peaks in X projection of each slice. From the top. the 1ˢᵗ slice (6.5<y<6 a.u.) to the bottom. the final slice (3<y<2.5 a.u.).*

$$\langle \sigma_x \rangle = \frac{\langle \sigma_{x1} \rangle + \langle \sigma_{x2} \rangle + \langle \sigma_{x3} \rangle}{3} \times \alpha_f \qquad (3.5)$$

where:

$$\alpha_f = \frac{X_{real_3} - X_{real_1}}{< X_{mean_3} > - < X_{mean_1} >}$$

The reference distance here is this between the center of the left (1ˢᵗ) capillary and the right one (3ʳᵈ) that in fact is 13.24mm ($X_{real_3} - X_{real_1}$) and from the *(3.5)* we extract the mean value of sigma. This value represents the spatial resolution of the γ-camera system and comes to verify the corresponding value of the 1ˢᵗ set of measurements with an only 3.29% deviation.

$$<\sigma_x> = (1.57 \pm 0.07) \text{ mm}$$
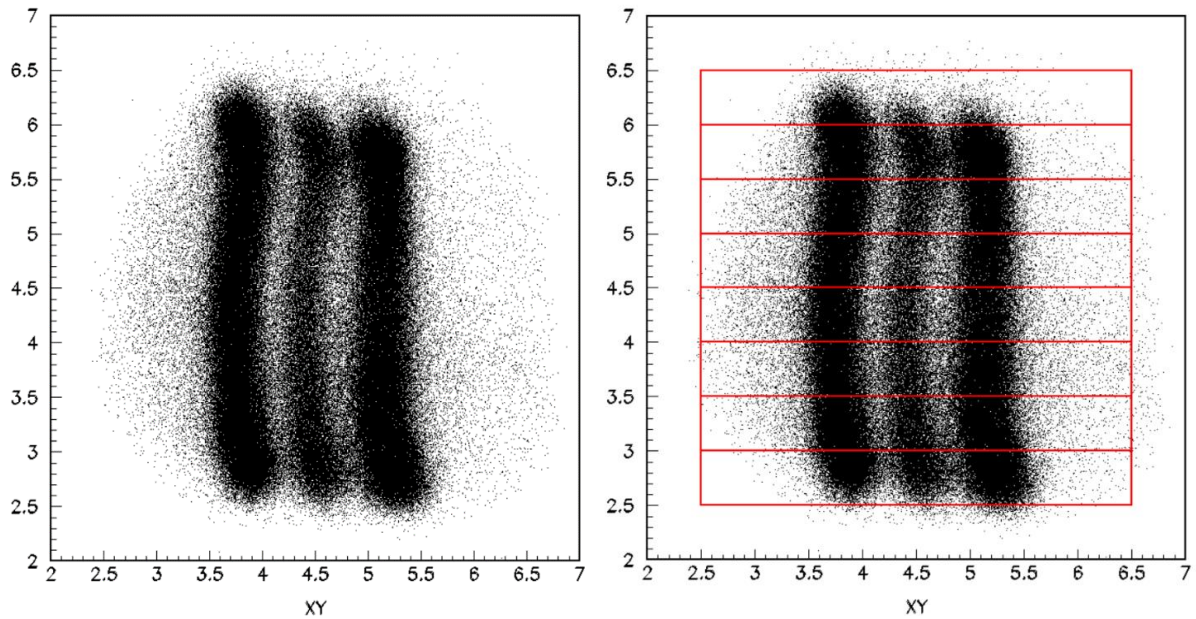
Figure 3.12. *On the left the recorded planar image of the phantom and on the right the way that the slices were defined in order to analyze our phantom and extract the spatial resolution of the γ-camera system.*
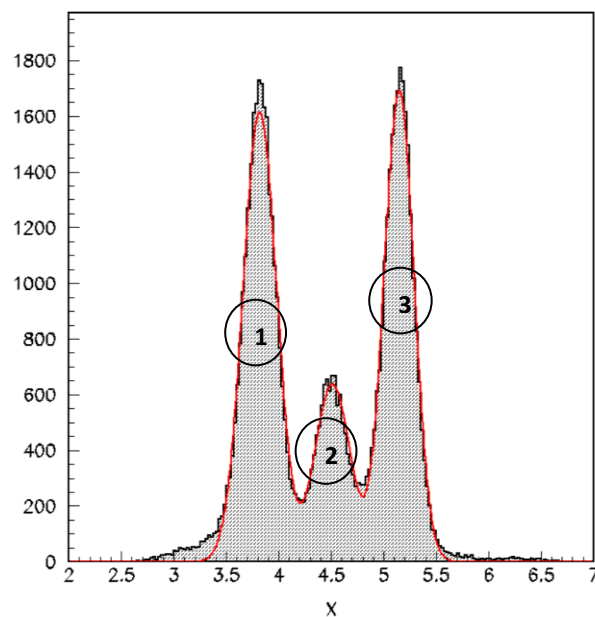
Figure 3.13. *The slice between 5.5<y<5.0 a.u and the three gaussians fitted for each capillary.*

Moreover. in order to eliminate the spatial distortion that is obvious in the planar image for all the hot capillaries (*Figure 3.12 (left)*) we took 38 supporting points along one capillary per time, that defined a spline function and according to their distance from each reference capillary we extract the appropriate shifting of each event depending on their Y position, as we did in the 1st set too (function *(3.3)*).

SET (A), row data
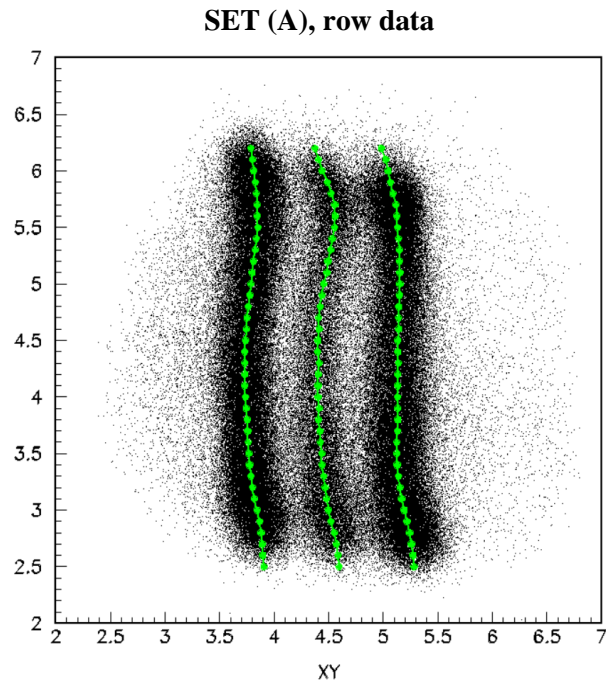
Figure 3.14. *The 38 supporting points along each capillary that define the spline function according which we corrected the planar image of the phantom. The axes are in a.u.*

The above process was followed once by taking as reference capillary the 1st and subsequently the 3rd one. The 2nd one was not taken under consideration because of lack of statistics. However the 1st seems to be more efficient (*Figure 3.15).*

SET (A), corrected on the left   **SET (A), corrected on the right**.
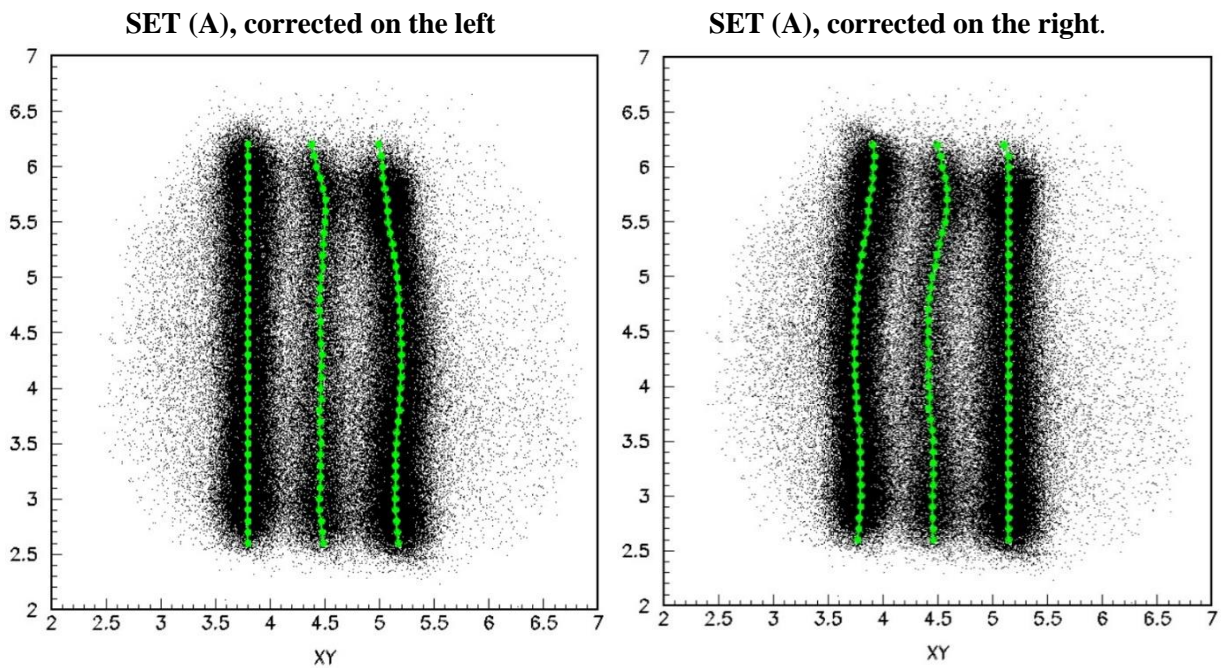
Figure 3.15. *On the left the corrected planar image taking as reference capillary the 1st and on the right the 3rd one. In both images the axes are in a.u. As it seems the 1st technique seems to be more effective. however a 2d correction maybe needed.*

Looking carefully the *Figure 3.15* it is clear that the correction technique is a function not only of the Y position of the event. but also of its X position and this because the distortions seem to be more intense as we approach the margins of the effective FOV of the system. So, a 2D correction technique is needed, in order to optimize each planar image taken

For this purpose, two more planar images were recorded (set (B) and (C)), where the phantom was shifted some mm right (B) and left (C) of the 1st image.

In this measurements set we calculated again the recorded events ratio in order to verify our statistics that should be analogue to the volumes of the capillaries. When we put the phantom right of the 1st orientation this ratio is:

$$\frac{Events_1}{Events_2} = \frac{40688}{15919} \cong 2.56 \qquad \frac{Events_1}{Events_3} = \frac{40688}{33122} \cong 1.23$$

and as it becomes clear the $\dfrac{Events_1}{Events_3}$ ratio seems to deviate enough from the 1 since the 3rd capillary is at the margins of the FOV of the γ-camera and as result a lack of recorded events is noticed. The same ratios when the phantom is left of the 1st orientation is:

$$\frac{Events_1}{Events_2} = \frac{74895}{31615} \cong 2.37 \qquad \frac{Events_1}{Events_3} = \frac{74895}{74963} \cong 1.00$$

SET (B)   **SET (C)**
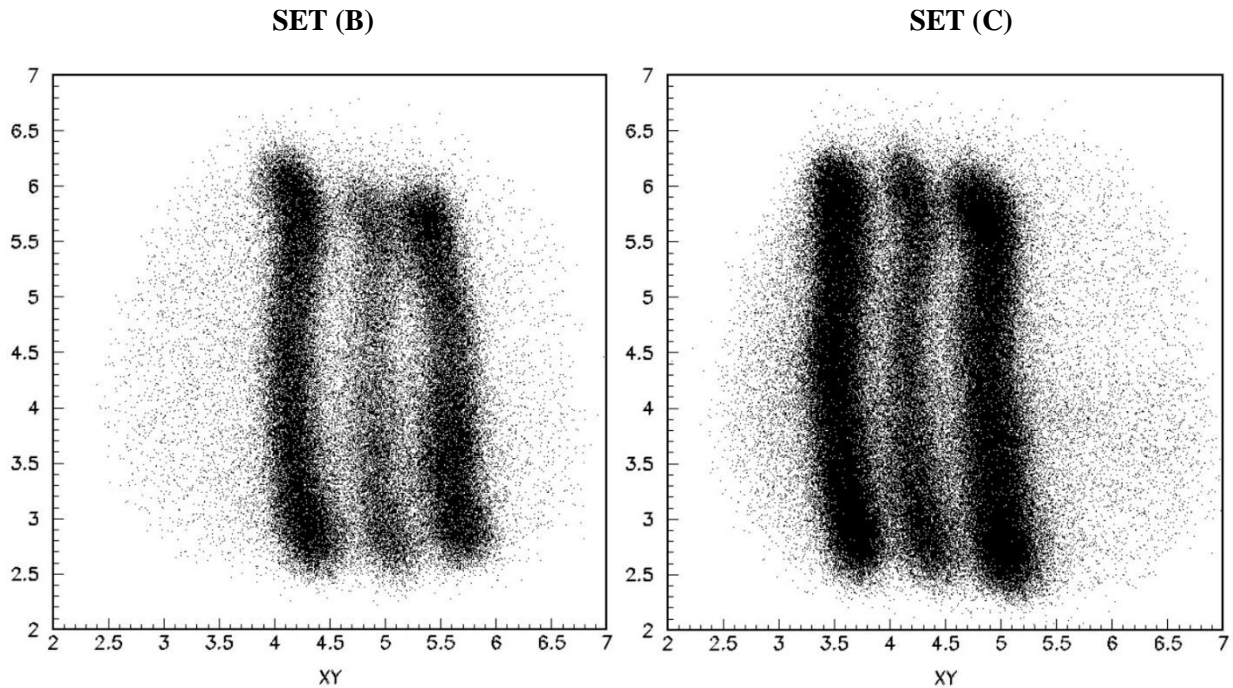
Figure 3.16. *On the left the recorded image where the phantom has been shifted right (B) of the 1st set image (100000 events) and on the right the corresponding recorded one, where the phantom has been shifted left (C) of the 1st one (200000 events).*

Now we took 38 supporting points along each capillary for all the recorded planar images, that create 9 different supporting lines. In this way, we succeed in separating the whole space in 8 different X and 39 Y levels. Although we have 9 different supporting lines due to the phantom position, two of them are in the same mean X position (*Figure 3.17)* and for analysis purposes we keep these that refer to measurements with higher statistics.
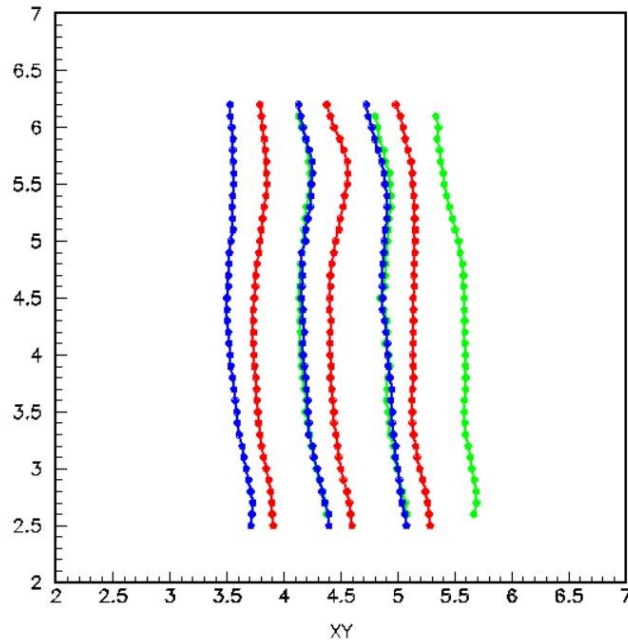
Figure 3.17. *In this figure we see the supporting points and lines along each capillary for the three different positions of the phantom. The red lines refer to the 1ˢᵗ recorded planar image and the blue and green to the left and right shifted respectively.*

The reference Y positions according to which we took the supporting points are between 2.50 and 6.20 a.u. with a step of 0.10 a.u. For each capillary we extract its mean X position by fitting the appropriate gaussian function on its X projection that give the nominal positions of the capillaries and we finally have seven different X levels.

Supportings Nominal Posistions

Nominal Positions (a.u)	3.568	3.796	4.215	4.471	4.922	5.147	5.554

Table 3.9. *The nominal X positions in a.u. of the seven reference lines on which the correction of the planar image is based.*

1ˢᵗ Step : 2D-Correction Technique With 1 Nominal X-Support

For each random event $(X_i.Y_i)$ we found two different Y levels Y_H and Y_L that are defined from the supporting points that we have already found. From its distance from the lower level and the shifting that each supporting point needs we calculate the weighted by Y shiftings needed DX_{ij} where j takes values from 1 to 7 taking in mind the closest neighbours per time (*Figure 3.18*).

More specifically:

$$AA_i = \frac{Y_i - Y_L}{Y_H - Y_L} \qquad (3.6)$$

$$DX_{ij} = AA \times \left(DX_{Hj} - DX_{Lj}\right) + DX_{Lj} \qquad (3.7)$$

where,

j is either j=1 or j=2 for the following example (*Figure 3.17*) and represents the closest pair (high and low) of supporting points.
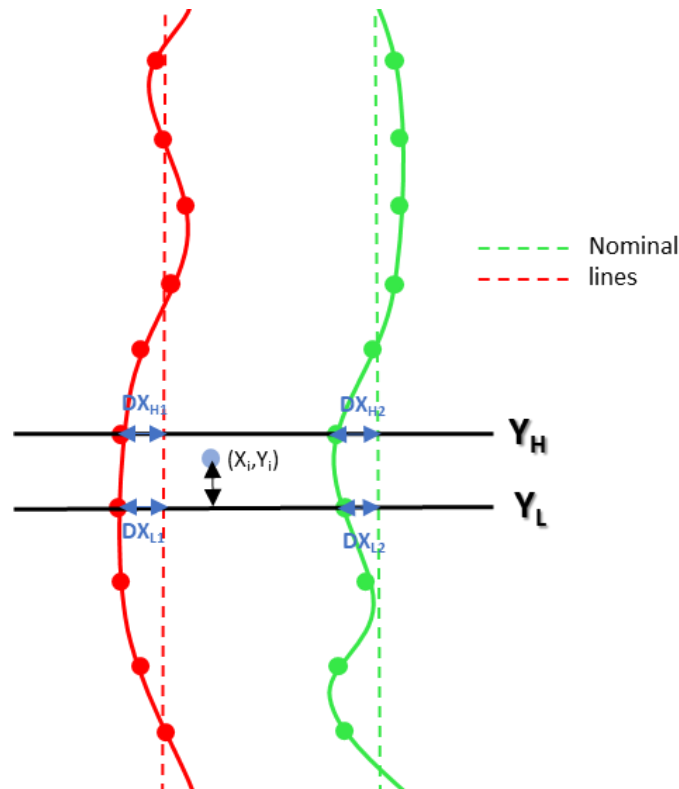
Figure 3.18. This figure is a schematic representation of the first step of the correction technique. For a random event $(X_i.Y_i)$ we take under consideration the distances from the nominal position of the closest neighbours (DX_H and DX_L) and their Y coordinates. $Y_H.Y_L$ for the above and the below supporting point respectively.

2nd Step : Extension of the 2D-Correction Technique With Many Supporting Lines

 In this step we weighted the sifting that each random event needs according to its distances D_k from the closest nominal lines and positions too (*Figure 3.19*). For this reason we have to find these distances and the final correction function is:

$$D_k = \left| X_i - X_{nominal_k} \right| \tag{3.8}$$

$$DX_{total_i} = \frac{D_{k+1} \times DX_{i_j} + D_k \times DX_{i_{j+1}}}{D_{k+1} + D_k} \tag{3.9}$$

This technique can be applied for any case, where $\mathbf{X_k} < \mathbf{X_i} < \mathbf{X_{k+1}}$, with $\mathbf{X_k}$ and $\mathbf{X_{k+1}}$ are the nominal supporting positions. However, there are events recorded outer of the bound area defined by the supporting lines in both X and Y directions, so we balance their corrections with the closest supporting line of the given coordinates for the specified event.
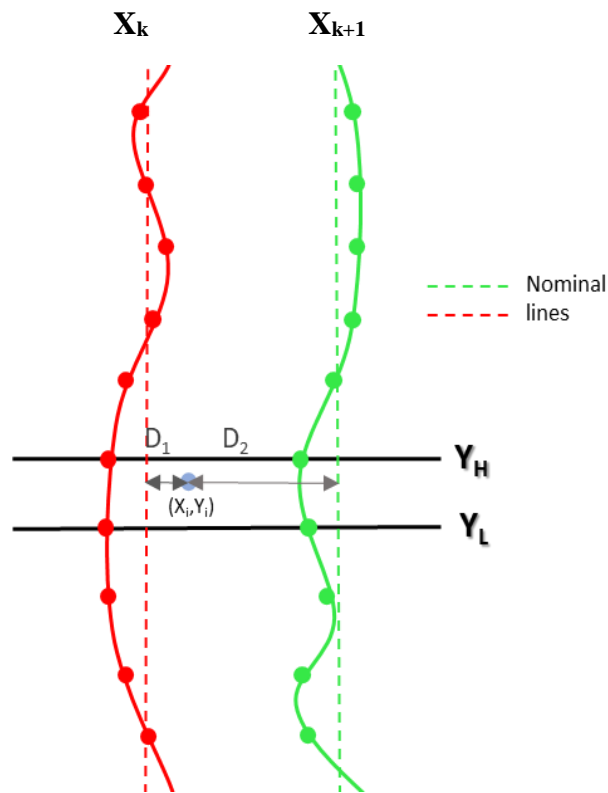
Figure 3.19. *The distances D_k and D_{k+1} from the nominal positions are the factors that finally balance the correction that each event needs.*

Finally the new position of the event is:

$$X'_i = X_i + DX_{total_i} \qquad (3.10)$$

What is more it works event by event and seems to be efficient enough as it optimizes every planar image taken in this measurement set (*Figure 3.19)* and offers to us a tool that can be used in planar images of more complex geometrical phantoms too.

(a)

(b)

(c)
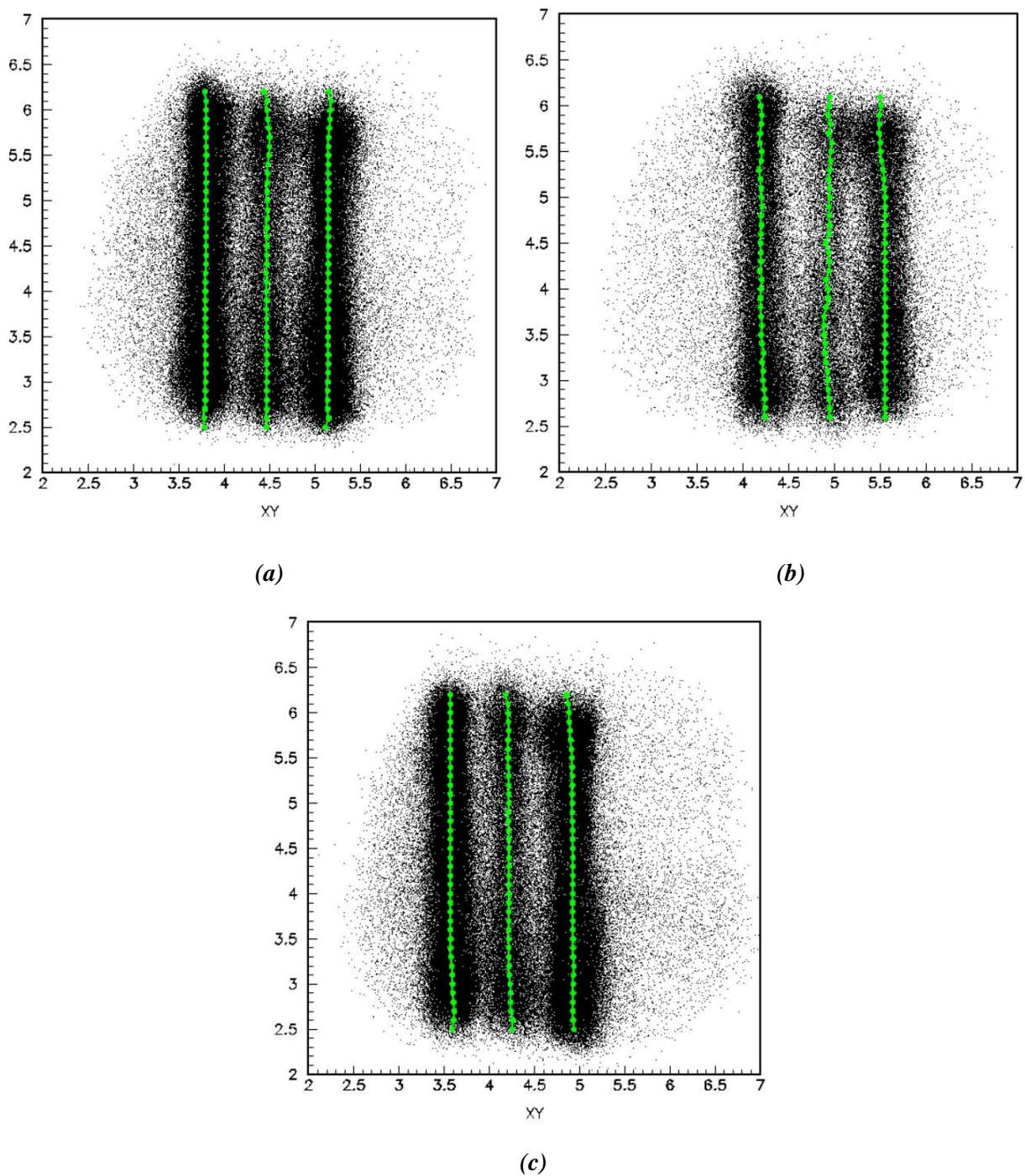
Figure 3.20. *The corrected planar image for the 1st orientation of the phantom (a) and the corresponding ones when the phantom is shifted right (b) and left (c) of the 1st.*

Chapter IV

γ-Camera Test at Tomographic Level

   To complete a study about a small field γ-Camera system at preclinical level, it is necessary to check and test it at tomographic level. For this reason, the use of more complicated geometrical phantoms or even small animals, like mice, is imperative. What we study in this chapter, are the methods with which we finally take the reconstructed image and of course the information needed. However, the reconstruction of an object in computed tomography (CT) is a multicomplex   problem.
   The two methods that can be chosen to reconstruct a SPECT image are the Analytical and on the other hand the Statistical one. Both algorithms have been implemented in clinical modalities in order to reconstruct images of lesion and organs within the human body. Tomographic image reconstruction is based on measured estimation of the integral of radiotracer distribution as seen under different angles (projections). To this direction, both Analytical and Statistical algorithms have been developed **[SEM08]**.

   Image reconstruction in computed tomography (CT) is the task of computing the spatial structure of an object that is based on calculated estimation of the integral of radiotracer distribution as seen under different angles (projections). The solution for this problem is really complex and involves techniques not only in physics but in mathematics and computer science too.
   If one considers a single slice through the examined object or the patient the relevant parameter in them can be expressed mathematically as a function $f(x,y)$ in which the spatially-dependent values of f correspond to the distribution of radiopharmaceutical in SPECT. The *Tomographic Problem*, which is an inverse problem, lies in the reproduction of the real image from its observed, experimental data that differs from recording to recording.

4.1 Analytical Reconstruction Algorithms

   Analytical reconstruction algorithms model the measurement of radiotracer distribution in a simplified way, so that an exact solution may be calculated analytically. This kind of algorithms ignore a number of physical effects during acquisition, such as limited sampling, Poisson statistics in photon counting, attenuation or radiotracer decay, resulting in reduced image accuracy. There are many types of analytical reconstruction techniques, but Filtered Back Projection (FBP) has been the most widely used analytical algorithm. A selected one-dimensional filter is applied on projection data before backprojectioning (2D or 3D) the data onto the image space **[LYU16]**. By filtering, it is possible to introduce negative contributions, canceling out the positive counts in areas of zero activity and finally correct image's misleading artifacts. The choice of filter and cut-off frequency determines resolution and noise level in the reconstructed image.

4.2 Statistical Reconstruction Algorithms

Different from analytical reconstruction methods, statistical methods use iterative strategies to solve linear systems and reconstruct images by iteratively optimizing an objective function, which typically consists of a data fidelity term and an edge-preserving regularization term. With the advances in computing technology, iterative reconstruction (IR) has become a very popular choice in routine tomography practice because it has many advantages compared with conventional FBP techniques. Important physical factors including focal spot and detector geometry, photon statistics, X-ray beam spectrum, and scattering can be more accurately incorporated into iterative reconstruction, yielding lower image noise and higher spatial resolution compared with FBP. In addition, IR can reduce image artifacts such as beam hardening, windmill, and metal **[TOM18]**.

4.2.1 Sinogram

In order to reconstruct a two-dimensional image, a series of one-dimensional planar images and their projections p_1, p_2, … , p_n are acquired with the detector orientated at different angles with respect to the object (*Figure 4.1*). In SPECT the image represents the biodistribution of the injected radioactive agent.
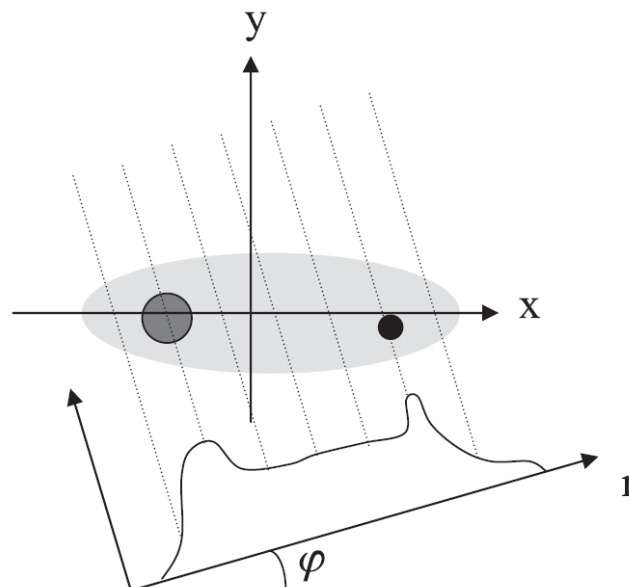
Figure 4.1. *The object being imaged is represented as f(x,y) where x and y are the image coordinates. Here, high distributions of injected radioactive tracer are represented by darker colors. The projection plots the intensity as a function of r, where the highest values correspond to lines passing through the darker disk-shaped areas (Figure taken from* N. B. Smith & A. Webb: '*Introduction to Medical Physics, Physics, Engineering and Clinical Applications',* New York, 2011).

A common method of displaying projection data is a *sinogram*, in which the projections are plotted as a function of the angle φ. A sinogram is a grey scale plot where the density of image is a monotone function of the measured projection values $p(r,\varphi)$ where φ taking values between 0° and 360° **[EPS08]**.
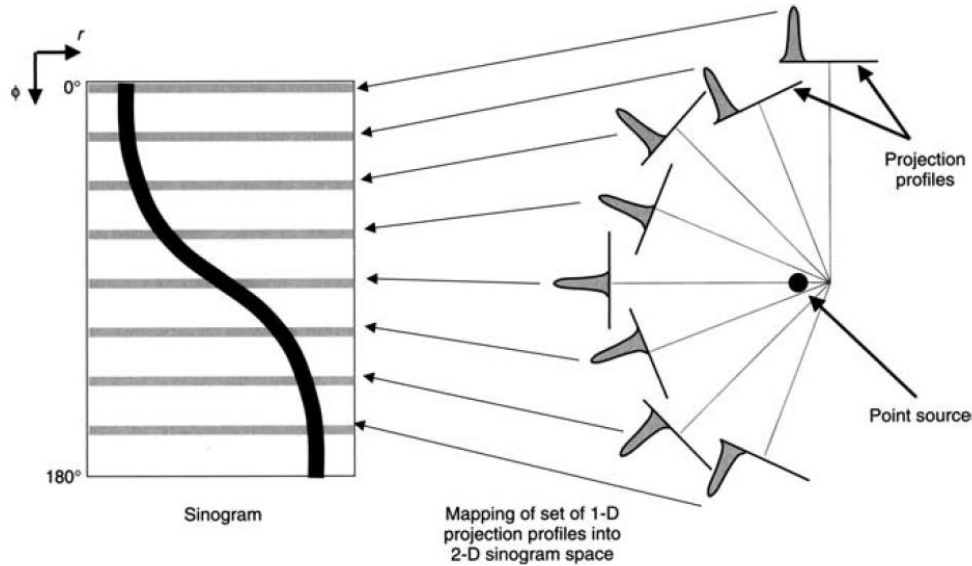
Figure 4.2. *Two-dimensional (2D) intensity display of a set of projection profiles. Each row in the display corresponds to an individual projection profile, sequentially displayed from top to bottom. A point source of radioactivity traces out a sinusoidal path in the sinogram.* (*Figure taken from* Simon R. Cherry et al.: '*Physics in Nuclear Medicine*', Fourth Edition, W B Saunders Co Ltd 2012, **[CHE12]**)
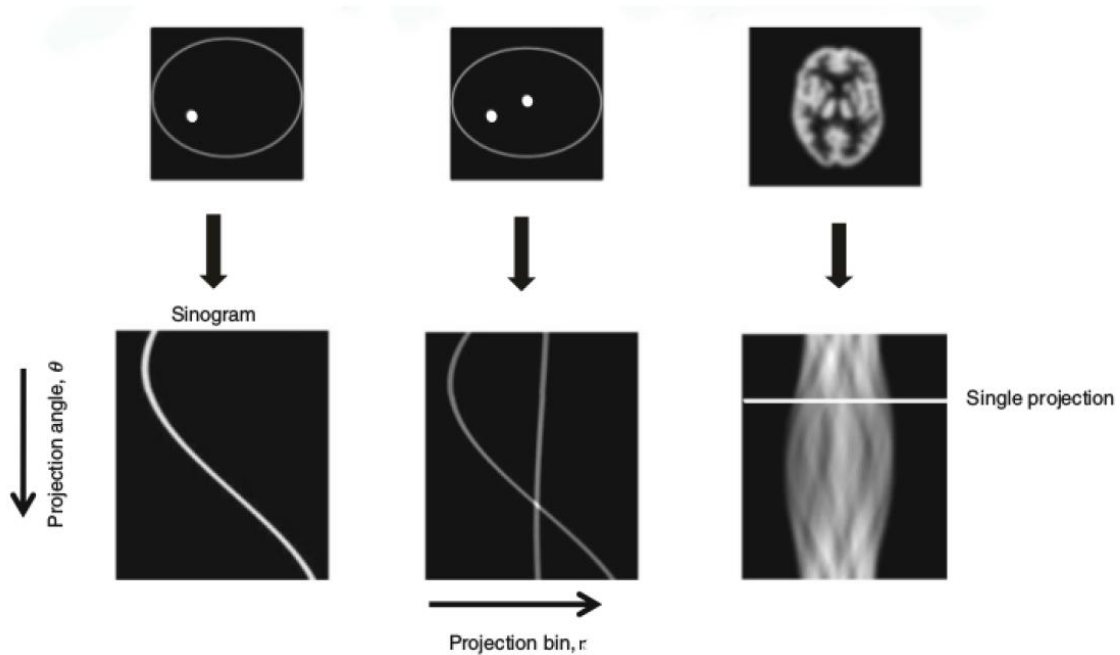
Figure 4.3. *Examples of sinograms for multiple of hot spots and more complex structures.* (M. E. Tomazinaki,:'*Artificial Neural Networks in Single Photon Emission Tomography (SPECT)*', Master Thesis, University of Athens, 2018).

4.2.2 Projection Matrix

When using algebraic methods, one proceeds with the physically correct assumption that the X-ray beam, in CT for example, has a certain width. When passing through tissue, one now has to take into account how much of the pixel that is to be reconstructed is passed through by the beam. For this purpose, weights are introduced that reflect the relation between the area that is illuminated by the beam and the entire area of the pixel.
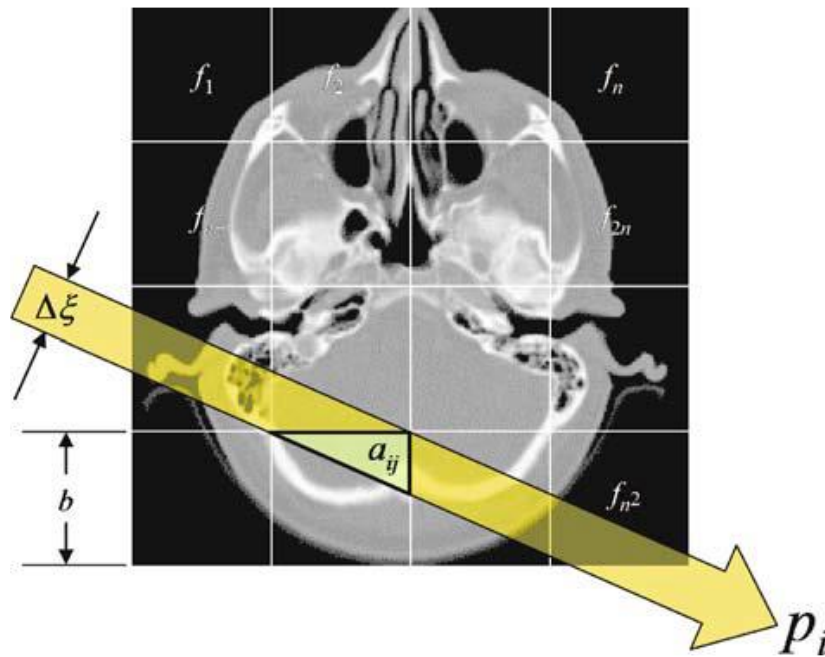
Figure 4.4. *The X-ray beam of width Δξ does not traverse all pixels of size b² equally when passing through the tissue. The area of the pixel section that has actually been passed through and that is to be reconstructed must be included in the system of equations as a weighting (Figure from* Thorsten M. Buzug: *'Computed Tomography, From Photon Statistics to Modern Cone-Beam CT'*, Springer, 2008*).*

A beam of width, Δξ, passes through the tissue – again illustrated by cranial tomography. The pixel size is given by b^2. The weight ai j is thus determined by the relation:

$$a_{ij} = \frac{illuminated\ area\ of\ pixel\ j\ ray\ i}{total\ area\ of\ pixel\ j} \qquad (4.1)$$

and lies in the interval $0 < a_{ij} < 1$.

So, from *Figure 4.4,* we have the following system of equations that finally describes the problem

$$\sum_{j=1}^{N} a_{ij} f_j = p_i \qquad (4.2)$$

in which the weights, a_{ij}, are taken into account. N is the number of the pixels, n^2, that are to be reconstructed, and $i = \{1,\ldots,M\}$ is the index of the projection, with $M = N_pD$ being the total number of projections (p_i) of all detector elements, D, of the detector array in all projection directions, N_p. In an expanded form *(4.2)* is given as

$$a_{11}f_1 + a_{12}f_2 + \cdots + a_{1N}f_N = p_1$$
$$a_{21}f_1 + a_{22}f_2 + \cdots + a_{2N}f_N = p_2$$
$$\vdots$$
$$a_{M1}f_1 + a_{M2}f_2 + \cdots + a_{MN}f_N = p_M \qquad (4.3)$$

Within nuclear diagnostic imaging, as in PET and SPECT, in which the representation of the photon paths as a set of linear equations is used in a statistical approach, the weightings are to be interpreted as probabilities that gamma quanta from the area element j are detected in projection i. Linear physical processes can be built into the imaging model via appropriate weightings of the projection equations. In this way, the imaging quality can be improved because the mathematical model that the reconstruction is based on can be tailored to match the real physical situation **[BUZ08]**.

Writing all projections as column vector

$$\boldsymbol{p} = (p_1, p_2, \ldots, p_M)^T \qquad (4.4)$$

and writing the attenuation values that are to be reconstructed as a column vector as well (that previously in *Figure 4* were presented as an image matrix)

$$\boldsymbol{f} = (f_1, f_2, \ldots, f_N)^T \qquad (4.5)$$

the weightings are thus presented as an $M{\times}N$ matrix

$$A = \begin{pmatrix} a_{11} & a_{12} & \ldots & a_{1N} \\ a_{21} & & \ldots & a_{2N} \\ & & & \vdots \\ a_{M1} & & .. & a_{MN} \end{pmatrix} \qquad (4.6)$$

such that the system of equations becomes

$$\boldsymbol{p} = \boldsymbol{Af} \qquad (4.7)$$

Where p stands for the ensemble of all the available projections that consists the *sinogram*, A_{ij} known as *Projection Matrix* which is finally a weighting matrix, which carries the information of how much each element of the matrix being reconstructed contributes to each ray and f the vector that contains all the grey value of the image grid. Now, in order to solve the matrix problem in equation *(4.7)*, all we have to do is to inverse the A matrix as follows

$$\boldsymbol{p} = \boldsymbol{Af} \Leftrightarrow \boldsymbol{A^{-1}p} = \boldsymbol{A^{-1}Af} \Leftrightarrow \boldsymbol{A^{-1}p} = \boldsymbol{If} \Leftrightarrow \boldsymbol{f} = \boldsymbol{A^{-1}p} \qquad (4.8)$$

Figure 4.5. *Sinogram, Projection and Image Matrix as the equation (4.7) dictates, where N×N is an Image square matrix, N_p the number of projections and N_R the number of the constant width ray per each projection .*

4.2.3 Algebraic Reconstruction Technique

Algebraic Reconstruction Technique, knowns as ART for simplicity, use iterative strategies and a linear model for the measurement process and the solution (over- or undetermined) of linear systems so that the reconstruction problem can be posed as a system of linear equations. ART seems to be an extension to Kaczmarz method in 1937 for solving this kind of problems.

This technique has been introduced in biomedical imaging by Gordon et al.(1970) and in today's clinical routine algebraic methods for image reconstruction are widely disregarded due to the substantial amount of inherent computational effort. Even if FBP is the working horse of image reconstruction due to the computational expense of ART, this method is more instructive since it represents the reconstruction problem as a linear system of equations **[BUZ08]**.

Moreover, the greatest advantage of ART in the computed tomography is the ability to produce better images than other methods from fewer projections **[ANG09]**.

First of all, this technique usually starts with the notion that the realization of an image, $f = (f_1, \ldots, f_N)^T$, presents a point in an N-dimensional solution space. Starting with an initial image, $f^{(0)}$, a sequence of images, $\{f^{(1)}, f^{(2)}, \ldots \}$, is calculated iteratively that converges to the desired tomographic reconstruction.

In the first step, a forward projection,

$$\mathbf{p^{(n)} = Af^{(n)}} \tag{4.9}$$

of the nth image approximation $f^{(n)}$ is determined. The projection, $p^{(n)}$, determined in the nth forward projection can then be compared with the actual measured projection, p. The comparison between the determined and the measured projection yields correction terms that are applied to

the nth image approximation, $f^{(n)}$, resulting in the $(n + 1)^{th}$ image approximation. This process is iteratively repeated such that with another forward projection, the projection $p^{(n+1)}$ is determined.

 An illustrative example first published by Kak and Slaney (1988) and Rosenfeld and Kak (1982) in order to impress the idea of the correction using this strategy. For simplicity, the desired image consists of two pixels f_1 and f_2 and two measured projections p_1 and p_2 are available. So the corresponding equations system is:

$$a_{11}f_1 + a_{12}f_2 = p_1$$
$$a_{21}f_1 + a_{22}f_2 = p_2 \qquad\qquad (4.10)$$

 As a starting point, one needs an initial image, $f^{(0)}$ (*Figure 4.6),* as a base for which the iteration shall be started. This image could result from a rudimentary backprojection (BP),for example. However, an image that is equivalent to the zero vector, $f^{(0)} = (0,0, \ldots ,0)^T$, serves the purpose equally. This vector is projected perpendicularly onto the first straight line that represents the first X-ray beam with the projection result, p_1 , in order to obtain a new and improved image, $f^{(1)}$. This image is then projected perpendicularly onto the second straight line. Therewith, one obtains an image that is improved with respect to $f^{(1)}$ because $f^{(2)}$ lies closer to the intersection point of the straight lines than its two predecessors. Note, if both straight lines *(4.10)* are perpendicular to each other, one will reach the intersection point within two iterations. In practice, this method almost always converges. The only exception is the case of parallel straight lines intersecting in infinity.
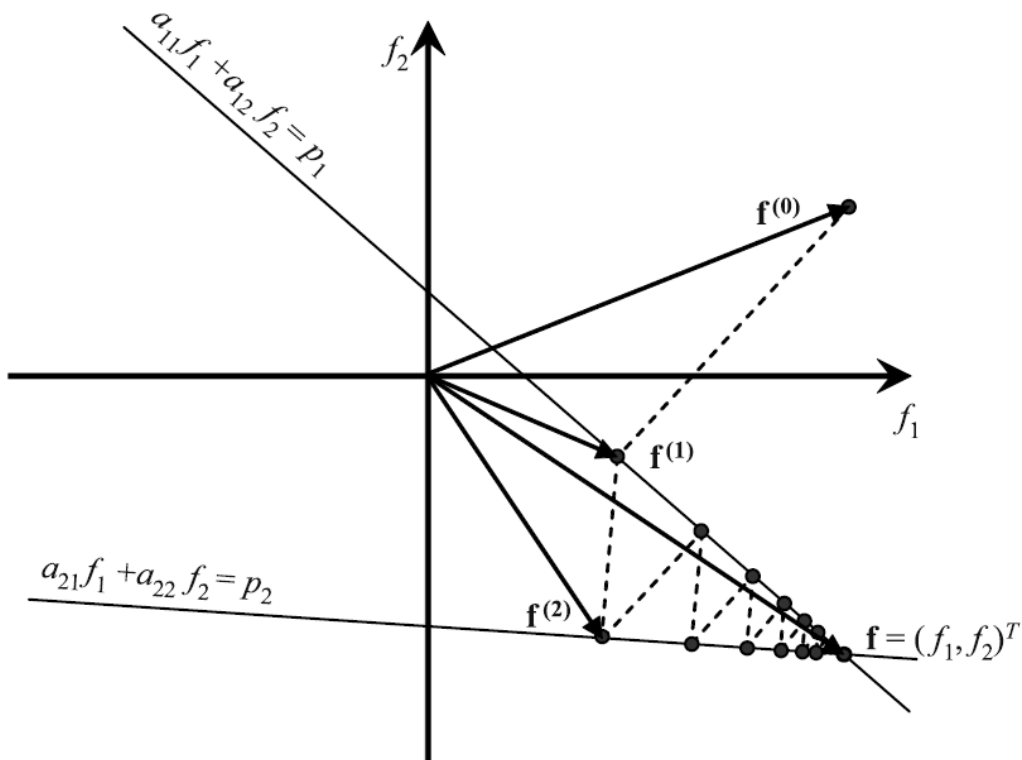
Figure 4.6. *Iterative solution of the system of equations (4.10) (adapted from Kak and Slaney [1988] and Rosenfeld and Kak [1982]). In the two-dimensional solution space each equation of the system (4.10) is represented by a straight line. The intersection point of the two lines gives the solution vector $f = (f_1 , f_2)^T$, i.e., the desired pixels of the image (Figure from* Thorsten M. Buzug: *'Computed Tomography, From Photon Statistics to Modern Cone-Beam CT'*, Springer, 2008*).*

However, physically this would mean that one has measured the same direction twice and therefore either no new spatial information can be gained (mathematically this means that the system of equations is singular because it is linearly dependent) or a different projection result is obtained. This result is caused by measurement noise, which is inconsistent.

A projection value, what is just a Radon transform is

$$p_i = \sum_{j=1}^{N} a_{ij} f_j \tag{4.11}$$

and finally the iteration equation is given by Kak and Slaney 1988:

$$f^{(n)} = f^{(n-1)} - \frac{(a_i f^{(n-1)} - p_i)}{a_i (a_i)^T} (a_i)^T \tag{4.12}$$

where α_i is a certain row I of the system matrix, which means $a_i = (a_{i1}, a_{i1, \dots}, a_{iN})$.
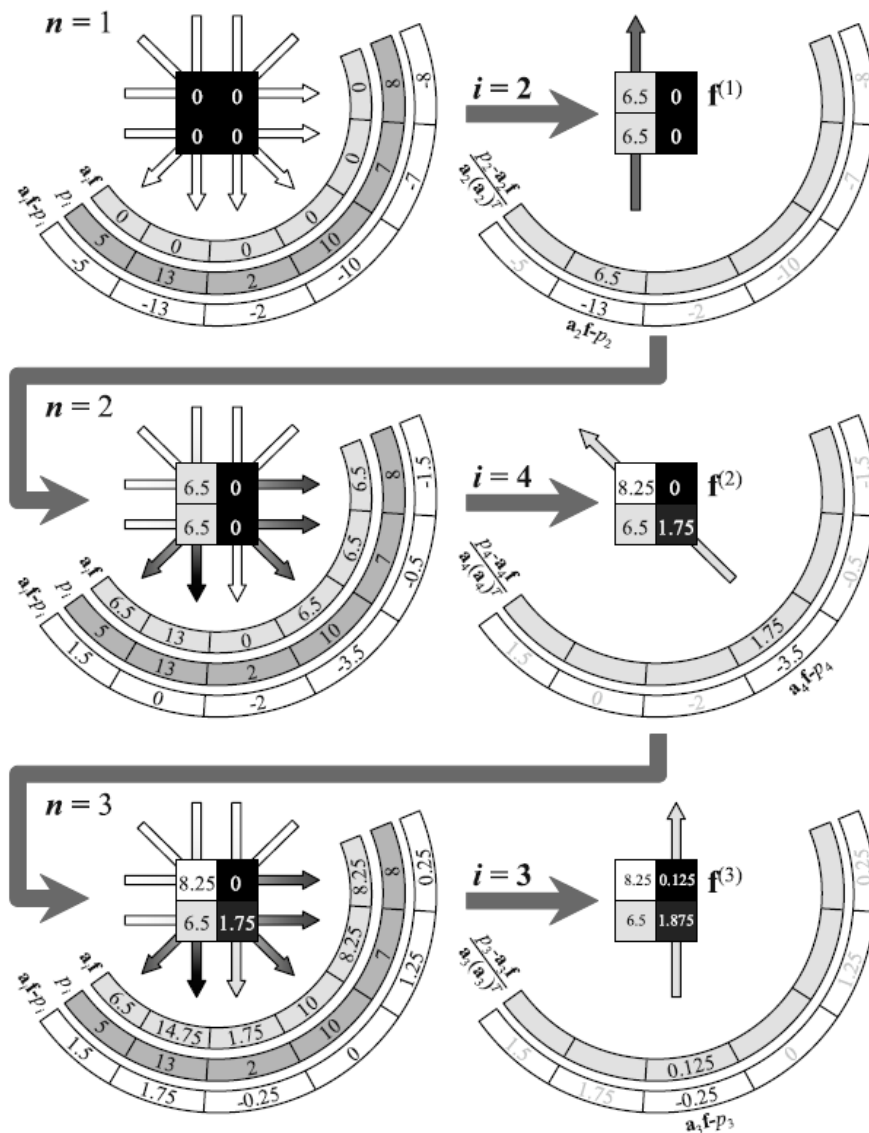

Figure 4.7. A schematic illustration of the first three iterations of ART technique, for a 2×2 Image Matrix. Using $f^{(0)} = (0,0,0,0)^T$ as an initial image and that the correct image values are $f = (8, 0, 5, 2)^T$.

4.3 Experimental Data

4.3.1 A Complex Geometrical Phantom

In this paragraph of the chapter, we pass from planar to tomographic images based on data from a complex geometrical phantom. More specifically, as *Figure 4.8* shows, the phantom consists of a cylindrical pyrex into which we have adapted two capillaries of the same volume and size (1), two small tubes of the same volume (2) and a central bigger tube (3), all of them filled with Tc^{99m}.
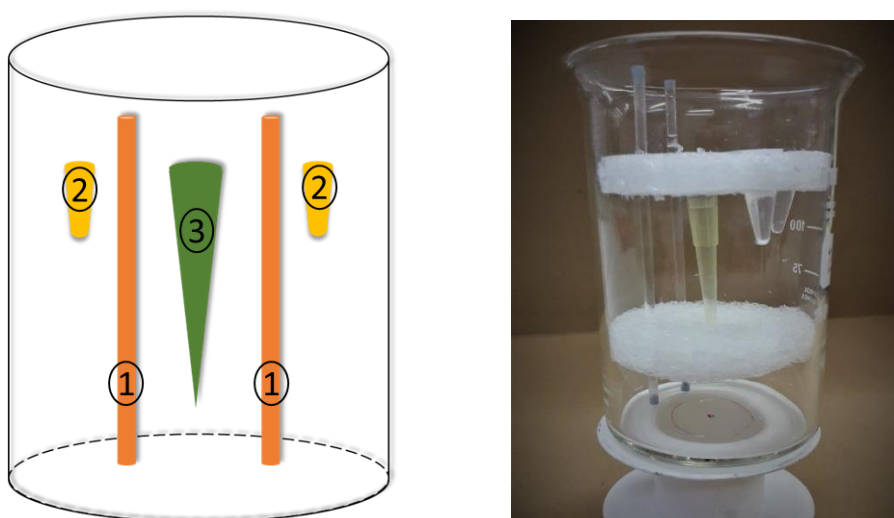
Figure 4.8.a. A schematic depiction of the geometrical phantom (left) and a photograph of it (right).
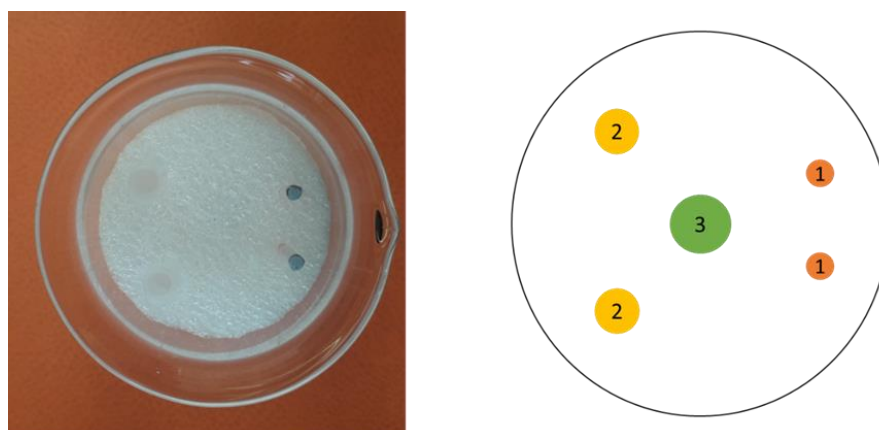
Figure 4.8.b. A photograph from the top of the phantom where the 3rd tube cannot be seen since it is under the supporting foam(left) and a schematic illustration of its top view.

The volumes and information about the activity of radioactive tracer Tc^{99m} that each element of the phantom is filled with, are included in the following table:

N	Specific Activity	Volume	Absolute Activity
1	0.73μCi/μL	200μL	146.0μCi
2	0.73μCi/μL	250μL	182.5μCi

3	0.73μCi/μL	300μL	219.0μCi
TOTAL	0.73μCi/μL	750μL	547.5μCi

Table 4.1. *Calculated volumes and 99mTc activity for the five elements used in the phantom.*

The protocol that was followed for the experimental process included 24 planar images of the phantom with a fixed step of 15º covering the full angle region (0º-360º) and 100000 events per run.

(α)

(b)

(c)

(d)
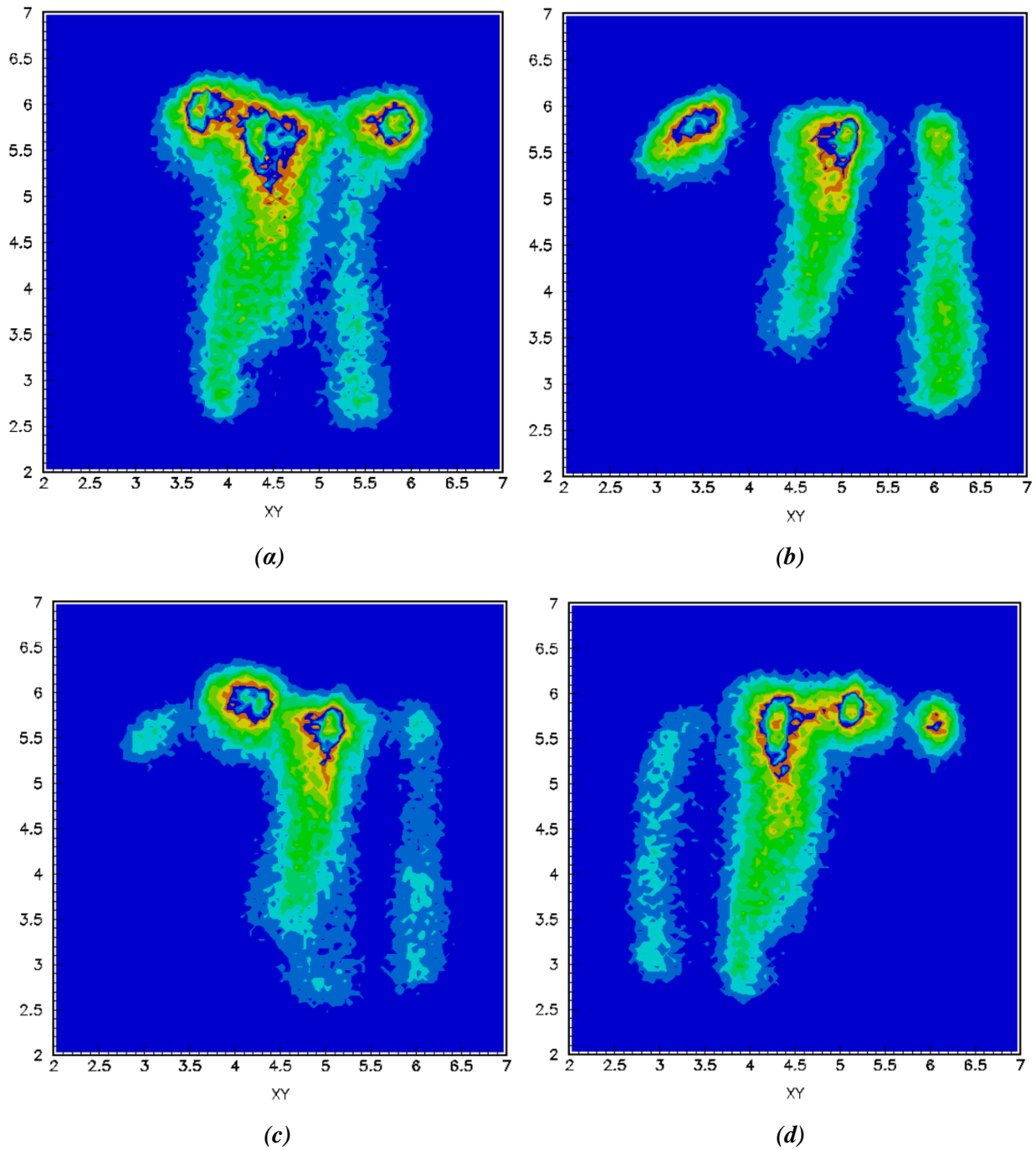
Figure 4.9. *Some recorded planar images of our phantom at 0º(a), 90º(b), 135º(c) and 315º(d) after the correction technique as described in paragraph 3.2. In some of them we can clearly see all the five elements of the phantom (a,c) whereas in b we have the overlapping of the two capillaries (element 1) between them and the two tubes (element 2) respectively.*

The planar information is further analyzed to reconstruct the tomographic images, taking into account all off-line corrections needed to remove barreloid deformations appearing at the edges of the FOV, as they have been described in the previous chapter in paragraph 3.2 (*Figure 4.9*).

Figure 4.10. *The 3D reconstructed image of the phantom from an angle that all the five elements of which is consisted are distinguished. Up the uncorrected image and down the corrected one.*

Afterwards, every projection was sliced 21 times along the Z-axis, bottom to the top of the phantom. 64 × 64-pixel reconstruction images are created by using iterative technique and more specifically ART algorithm, for all information recorded in the ensemble of the planar images and for the whole angular range. From this procedure, we extracted 21 tomographic images along Z-axis that were synthesized with the technique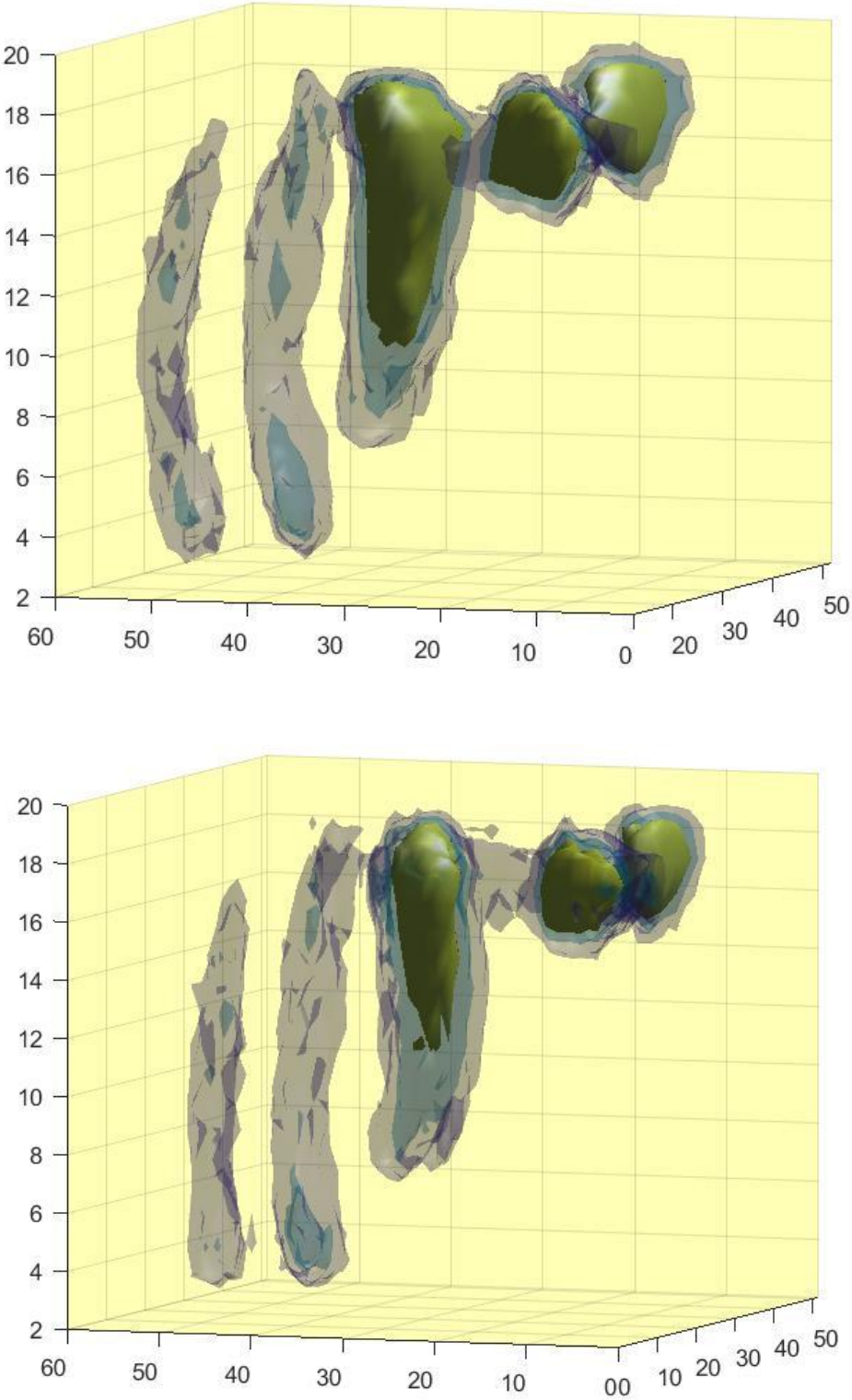 of stacking, using the MATLAB software (*Figure 4.10*). In the reconstructed image we can clearly see all the five elements of the phantom, even the capillaries. So, the sensitivity of our SPECT-LAB γ-Camera system derived from this experiment is:

~ 0.73μCi/μL for volumes of *200μL* such as the capillaries.

Finally, the 2D correction technique seems to affect the tomographic image, a fact that it is more clear at the depiction of the capillaries, since they seem to be straightened. Moreover all the elements of the phantom have been moved and as a result each one's limits are more clearly depicted.

4.3.2 Small Animal Imaging

4.3.2.1 Introduction to Small Animals Imaging

The use of small animal models in basic and preclinical sciences constitutes an integral part of testing new pharmaceutical agents prior to commercial translation to clinical practice and a fertile ground for many studies about the optimization of the imaging techniques. Whole-body small animal imaging is a particularly elegant and cost-effective experimental platform for the timely validation and commercialization of novel agents from the bench to the bedside **[KAG10]**.

Mice in particular are favorite animal subjects: they are economical, reproduce rapidly, and can provide models of human disease. Mice with compromised immune systems have been used for many years in studies of human tumor xenografts. The sequence of the mouse genome has been determined, and knockout mice (in which expression of a particular gene has been disabled) are available as models of various metabolic abnormalities **[KUP05]**.

4.3.2.2 Mouse Imaging Using the SPECT-LAB γ-Camera

The final step of this study was to evaluate the feasibility of a small animal imaging at tomographic level using our SPECT-LAB γ-Camera. The observed animal was a mouse labelled with Tc^{99m} with respect to the appropriate moral protocol of this procedure. The study was carried out by using the set of planar projections obtained for the SPECT scan of the mouse to reconstruct 2D tomographic images of the inner radioactive distribution.

In this study the area of interest was the mouse's lungs. For this purpose the appropriate radiopharmaceutical should be prepared. This process included PULMOCIS (CURIUM®), which is a standard package for the preparation of an injectable solution of Technetium [^{99m}Tc] human albumin macroaccumulates, which is used for scintigraphic imaging of the lungs perfusion. More specifically, using a syringe, we added 2.5 mL sterile free pyrogen sodium pertechnetate [^{99m}Tc] solution, 5.5 mCi radioactivity. The vial was shaken for about 2 minutes while administration of the radiopharmaceutical was done 15 minutes later. In a Swiss standard muscle, 200 μL [^{99m}Tc] Tc-Pulmocis (~ 500 μCi) was administered, and the radiopharmaceutical was allowed to circulate for 30 min. It was followed by killing of the muscle, and imaging it in our experimental gamma camera.

For this experiment we took 24 planar images, with a fixed step of 15° for all the range of 0° to 360° and 100000 recorded events each. The mouse was placed on a rotating table in the front of the camera. In order to achieve the higher spatial resolution, the distance between the animal and the front of the collimator was less than 1 cm (*Figure 4.11*).
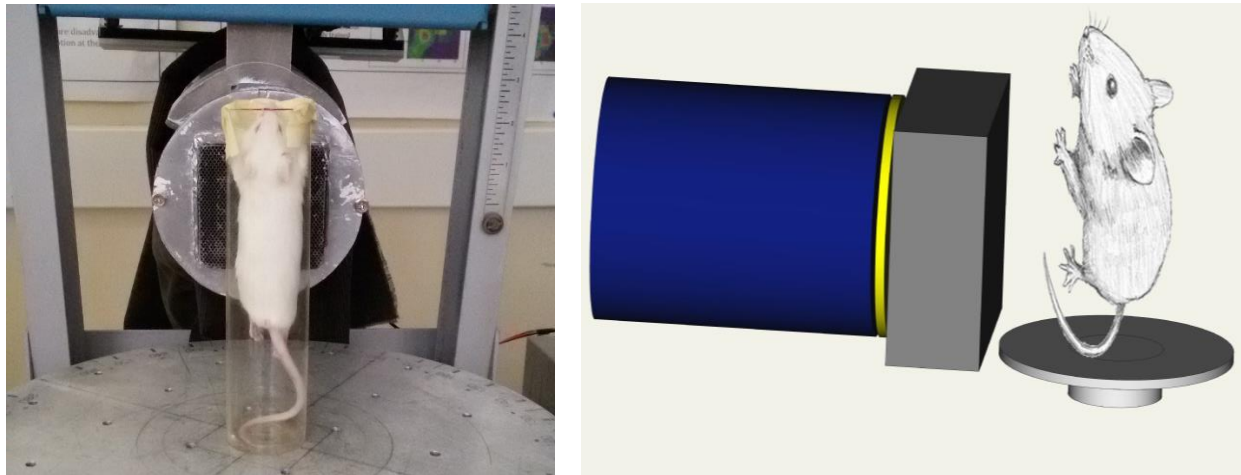

Figure 4.11. *The labelled mouse in front of the γ-Camera System (left) and a schematic illustration of the imaging procedure (right).*

The first recorded image and the orientation of the mouse at 0° was with the mouse lungs in front of the γ-Camera System (*Figure 4.11*). The supply PSPMT's high voltage was at 1310V and the recorded events 50000 per run. Each planar image was further corrected with the 2D correction technique defined at section 3.2.

Some of the recorder planar images are shown in the following figures (*Figure 4.12, 4.13*), where we can clearly identify the two lungs of the mouse which are more intensely depicted. When the contouring of the image is in linear scale we can barely notice the existence of another hot spot except of the lungs. This suspicion increases when the contouring scale becomes logarithmic, where these hot spots are now obvious and could be attributed to the mouse kidneys.
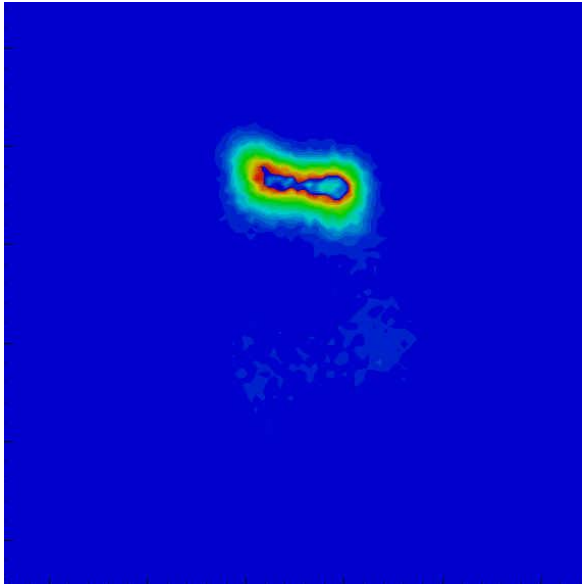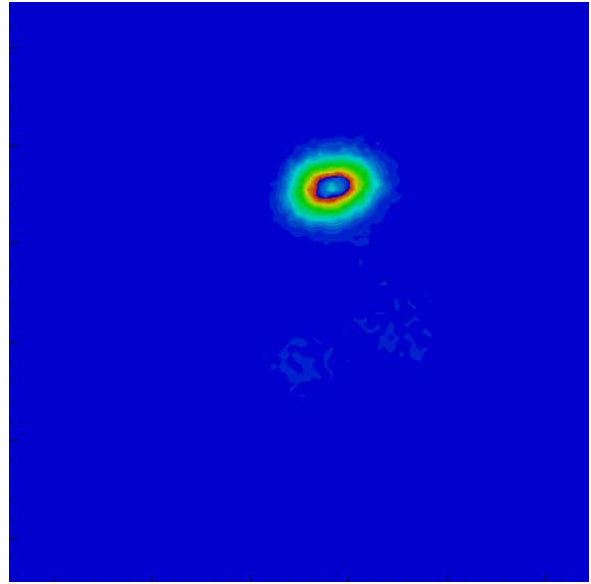
(a) *(b)*
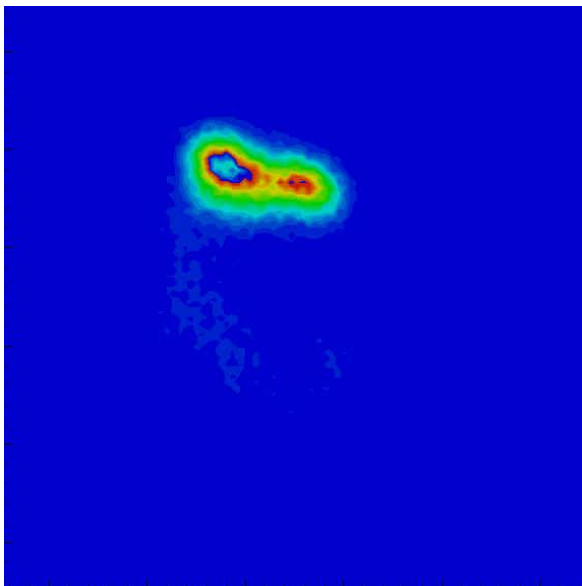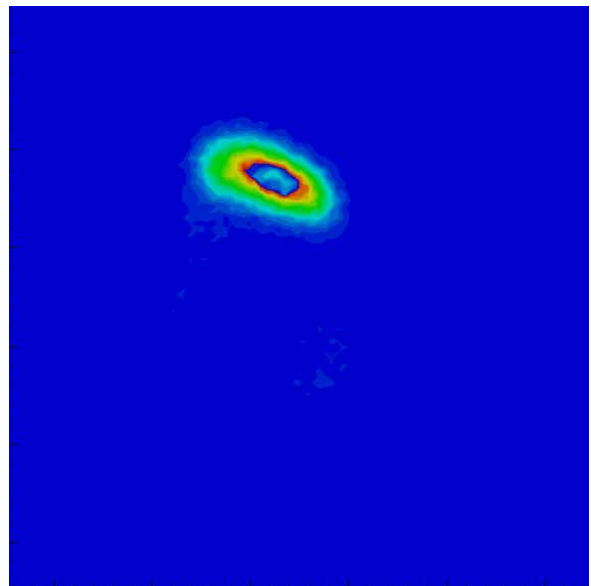
(c) *(d)*

Figure 4.12. *Some planar images of the labelled mouse at 0º (a), 90º (b), 210º (c) and 300º (d) with a linear scale contouring. In all these images the lungs are identified.*
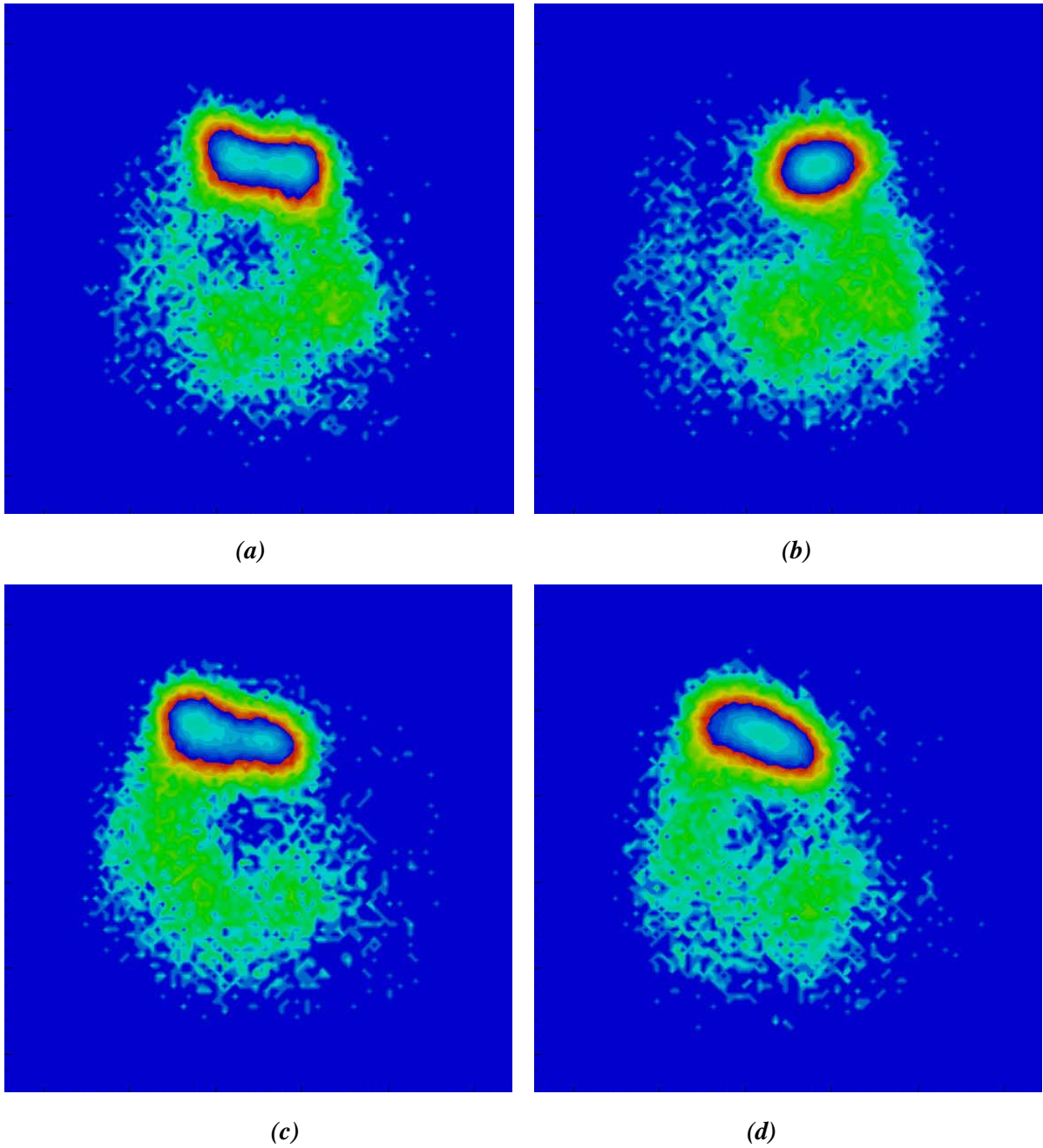
Figure 4.13. *Some planar images of the labelled mouse at 0ᵒ (a), 90ᵒ (b), 210ᵒ (c) and 300ᵒ (d) with a logarithmic scale contouring. In all these images the lungs are depicted more intense and two more hot spots are noticed that probably are the kidneys .*

It is also interesting to see the tomographic images along the z axis of mouse. By height and from the bottom to the top we can firstly identify the kidneys of the mouse and then the area of

interest, the lungs. It is obvious (*Figure 4.14*) that the lungs are the organ with the biggest radiopharmaceutical uptaking.
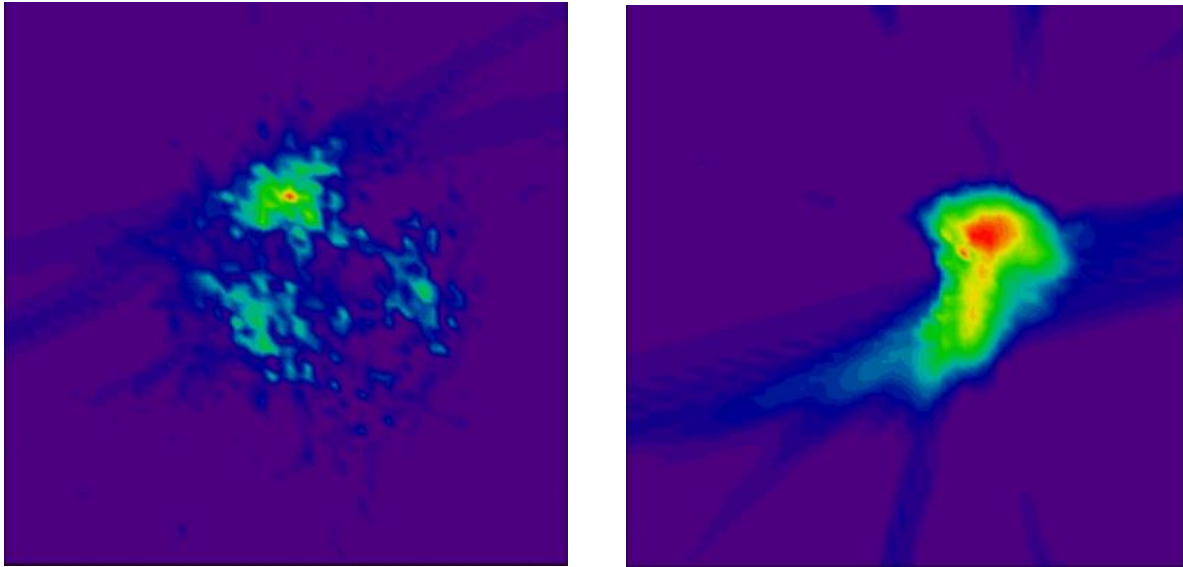
Figure 4.14. Two tomographic images that depict the mouse kidneys (left) and lungs (right).

Finally, all the planar information is further analyzed to reconstruct the tomographic images with the use of ART. In order to extract the 3D reconstructed image of the mouse's areas of interest the tomographic images were stacked and the final result is shown in *Figure 4.15*.
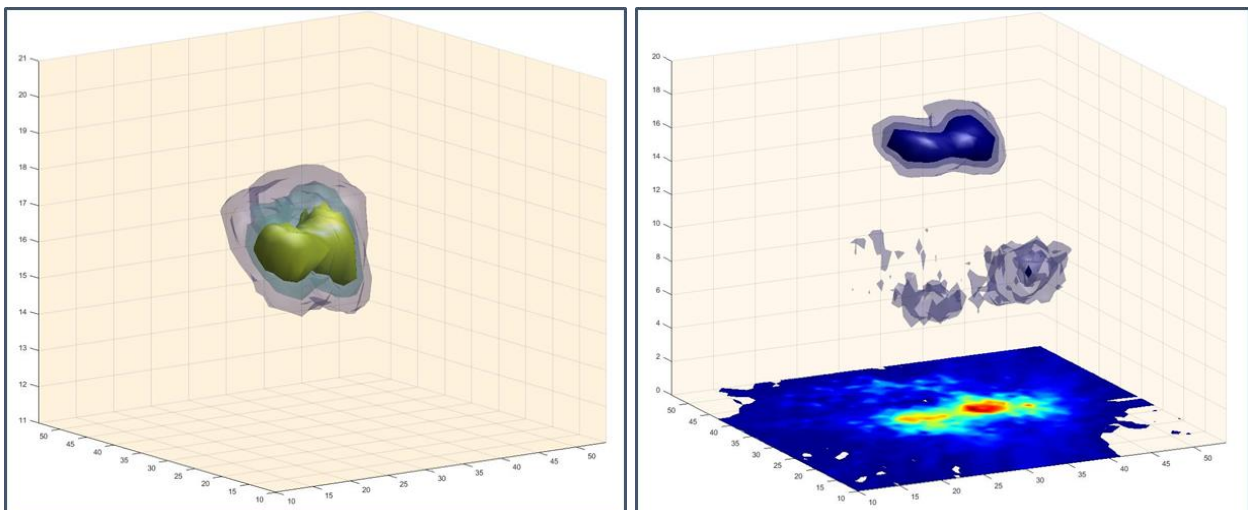
Figure 4.15. A 3D reconstructed image of the mouse lungs with linear scale contouring (left) and with algorithmic contouring scale (right).

Chapter V

Conclusions

In the present thesis, a complete study of a small-field, high resolution γ-Camera System is represented. This system is basically used at preclinical level for geometrical phantoms and small animals imaging. The main components of the camera is the scintillation crystal, that in our study is a CsI(Tl) pixelated crystal with 1mm pixel size, the Position Sensitive Photomultiplier Tube (PSPMT) which constitutes the body of the camera and the electronics system that final gives the signal. Our SPECT-LAB γ-Camera System is optimized for studies with ^{99m}Tc.

Our first attempt was to characterize the HAMAMATSU R2486 PSPMT of our system in terms of its inner spatial resolution and energy response. For this purpose, we used a plexiglass support with the same diameter of the PSPMT, which is consisted of 21 equidistant holes at 10mm distance. This support is used to guide externally produced light pulses to the PSPMT. The first experimental set included measurements of the light pulse in different hole on the plexiglass per recording with constant PSPMT high voltage and light pulse width. From this process we had the mean value of each X and Y position of the optical fiber in wire coordinates (a.u.) that was taken from the corresponding projections by fitting the suitable gaussians. Since the fiber position is well-known in physical dimensions, we found the mean width of each light pulse profile in both X and Y axes and also their mean values and their deviations for all the 21 possible positions in mm. So, the spatial resolution of the PSPMT is:

$$<FWHM>_x=0.124\pm0.009mm \quad \& \quad <FWHM>_y=0.123\pm0.051mm$$

when the high voltage is 900V and the pulse time width 1μs. However these values worsened when the high voltage decreases to 850V and the pulse time duration to 500ns:

$$<FWHM>_x=0.178\pm0.009mm \quad \& \quad <FWHM>_y=0.181\pm0.078mm.$$

As far as the energy resolution ΔE/E of the PSPMT is concerned, it is inversely proportional to $^1/_{\sqrt{E}}$ and it is represented by the ratio ΔQ/Q. This ratio depends on the position of the event and varies from ~3.00% to 1.90% for high voltage of 900V and pulse time width 1μs. The best energy response is observed when the fiber is on the central hole C_3. For high voltage of 850V and light pulse width 500ns the PSPMT energy response seems to be reduced following the ratio ΔQ/Q which takes values from ~4.00% to 3.11%.

In addition to these measurements, two more sets were taken in order to examine the variation of the PSPMT energy response according to the variation of the light pulse duration and the supply high voltage.

The first step was to verify the linearity between the increasing of the light pulse duration and the total accumulated charge. This had as a result the equidistant peaks of the energy for the recordings between 300 to 1300ns with a fixed step of 100ns. In this set, the ΔQ/Q ratio and consequently the energy response seems to be proportional to $^1/_{\sqrt{T}}$, where T is the light pulse duration. In fact, the light pulse duration T simulates the energy E of the incident γ photons on the scintillation crystal which is proportional to the amount of the produced optical photons.

More specifically, in this study, our PSPMT's energy resolution found to follow the below given relationship:

$$\frac{\Delta Q}{Q} = \frac{A}{\sqrt{T} + B}$$

where A and B are constants that depend on the voltage of the optical fiber.

The second step was to examine the dependence of the PSPMT energy response on the high voltage supply. In general, what was firstly observed was that the energy peaks for high voltage range from 800 to 1100V with a fixed step of 50V, are not equidistant. The total charge accumulated in the anode follows an exponential function of the high voltage supply. Although the PSPMT's high voltage increases, the energy resolution of the photomultiplier seems to be barely better. We have a 2% optimization for 300V increase (from 800V to 1100V) in the dynamic range of the photomultiplier.

The characterization of our PSPMT is completed with the Gain factor in the charge accumulated as a function of the high voltage supply. For the range 800 to 1300V the total charge gain is an exponential function of the high voltage and since the multiplication factor δ in the produced amount of electrons from dynode to dynode depends on the overall gain, we extracted their relationship. Finally, the multiplication factor δ is a linear function of the inter-dynode voltage. In fact δ for conventional dynodes varies as some fractional power of the inter-dynode voltage so that the overall gain is more typically proportional to V^{Neff}. N_{eff} is a number which represents the effective stages of the system and it is normally $N_{eff} < N$, where N is the number of the real stages of the PSPMT. For our system the effective stages that achieve the overall electron gain was calculated $N_{eff} \sim 7.6$ compared to the real stages number N=12.

The second part of this evaluation study was the characterization of the whole SPECT-LAB γ-Camera System. Since our camera used at preclinical level, the process included two simple geometrical phantoms. The first one consisted of ten similar capillaries some of which were filled with ^{99m}Tc and the others used as spacers. The phantom placed in two different orientations, vertical and horizontal. From their planar images that analyzed in slices, in order to be able to extract the corresponding projection's FWHM, we found the spatial resolution of the whole system which is:

$$<\sigma_X> = (1.52 \pm 0.08) \text{ mm} \ \& \ <\sigma_Y> = (1.62 \pm 0.20) \text{ mm}.$$

The second phantom consisted of nine capillaries with two different diameters. Three of them were filled again with ^{99m}Tc and the rest of them were used as spacers too. From this set we verified the γ-Camera spatial resolution in the vertical orientation:

$$<\sigma_X> = (1.57 \pm 0.07) \text{ mm}.$$

Another factor that we had to deal with was the observed spatial distortions that caused because of the limited field of view of the system. What we call barreloid effect should be eliminated in order to optimize the final recorded image. For this purpose we applied an 1D correction algorithm which applies a relevant shift for each event of the image according to the correction that 18 supporting points needed in order to be at their nominal position. Although this technique seemed to work for the vertical and horizontal orientation, the diagonally oriented phantom did not show any optimization. The reason why this happened is that the spatial distortion depends on both X and Y locations of the event. Therefore, a 2D correction algorithm was developed, that takes in account the 1D shift based on the previous methodology and weights it according to the

information extracted from different supporting lines which were selected at various X locations. In this case, seven nominal lines with 38 supporting points each was used from experimental data derived from the different locations of the capillary phantom.

The final part included tomographic reconstruction of a more complicated geometrical phantom consisted of five elements, capillaries and tubes filled with ^{99m}Tc, 0.73μCi/mL each. After having taken 24 planar images of the phantom with a fixed step of 15° covering the full angular region (0°-360°) corrected with the abovementioned 2D correction technique, we took 21 tomographic slices reconstructed with the Algebraic Reconstruction Technique (ART). All the tomographic images along the z axis were stacked together (using MATLAB) forming a 3D reconstructed image of the phantom. All the five elements were clearly distinguished and the sensitivity of the system was calculated to the value of 0.73μCi/μL for typical capillary volumes of 200μL.

To conclude with, a small animal SPECT imaging completed the present study. In order to estimate the whole system in every possible application at preclinical level, a mouse was labelled with ^{99m}Tc- PULMOCIS (CURIUM®) used for lungs perfusion imaging. The followed protocol was similar to the above: we took 24 planar images covering the full angular region. Then a 3D reconstructed image was created, where the area of interest was clearly formed. With a specific activity of 0.4μCi/μL the lungs measuring 15mm in width were depicted with clarity.

Following this study, our SPECT-LAB γ-Camera system should be explored further and more analytically in terms of its sensitivity and its homogeneity. It could be appropriate to check its signal to noise ratio with or without an absorbent environment for the characterization of the system from each possible point of view. Last but not least the abovementioned 2D correction technique should be checked in every orientation of geometrical phantoms with capillaries in order to have the optimum possible image.

Bibliography

[ANG09] S. Angeli, E. Stiliaris: '*An Accelerated Algebraic Reconstruction Technique based on the Newton-Raphson Scheme*', IEEE Nuclear Science Symposium Conference Record **M09-323** (2009) 3382-3387.

[BUZ08] T.M. Buzug: '*Computed Tomography, From Photon Statistics to Modern Cone-Beam CT*', Springer, 2008, **ISBN:** 978-3-540-39407-5.

[CHE12] S.R. Cherry et al.: '*Physics in Nuclear Medicine*', Fourth Edition, W.B. Saunders, 2012, **ISBN:** 978-1-416-05198-5.

[CUL08] J. Culver, W. Akers, S. Achilefu: '*Multimodality Molecular Imaging with Combined Optical and SPECT/PET Modalities*', The Journal of Nuclear Medicine **49** (2007) 169-172.

[EPS08] C.L. Epstein: '*Introduction to the Mathematics of Medical Imaging*', Second Edition, SIAM, 2008, **ISBN:** 978-0-89871-642-9.

[FLY02] S-O Flyckt, C. Marmonier: '*PHOTOMULTIPLIER TUBES, Principles & Applications*', PHOTONIS, 2002.

[GEO08] Ε. Γεωργίου: '*Ιατρική Φυσική, Διαγνωστικές & Θεραπευτικές Εφαρμογές των Ακτινοβολιών*', Π.Χ. ΠΑΣΧΑΛΙΔΗΣ, 2008, **ISBN:** 978-960-399-906-5.

[HAM10] HAMAMATSU: '*Position Sensitive Photomultiplier Tubes with Crossed Wire Anodes, R2486 Series*', HAMAMATSU PHOTONICS K.K., 2010.

[KAG10] G.C. Kagadis, G. Loudos, K. Katsanos *et al.*: '*In vivo small animal imaging: Current status and future prospects*', Medical Physics **37** (2010) 6421-6442.

[KNO00] G.F. Knoll: '*Radiation Detection and Measurement*', Third Edition, John Wiley & Sons, 2000, **ISBN:** 0-471-07338-5.

[KUP05] M.A. Kupinski, H.H. Barrett, Editors: '*Small-Animal SPECT Imaging*', Springer, 2005, **ISBN:** 978-0-387-25143-1.

[LYU16] L. Yu, S. Leng: '*Image reconstruction techniques*', Image Wisely: Radiation Safety in Adult Medical Imaging, 2016.

[MAD07] M.T. Madsen: '*Recent Advances in SPECT Imaging*', The Journal of Nuclear Medicine **48** (2007) 661-673.

[PET11] T.E. Peterson, L.R. Furenlid: '*SPECT detectors: The Anger Camera and beyond*', Physics in Medicine and Biology **56** (2011) R145–R182.

[PIK09] V.W. Pike: '*PET radiotracers: crossing the blood–brain barrier and surviving metabolism*', Trends in Pharmacological Sciences **30** (2009) 431-440.

[POL06] A. Polychronopoulou , D. Thanasas , N. Giokaris *et al.*: '*Position and Energy Resolution of a γ-Camera based on a Position Sensitive Photomultiplier Tube*' , 16th Hellenic Symposium on Nuclear Physics, (2006) 172-179.

[SEM08] W. Semmler, M. Schwaiger, Editors: '*Molecular Imaging I* ', Springer, 2008, **ISBN:** 978-3-540-72717-0.

[SMI11] N.B. Smith, A. Webb: '*Introduction to Medical Imaging, Physics, Engineering and Clinical Applications*', 1st Edition., Cambridge University Press, 2011, **ISBN:** 978-0-521-19065-7.

[THA08] D. Thanasas, D. Maintas, E. Georgiou *et al.*: '*Correcting Spatial Distortion and non-Uniformity in Planar Images from γ-Camera Systems*', IEEE Nuclear Science Symposium Conference Record **M06-19** (2008) 3711-3714.

[TOM18] M.E. Tomazinaki: '*Artificial Neural Networks in Single Photon Emission Tomography (SPECT)*', MSc Thesis, National and Kapodistrian University of Athens, Master of Science Medical Physics and Radiophysics, 2018.

[VAQ15] J.J. Vaquero, P. Kinahan: '*Positron Emission Tomography: Current Challenges and Opportunities for Technological Advances in Clinical and Preclinical Imaging Systems',* Annual Review of Biomedical Engineering **17** (2015) 385–414.

[ZAN12] P. Zanzonico: '*Principles of Nuclear Medicine Imaging: Planar, SPECT, PET, Multi-modality, and Autoradiography Systems*', Radiation Research **177** (2012) 349-364.